AN IMAGING TECHNIQUE FOR SIZING BUBBLES IN FLOTATION SYSTEMS

Jose Ramon Hernandez Aguilar

Department of Mining, Metals and Materials Engineering

McGill University, Montreal

October 2004

A thesis submitted to McGill University

in partial fulfillment of the requirements of the degree of

Doctor of Philosophy

Your file Votre référence
ISBN: 0-494-12856-9
Our file Notre référence
ISBN: 0-494-12856-9

To the memory of my father,
Prof. Oscar Hugo Hernández Yáñez
"Estamos bien, porque estamos juntos"

and

To my wife, Noriko-san,
with all my love

ABSTRACT

A sampling-followed-by-imaging technique for sizing bubbles in flotation systems has been developed and validated. The technique is based on directing a sample of bubbles into a viewing chamber where they are exposed and digitally imaged using incoherent backlighting. The images are automatically analyzed by means of a threshold criterion. The chamber is sloped to spread the bubbles over the surface of the viewing (glass) window. This configuration reduces bubble overlap and facilitates the definition of the focus plane.

To validate the images, measurements were compared with standardized bubble sizes obtained with the displaced-volume method. It was observed that when thresholding at half the intensity level, sizes were systematically underestimated and the bias was correlated to bubble size, increasing from 0.3% at ca. 0.7 mm to 2% at ca. 4 mm. Experiments were designed to evaluate the bias due to system optics (i.e., the contribution of reflected/refracted rays and the defocus distance to image formation) and due to the sloped window. The results showed that reflected/refracted rays slightly biased towards underestimated sizes whereas the inclined window caused a small overestimation. The overestimation was due to the bubble flattening caused by the gravity force. These two effects were of similar magnitude and, therefore, tended to cancel. Consequently, the underestimation trend was attributed to the defocus distance which, in this unique system, is small and unambiguous (i.e., it is invariably negative since bubbles flow "behind" the focus plane, the underside of the window). A semi-empirical correction procedure is suggested which uses the fundamental method of

Bongiovanni et al. (1997) to correct the bias due to system optics along with an empirical approach to compensate for bubble flattening.

To verify whether the computed size distributions were representative of the actual dispersion, bubble populations with significantly different size classes were mixed in a bubble column (0.1 m x 2.5 m). The column was equipped with two independently aerated spargers with nominal porosities of 0.5 μm (generating bubbles from 0.2 mm to 1 mm) and 100 μm (generating bubbles from 1 mm to 5 mm), respectively. Various proportions of airflow rates were injected through each sparger. The results showed bi-modal distributions in which the real and calculated proportions corresponded with a deviation of less than 15%, considered good given the severity of the test. However, the deviation was correlated to the superficial gas velocity (J_g) and bias was consistently against smaller bubbles. The data were not sufficient to reveal the cause of the bias, but several possibilities were entertained.

The technique was demonstrated in an industrial-scale flotation machine, where it was compared with a capillary technique. It was also used to determine the bubble surface area flux (S_b) in a micro–flotation cell, setting up a test of the proposed relationship between the flotation rate constant k and S_b for the pulp zone.

RÉSUMÉ

Une technique d'échantillonage-suivi-d'imagerie pour le calibrage de bulles des systèmes de flottation a été dévelopée et validée. À la base de cette technique, un échantillon de bulles est dirigé vers un hublot d'observation, où les bulles y sont exposées et imagées digitallement en utilisant un éclairage en contre-jour incohérent. Les images sont analysées automatiquement au moyen d'un critère de seuil. Le hublot est incliné afin de disperser les bulles à la surface de la fenêtre (vitre) d'observation. Cette configuration réduit le chevauchement des bulles et facilite la définition du plan focal.

Pour valider les images, les mesures ont été comparées à des grosseurs de bulles normalisées obtenues à l'aide d'une méthode de volume de refoulement. Il a été observé qu'en fixant le seuil à la moitié du niveau d'intensité, la grosseur était systématiquement sous-estimée. Le biais est en correlation avec la grosseur des bulles, augmentant de 0.3% à ca. 0.7 mm jusqu'à 2% à ca. 4 mm. Les expériences étaient conçues pour évaluer le biais du au système optique (i.e., la contribution des rayons réfléchis/réfractés et la distance de flou à la formation de l'image), ainsi que celui causé par l'inclinaison de la fenêtre. Les résultats démontrent que les rayons réfléchis/réfractés étaient légèrement biaisés vers une sous-estimation de la grosseur alors que l'inclinaison de la fenêtre causait une certaine sur-estimation, due à l'aplatissement des bulles par la gravité. Ces deux effets, de magnitude similaire, ont tendance à se canceller. Par conséquent, la tendance de sous-estimation a été attribuée à la distance de défocalisation (flou) qui, pour cet unique système, est minime et sans ambiguïté (i.e., invariablement négative puisque les bulles circulent "derrière" le plan focal, sous la fenêtre). Une procédure semi-

empirique est suggérée, utilisant la méthode fondamentale de Bongiovanni et al. (1997) afin de corriger le biais du au système optique en compensant pour l'aplatissement des bulles.

Pour vérifier que les distributions de grosseurs calculées étaient représentatives de la dispersion réelle, des populations de bulles de catégories considérablement différentes ont été introduites dans une collone à bulles. La colonne était équipée de deux aérateurs à bulles de porosités nominales de 0.5 μm (générant des bulles de 0.2 mm à 1 mm) et 100 μm (générant des bulles de 1 mm à 5 mm), respectivement. Des proportions variées de débits d'air ont été injectées à travers chaque aérateur à bulles. Les résultats ont démontré des distributions bi-modales pour lesquelles les proportions réelles et calculées correspondent à l'intérieur d'une déviation de moins de 15%, jugé satisfaisant considérant la sévérité du test. Cependant, puisque la déviation est en corrélation avec la vitesse superficielle du gaz (J_g), le biais était régulièrement vers des bulles plus petites. Les résultats n'ont pas été suffisant pour révéler la nature de ces interactions.

La technique a été démontrée pour un sytème de flotation à l'échelle industrielle, où elle a été comparée à une technique capillaire. Elle a aussi été utilisée pour déterminer le flux d'aire de surface des bulles (S_b) pour une cellule de micro-flottation, en créant un test de la relation proposée entre la constante du taux de flottation k et S_b pour la zone de pulpe.

ACKNOWLEDGEMENTS

I wish to express my sincerest appreciation and utmost gratitude for the continuous encouragement, guidance and moral support received from my research director, Prof. J. A. Finch. His enthusiasm, wisdom and everlasting generosity stimulated my interest in the field of Mineral Processing.

I would like to thank Prof. André Laplante, Dr. C. O. Gomez, Dr. R. Rao and Mr. J. E. Nesset for valuable suggestions and fruitful discussions. I greatly appreciate the assistance received from my colleagues and friends, Mr. J. A. Torrealba-Vargas and Mr. Ryan Cunningham, with whom I shared various aspects of this investigation. I also would like to express my appreciation to the members of my research group, Mr. Grant McSorely, Ms. Marta Bailey, Ms. Helin Girgin, Ms. Dominique Lascelles, and especially to Dr. Stephanie Gelinas for her help in translating the abstract of this thesis. Thanks to Mr. Alain Gagnon and Mr. Roberto Tariello for their suggestions in the assembly and construction of the equipment. I also extend my gratitude for the financial support received from the Natural Sciences and Engineering Research Council of Canada, the sponsors of the Industry Chair in Mineral Processing (Corem, Falconbridge, Inco, Noranda, SGS Lakefield Research, and Teck Cominco), the North American sponsors of the P9M project (Teck Cominco, Inco, Noranda, Clifts Mining and Phelps Dodge), the National Council for Science and Technology of Mexico (CONACYT) and the Mexican Ministry of Education (SEP), in the form of teaching and research assistantships.

Finally, I would like to express my love to my parents and my wife for their patience and unconditional support.

TABLE OF CONTENTS

LIST OF FIGURES

LIST OF TABLES

CHAPTER 1

INTRODUCTION

Originally developed about a century ago, flotation today is the most widely used separation process in the mineral processing industry. In its basic form, flotation consists in dispersing gas (usually air) bubbles into a vessel containing solid particles suspended in an aqueous (pulp) phase. By adjusting the chemical composition of the system, target (hydrophobic) mineral particles in the pulp adhere to the surface of the bubbles. The bubble-particle aggregates float and reach a stable (froth) phase which is removed to recover the minerals. Production of small bubbles (typically < 3 mm) and froth stabilization is promoted by the addition of surfactants (frothers) which prevent bubble coalescence.

To understand the physical interactions that govern the process, accurate information of a number of pulp phase gas dispersion parameters is required among which bubble size is one of the key. Bubble size governs the surface area over which solid particles and bubbles interact, and contributes significantly to system hydrodynamics, which impacts process performance. Notwithstanding this, few techniques are available to measure bubble size which can operate at any scale from laboratory to plant. Furthermore, validation studies of these techniques are rare in the literature.

Sizing bubbles in the pulp phase is difficult because of the high concentration of bubbles and solid (dark) particles the latter reaching 40% by weight in industrial systems

(Nelson et al., 2002). This, for example, renders the system opaque impeding visualization methods. The techniques have to be robust to perform in the concentrating plant environment where flotation cells may be difficult to access, dusty and vibrating, as well as to survive the erosive/corrosive conditions prevailing in a three-phase agitated system.

Measuring bubble size has been the subject of extensive scientific and engineering research. A high degree of sophistication has been achieved in the development of non-invasive techniques including: ultrasound, tomography and radiography imaging, nuclear magnetic resonance imaging (NMR), and velocimetric techniques (laser-doppler anemometry (LDA), particle image velocimetry (PIV), etc.). However, they are usually too complex and involve rather expensive equipment to be implemented in industrial flotation systems.

Two methods have been used successfully in plant, the sampling-followed-by-imaging technique pioneered by Jameson and Allum (1984) and the capillary technique of Tucker et al. (1994). The second is addressed first.

Tucker et al. (1994) developed a method (known as the University of Cape Town (UCT) bubble size analyzer) to separate bubbles from the pulp into a chamber (reservoir) filled with a clear liquid in which a funnel-ended capillary tube was placed. To measure individual sizes, a fraction of the bubbles was suctioned into the capillary tube where they were converted into slugs and their lengths and velocities measured with two optical detectors. The total volume of gas captured by the capillary tube was measured and individual bubble sizes were determined as a fraction of this total volume assuming spherical bubbles. The UCT bubble size analyzer is the technique that has been mostly used in the few available gas dispersion related industrial-scale studies to date (e.g., Gorain et al., 1995; Gorain et al., 1997; Gorain, 1997; Deglon et al., 2000). However, objections to the technique have been reported recently: Grau and Heiskanen (2002) discussed that breakup may occur as bubbles enter or flow in the capillary tube, particularly for large bubbles (> 3 mm). In addition, the capillary is prone to occlusion from particulates in the dispersion. Besides difficulties associated in replacing blocked capillaries on site, significant blockage may cause a gradual reduction in slug velocity. Also, there is a perception in the industry that the technique is cumbersome and not sufficiently robust for plant use.

The work of Jameson and Allum (1984) pioneered the attempt to measure bubble size under industrial conditions. Their approach (referred to here as the sampling-followed-by-imaging technique), consisted in directing a sample of bubbles into a viewing chamber filled with a non-coalescing "clear" liquid (frother containing water) in which bubbles were readily exposed and imaged. A total of 44 flotation machines with different mechanical designs were surveyed revealing a broad range in average bubble size (0.24 mm < number mean diameter < 1.57 mm). As indicated in their report, automatic image processing was projected. However, the frequently reported problems associated with analysis of this type of images (e.g., overlapping, blurring, clustering, etc.) impeded the task. The bubbles were sized manually, an arduous and time-consuming process, which permitted only a small number of bubbles to be computed (ca. 250), a situation that still holds (Chen et al., 2001).

This thesis explores the sampling-followed-by-imaging technique and offers some solutions through innovative design, automated data processing, and importantly, executes validation tests.

1.1 Structure of the Thesis

Chapter 2 includes an extensive review of techniques to measure bubble size in a broad range of applications. Chapter 3 gives the description of the technique under consideration. To illustrate its applicability, Chapter 3 also includes the results of an exercise in which the effects of frother dosage and airflow rate were evaluated in an industrial-scale mechanical flotation cell. Chapters 4 and 5 address the image and sampling validation studies, respectively. In Chapter 6 the technique is compared with the UCT bubble sizing method in a plant-scale mechanical flotation cell. Chapter 7 illustrates a laboratory-scale application with an attempt to establish the impact of bubble size and gas rate on recovery of single minerals in a micro-flotation cell. Although Chapters 4 to 7 contain conclusion sections, overall conclusions comprise Chapter 8.

CHAPTER 2

LITERATURE SURVEY

Techniques capable of measuring bubble size in multiphase flows are usually classified depending upon their operating principles.

2.1 Electroresistivity techniques

A commonly used method for bubble size measurement is the two-electrode conductivity probe (Hewitt, 1978; Thang and Davis, 1979). Such a probe consists of two needles which are fixed a small vertical distance apart. Each of the sensors has a binary output signal depending on which phase is in contact with the tip. As a bubble passes, the time delay t between signals from the two sensors measures the time for the bubble to proceed from one probe tip to the other. The distance L between the tips being known, the velocity component of bubble i along the direction defined by the line joining the tips can be estimated as:

$$u_i = L / t_i \tag{2.1}$$

This velocity along with knowledge of the mean residence time of the bubble at one of the probe tips t_r can be used to estimate the pierced chord length of the bubble as:

$$l_i = u_i \, t_{ri} \tag{2.2}$$

With this method there are variations in bubble frequency and the corresponding chord lengths obtained using the measurements from the upper and lower sensor. If such variations are statistically significant, this is indicative of problems of cross-talk and capacitive effects. This implies that the sensors are too closely spaced. The optimum separation between the sensors is unfortunately a function of the bubble frequency, the range of bubble chord lengths intercepted by the sensors as well as the sensor size and geometry.

There are potential problems in applying this method to multiphase flow. Bubbles that are rising in a direction not aligned with the two probes lead to major errors, since it is possible that there is no delay in the signal from the two sensors. This seriously limits their use in turbulent flow fields. To overcome this difficulty some researchers have developed multi-point probes (Burgess and Calderbank, 1975; Raper et al., 1982). However, these probes can be utilized only in flows where the bubble size is at least 6 mm (Buchholz et al., 1981). The velocity, as calculated by Equation 2.1, is applicable only if the bubble is centrally pierced. Steinemann and Buchholz (1984) provide an alternative procedure for calculating the rise of bubbles that are not centrally pierced. This is based on assuming a probability density function for the bubble chord distribution, the parameters for which are fitted to the measured chord distribution. If the bubbles are small (< 1 mm), there is the possibility that a bubble never gets pierced but goes around the sensing probe tips. Svendsen et al. (1998) have used this method to measure axial and radial bubble size and bubble velocity variations in columns for air/water and CO_2/N_2/aqueous MDEA (Methyldiethanolamine) systems. In order to eliminate the effects of cross-talk between two closely positioned sensors an alternative method of acquiring the mean time delay between the signals from the two tips is to obtain it from the cross-correlation function between the signals (Zun and Saje, 1982). In summary, the two-point probe is an acceptable instrument for measuring bubble characteristics only if the bubbles are spherical and not too small.

2.2 Ultrasound techniques

Ultrasound reflection techniques offer a way to determine bubble size distribution in multiphase flows. It is known that bubbles have a resonance frequency that is inversely proportional to the radius of the bubble. This fact has been exploited for detection and estimation of bubble size (Hilgert and Hofmann, 1986; Luebbert et al., 1987; Broering et al., 1991). Bubbles are excellent sound scatters and have a characteristic resonant frequency dependent on their sizes (Cathignol et al., 1988).

2.3 Optical techniques

2.3.1 Optical fibers

Optical fibers exploit differences in the index of refraction of air/liquid phases and rely on the application of Snell's law at the probe-fluid interface. Depending on which phase is present at the probe tip the light from the tip is reflected or refracted. The most common optical probe consists of two optical fibers fused and ground to a 45° angle with respect to the probe axis. The other ends of the fibers are free with one of them serving as an emitter and the other as a receiver. Light detection can be achieved with a phototransistor. The principle of detecting bubble size and velocity is identical to that of the two-point conductivity probe described above. Measurement of bubble size using optical probes is reported by De Lasa et al. (1984), Saxena et al. (1990) and Saberi et al. (1995). In general, an optical probe can be used only in transparent systems and at low gas holdup (volume fraction of gas). The success of the probe in discriminating between the phases depends on good contact between the probe tip and the bubble. Thus, if the bubble size was too small the probe would be unable to detect variations. The use of optical probes in a three-phase system is also considered problematic (Euzen, 1993).

2.3.2 Laser-Doppler anemometry

There are basically four distinct varieties of laser-doppler anemometry (LDA). The first utilizes a relationship between bubble size and a characteristic signal such as doppler amplitude or modulation depth. The technique is most readily applied to bubble sizes up to a few hundred micrometers (Yule et al., 1977; Ungut et al., 1978; Lee and Srinivasan, 1978) although Martin et al. (1981) obtained a unique relationship between signal visibility and bubble size for diameters up to one millimeter. At its best, this approach is therefore restricted to rather small bubbles.

The second variant of LDA is that described by Durst and Zare (1975). In their technique the two light beams, either reflecting off or refracting through the bubble, generate interference fringes in the surrounding space. Bubble size can then be calculated from the fringe spacing. The main difficulty with this method appears to be the measurement of moving fringes as bubbles pass though the beam. In the third variant, Lee and Srinivasan (1982) combine LDA determined bubble velocities with reference beam blockage times to yield diameters. This technique appears capable of yielding high quality size information, but it requires rather involved signal processing.

The fourth variant is that of Semiat and Dukler (1981). In their work, the light fringes required for LDA are generated by Ronchi gratings rather than crossed beams. This serves to simplify the optics and make the overall approach more workable. Their work shows size distributions with relatively large bubbles (diameter up to several millimeters). Even so, the approach is still fairly complex to be implemented in practical mineral processing conditions and its use was only demonstrated in bubbly flows of low bubble number density.

2.3.3 Other laser-based techniques

Meernik and Yuen (1988a, 1988b) reported a technique to determine the size distribution of bubbles in two- and three-phase systems. This method involved passing a narrow laser beam through the system and monitoring the transmitted light intensity. In this case, the light beam diameter should be less than the diameter of the smallest bubbles for which data are desired. By assuming the distance of closest approach between any bubble center and beam axis to be random, a statistical analysis of the data collected yielded size distributions. As in the case of LDA, this technique does not appear suitable for implementation in plant-scale reactors.

2.3.4 The isokinetic collection probe

Another optical technique to measure bubble size is the isokinetic sampling probe (the term isokinetic refers to the condition in which bubbles are collected at uniform velocity regardless of their size). Its measurement principle is based on sampling (suctioning) bubbles from the dispersion into a capillary tube. The end of the capillary is funnel shaped with an expansion such that it provides a uniform acceleration as the bubbles become converted into cylinders (slugs) filling the capillary cross-section. A narrow collimated beam of light from an optical switch is directed through the glass wall of the capillary tube. The measured signal consists of the variation in intensity of the transmitted light due to the passage sequentially of gas and liquid slugs. These signals are similar to those of the conductivity or optical probes (i.e., are binary). The time elapsed between the detection of the two ends of a bubble is inferred from the signal. This, along with the known cross-sectional area of the capillary, can be used to estimate the bubble volume (Equation 2.3):

$$V_i = \left(\frac{t_{ri}}{t_i}\right) LA \tag{2.3}$$

where, A is the cross-sectional area of the capillary

L is the distance between the optical detectors

t_i is the time elapsed between the detection of the two ends of bubble i

t_{ri} is the bubble period (or residence time) of bubble i

(note that $u_i = L / t_i$ as in Equation 2.1)

Assuming that the bubble is a sphere an equivalent spherical bubble diameter can be computed. Employment of this technique in two-phase (air-water) dispersions is reported (Greaves and Kobbacy, 1984; Barigou and Greaves, 1991; Barigou and Greaves, 1992; Lammers, 1994); in three-phase (air-water-paper) pilot-scale flotation deinking cells (Hunold et al., 1997); in flotation columns with air-water-coal systems (Reddy et al., 1988; Biswal et al., 1994).

The choice of a suitable capillary size is a function of the smallest bubble to be detected. Bubbles smaller than the capillary diameter are not optimally transformed into slugs and, therefore, give rise to signal pulses which are not of sufficient amplitude and width to be reliably measured. On the other hand, reducing the capillary size further may cause bubble breakup inside the tube, in addition to it becoming prone to blockage from particulates in the dispersion. The minimum bubble size detected by this technique appears to be ca. 0.3 mm. Another limitation is that any significant blockage of the capillary may cause a reduction in slug velocity. Under conditions of severe contamination, as likely in the case of slurries of high solids concentration, the effect of reduction in slug velocity can be important.

A variant to the isokinetic sampling probe is that introduced by Randall et al. (1989). This method is often referred to as the University of Cape Town (UCT) bubble size analyzer. The difference is that in the UCT method individual bubble volumes are calculated indirectly as fractions of the total sampled volume, otherwise stated:

$$V_i = \frac{(t_{ri}/t_i)}{\sum_i (t_{ri}/t_i)} \sum_i V_i \qquad (2.4)$$

where, $\sum_i V_i$ represents the total sampled gas volume which is measured with a burette

As inferred from Equation 2.4, the determination of L and A is obviated. The approach was intended for two- and three-phase systems; however, its use was limited to low solids concentration due to capillary blockage.

2.3.5 The sampling-followed-by-isokinetic-collection technique

The need to size bubbles in industrial flotation systems where solids concentrations can be high motivated the development of a modification to the UCT bubble size analyzer. The modification (Tucker et al., 1994) consisted in directing a sample of bubbles into a chamber (reservoir) filled with a non-coalescing liquid (frother containing water) in which bubbles, now "clear" of solids, were readily suctioned by the capillary. In the present work, this approach is referred to as the sampling-followed-by-isokinetic-collection technique (Figure 2.1).

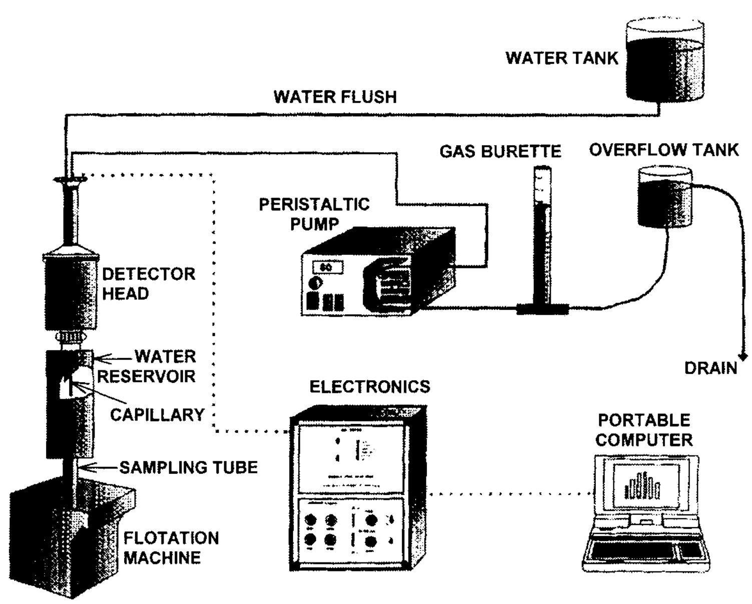

Figure 2.1. The UCT bubble size analyzer (after Tucker et al., 1994)

The UCT bubble sizing method has been used in a number of laboratory and industrial-scale studies, e.g., Aldrich and Feng (2000); Gorain et al. (1995); Gorain et al. (1997); Gorain (1997); Deglon et al. (2000); Steinmuller (1999). A deterrent is that it contains a significant number of components which combine to render the system cumbersome for industrial use. It has also been observed that, under inappropriate conditions (e.g., capillary size, suction rate, etc.), bubble breakup may occur (Grau and Heiskanen, 2002). Studies directed to establish the optimum conditions are scarce in the literature.

2.3.6 The imaging technique

The simplest approach would seem to be the imaging technique. Studies in which images are used to size bubbles proliferate in the literature. In the most common setup, pictures of the dispersion are taken through windows installed in the vessel wall while real sizes are obtained by placing an object of known size (usually a ruler) in the focus plane. Automatic sizing through image analysis routines have not been extensively implemented due to the common practical and fundamental problems associated with this method. For example, a fundamental problem that is not frequently discussed is the impact of the "inherently variant" distance between the focus plane and the bubble (i.e., the oscillating nature of the bubble motion causes the distance between the bubble and the focus plane to vary), which is particularly problematic as the bubble path depends on bubble size. Other fundamental problems include the influence of optical conditions, e.g., optical system quality (aberrations, non-linear response, lighting characteristics, etc.).

Practical problems are well documented: overlapping, blurring, bubble clustering, poor contrast, etc.

Also, the technique is limited to measurements close to the vessel wall impeding the establishment of spatial (point) distributions. In addition, the system needs to be transparent with low bubble concentration otherwise the optical path can become obscured. Therefore, this is not a straightforward approach in an industrial-scale system. Most of the studies reported have been carried out in the laboratory (Reynolds, 1992; Takahashi et al., 1992; Vigneault et al., 1992; Orsat et al., 1993; Miyahara and Hayahino, 1995; Lin et al., 1994; Pamperin and Rath, 1995; Varley, 1995; Tsuge et al., 1997; Humeres et al., 1999; Lage and Esposito, 1999).

2.3.7 The sampling-followed-by-imaging technique

A variant of the imaging technique is to direct a sample of the bubbles into a viewing chamber to expose them for imaging. In some cases, liquid (bearing bubbles) is withdrawn from the dispersion (Parthasarathy et al., 1991; Parthasarathy and Ahmed, 1994; Ahmed and Jameson, 1995; Parthasarathy and Ahmed, 1996; Deglon, 1998; Hui, 2000). However, this approach is applicable only when the liquid-phase is translucent. An alternative to size in systems with high solids concentration is to allow the bubbles to ascend into the viewing chamber by their natural buoyancy. Jameson and Allum (1984) first described this concept. Their work appears to be the first attempt to conduct a systematic survey of bubble sizes in industrial flotation cells. Indeed, the bubble sampling procedure of Tucker et al. (1994) (i.e., the UCT bubble sizing technique) was inspired by the approach of Jameson and Allum. The approach has been used for sizing bubbles in coal flotation (Yoon and Luttrell, 1986), for the visualization of bubble–particle (Zhou et al., 2000) and bubble-bitumen aggregates (Malysa et al., 1999), in a laboratory-scale flotation cell (Grau and Heiskanen, 2002), in a pilot-scale cell processing a sulphide ore (Chen et al., 2001), and in an industrial-scale cell (Yianatos et al., 2001). However, the same difficulties associated with the imaging method (overlapping, blurring, bubble clustering, contrast, etc.) were present.

Hernandez-Aguilar et al. (2002) introduced a concept (which is the subject of the present study) consisting in angling the viewing chamber. This simple expedient along with a proper configuration of diffuse backlighting provided high contrast, while bubble overlapping and bubble blurring were reduced. The quality of the images was such that a simple computational routine could be applied to analyze the images automatically. In this thesis, the technique is described in detail and the sizing and sampling procedures are validated against independent measurements.

CHAPTER 3

DEVELOPMENT OF THE TECHNIQUE

The proposed technique introduces an innovative variation to the sampling-followed-by-imaging technique by angling the viewing chamber. This simple expedient reduces bubble overlapping, and concentrates bubbles along the focal plane which reduces bubble blurring and, along with appropriate arrangement of diffuse backlighting, provides high contrast. Figure 3.1 illustrates a typical design. Examples of images are given in Figure 3.2.

3.1 Hardware

The system comprises a sampling tube attached to the bottom of the sealed viewing chamber. The typical diameter of the sampling (plastic) tube is 1.27 cm and its length usually varies between 1.5 and 2.5 m depending on the flotation cell configuration (typically, the length of the tube is adjusted to sample at ca. 0.5 m below the pulp–froth interface). The viewing chamber (31.7 x 22.1 x 13.0 cm) is made of plastic (PVC) with two facing glass windows. An aluminum frame along with an o-ring joint is used to seal the windows against the chamber. The viewing chamber, digital camera and light source are supported on an aluminum structure that makes the device light enough to transport and mount. A light diffuser is attached to the back window to enhance contrast. A description of the components is given in Table 3.1.

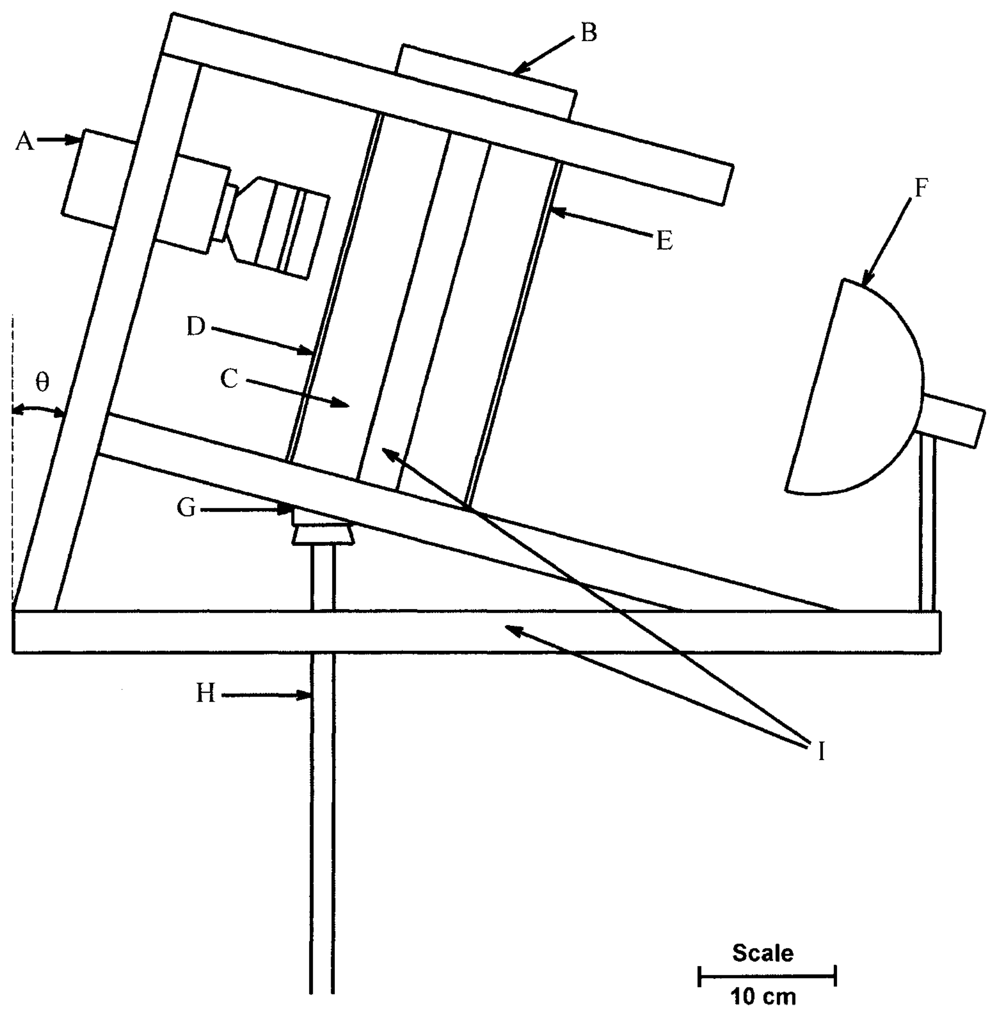

Figure 3.1. Scaled diagram of the device used in the sampling-followed-by-imaging technique with the inclined window and using diffuse backlighting. A: digital camera, B: filling cap, C: viewing chamber (bubble viewer), D: front window, E: back window, F: lamp, G: bubble viewer inlet, H: sampling tube, I: aluminum square bars (for support), θ: angle of the inclined window.

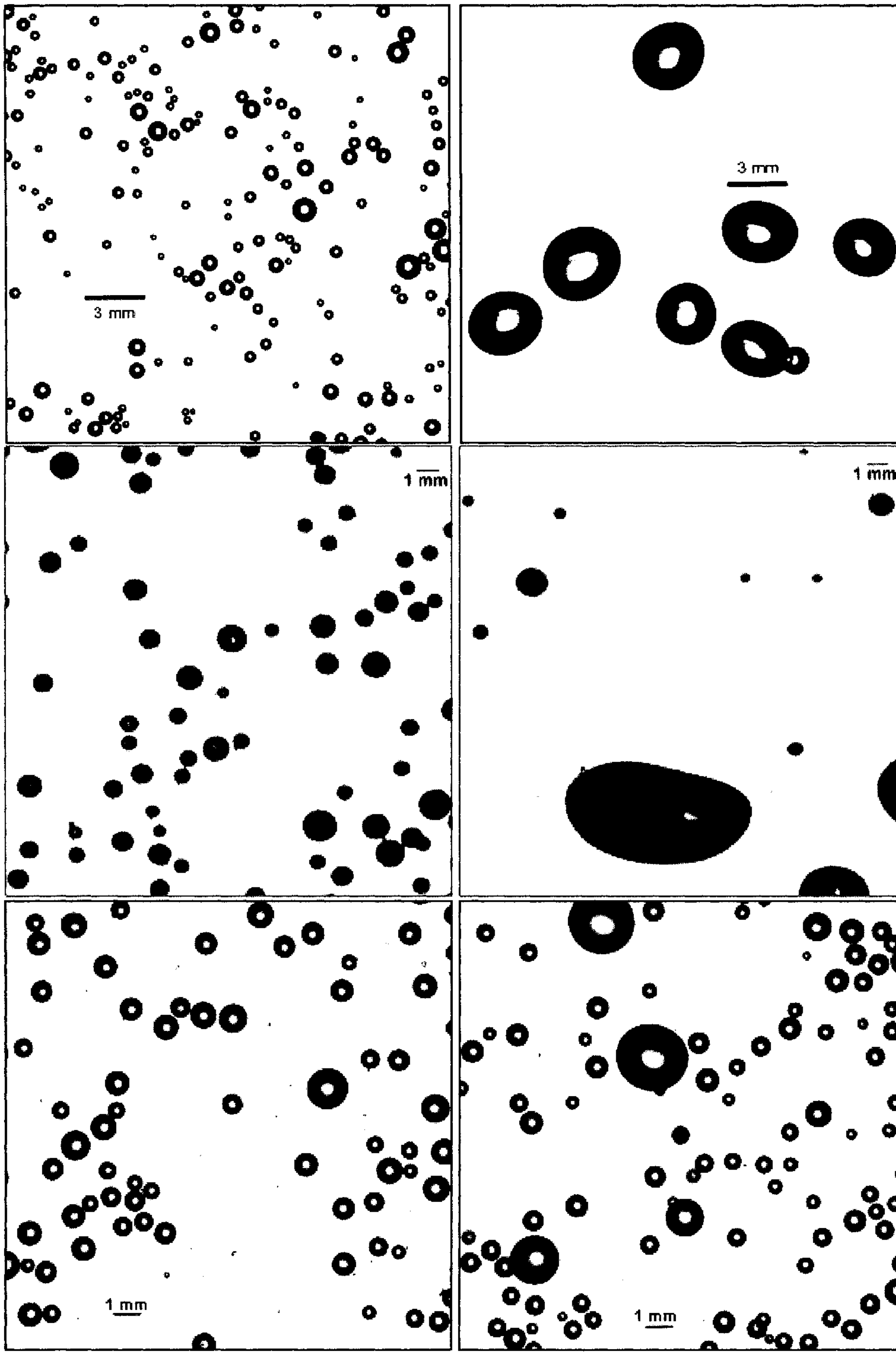

Figure 3.2. Examples of images. Top left: bubbles generated in a fine-porosity sparger (air-water); top right: in a coarse-porosity sparger (air-water); mid left: in a mechanical flotation machine processing a base metal ore; mid right: bubbles showing a wide size distribution generated by a jet-type sparger processing a base metal ore; bottom left: in a mechanical flotation machine processing a PGM (Platinum Group Metals) ore at a low aeration rate; bottom right: processing the PGM ore at a high aeration rate

Table 3.1. Specification of the components illustrated in Figure 3.1

Tag	Component name	Material	Description
A	Digital camera	——	Qimaging Retiga 1300
B	Filling cap	PVC	For filling and cleaning
C	Viewing chamber	PVC	Made of 0.5 cm thickness PVC plates
D	Front window	Glass	0.4 cm thickness
E	Back window	Glass	0.4 cm thickness
F	Lamp	Aluminum	660W manufactured by Acme Lite
G	Chamber inlet	PVC	4.1 cm O.D. and 3.3 cm I.D.
H	Sampling tube	PVC	2.1 cm O.D. and 1.27 cm I.D.
I	Support	Aluminum	Square bars 3 x 3 cm (Katim Products)

3.2 Operating procedure

An image with a transparent ruler placed in the focus plane (the underside of the window) is acquired to determine the image magnification factor. A rubber plug is placed to seal the sampling tube permitting immersion in the cell. The viewing chamber is filled via the filling cap with a solution of frother in water. Then, the filling cap is closed (sealing the viewing chamber) and the plug removed permitting the bubbles to enter. Images are recorded once the stream of bubbles becomes steady (typically 45 s for a 2.5 m tube).

The width of the bubble swarm spreading over the window varies from 3–4 cm (for a low concentration of bubbles with uniform sizes) to 8–9 cm (for a concentrated bubble population with broad size distribution). It has been observed that, in some cases (particularly non-uniform distributions), large bubbles displace small bubbles, i.e., the large bubbles tend to rise near the center of the window whereas the small bubbles move close to the swarm edge. To capture a representative area, the camera is positioned in such a way that one edge of the image corresponds to the window center, i.e., the swarm is assumed to be symmetric across the center of the window.

3.2.1 Software

The philosophy underlying development of the technique was to maximize image quality through hardware optimization in order to minimize the number and complexity of image analysis operations. The quality of the images illustrated in Figure 3.2 permits their analysis through a rather simple automatic routine. The steps followed to compute size distributions are the following: (1) collecting a number of digital images (usually 300) taken at uniform time intervals (1 s), (2) applying a threshold to distinguish objects within the image, i.e., isolated bubbles and clusters, (3) eliminating the bubble clusters using a shape factor criterion, (4) sizing the remanent objects (mostly isolated bubbles), and (5) grouping them into size classes. Neither contrast enhancers nor image filters are employed.

A commercial image analysis software package (Northern Eclipse 6.0) is used both to control the image capturing routine and to process the images. The digital camera has an IEEE 1394 interface that allows the transfer of full-resolution images directly onto the hard disk of a computer without the need of a frame grabber. This permits storage and analysis of a large number of images using a general purpose portable computer. Images are stored as 8-bit (256 intensity gray levels) monochrome TIFF files.

Due to the image contrast and background uniformity, the uncertainty associated with the threshold selection is significantly reduced. However, for the sake of consistency, the threshold is routinely set to half the intensity level, i.e., it is set to grey-scale value of 128 for the case of maximum contrast (i.e., when the average background grey scale value is 255 (white) and the minimum bubble grey scale value is 0 (black)).

In the case of systems with solids, the image background darkens gradually because the viewing chamber becomes turbid as particles accumulate after their release when the bubbles burst. In this case, the analysis is divided in batches of images (typically 50). Using the last frame of each batch, the threshold is set to half a "normalized" intensity level, i.e., relative to a characteristic (average) background value of the batch. Images are analyzed until the average background grey scale value is 25 (i.e., ca. 10% of the total grey scale).

The shape factor criterion used to select single bubbles is defined as:

$$SF = \frac{4\pi A}{P^2} \tag{3.1}$$

where A and P are the area and the perimeter of the object (bubble), respectively. A SF of one indicates a circle. As the value approaches zero, it indicates an increasingly elongated polygon. Therefore a single bubble will have a value close to one whereas a cluster will deviate from unity: all objects with a SF < 0.6 are rejected. (This criterion is discussed in detail later.)

The software outputs a number of parameters (area, perimeter, maximum diameter, minimum diameter, etc.). For each bubble, the maximum and minimum axis are computed and an equivalent spherical bubble diameter is obtained from:

$$D_b = \sqrt[3]{D_{\max}{}^2 D_{\min}} \qquad (3.2)$$

where D_{max} and D_{min} are the maximum and minimum diameters, respectively. Equation 3.2 makes the common assumption that the bubble is an oblate spheroid (Polli et al., 2002). Usually between 10 000 and 30 000 bubbles are sized.

Three mean diameters are routinely calculated: (1) the number mean D_{10}, (2) the Sauter mean D_{32}, and (3) the volume moment D_{43}, which are defined by Equation 3.3:

$$D_{mn} = \frac{\sum_{i=1}^{i=n_t} D_{b_i}{}^m}{\sum_{i=1}^{i=n_t} D_{b_i}{}^n} \qquad (3.3)$$

where, $m = 1$ and $n = 0$ for the number mean,

$m = 3$ and $n = 2$ for the Sauter mean,

$m = 4$ and $n = 3$ for the volume moment,

D_{bi} is the size of bubble i, and

n_t is the sample size

3.3 Evidence of measurement sensitivity

It has been observed that, besides the practical gains, the technique provides sensitive measurements. An example is given as follows.

3.3.1 Effects of frother addition and airflow rate

One role of frothers in flotation systems is to maintain a population of small bubbles by retarding coalescence. Figure 3.3 illustrates the variation of the number mean (D_{10}) and the volume moment (D_{43}) with airflow rate in a 130-m^3 nominal capacity flotation cell (model Outokumpu OK-130-TC) at various frother dosages in g/t of dry ore. (Tse et al. (2003) discussed the relevance of including both the D_{10} and the D_{43} mean diameters when evaluating systems in which bubble coalescence occurs.) The cell was located at Impala Platinum's Merensky concentrator in South Africa.

It can be seen that the D_{43} follows a consistent increasing trend with airflow rate. However, it is deduced that at 30 g/t coalescence was occurring because the values were significantly larger than those at 65 and 100 g/t. No significant difference was obtained between the mean diameters at 65 and 100 g/t, therefore, the trend (dashed) line was calculated by combining both. It is well documented that bubble size decreases quickly with frother dosage to some concentration above which the effect is minimal (Klassen and Mokrousov, 1963). Recently, Cho and Laskowsy (2002) referred to this concentration as the CCC (critical coalescence concentration). Therefore, at 30 g/t the plant was operating below the CCC and at 65 g/t the plant was above the CCC. The impact of increasing gas rate increasing the bubble size is also well known (Gorain et al., 1995). The significance here is the ability, for the first time, to detect these trends in full-scale industrial flotation cells.

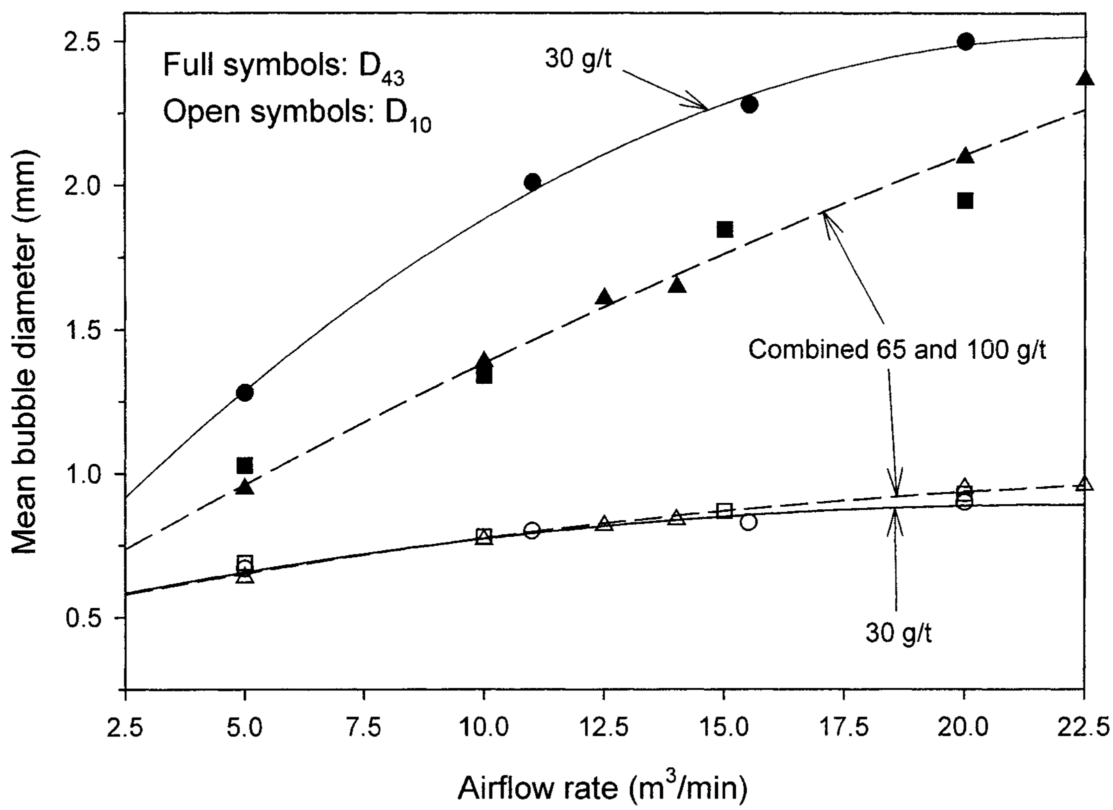

Figure 3.3. The effect of airflow rate on mean bubble diameter at various frother dosages (Sasfroth 2000). Circles: 30 g/t, squares: 65 g/t, triangles: 100 g/t

In contrast to D_{43}, the results show that the D_{10} is little affected by change in frother concentration. The D_{10} mean is most influenced by the number of small bubbles, the change in the number of the relatively few but large bubbles due to coalescence events having little consequence. This difference between D_{10} and other metrics, e.g., D_{43}, can be used to monitor changes in the width of the distribution (e.g., Figure 3.4). On close inspection of Figure 3.3, the D_{10} actually appears to decrease at the highest air rates, and lowest frother dosage. This may be a consequence of coalescence. Tse et al. (2003)

show that a coalescence event produces daughter bubble fragments, i.e., it increases the number of small bubbles. The sensitivity of the sampling-followed-by-imaging technique may be sufficient to reveal this phenomenon.

The thesis will discuss other results showing the sensitivity of the technique, the example here serving the purpose of introducing this feature.

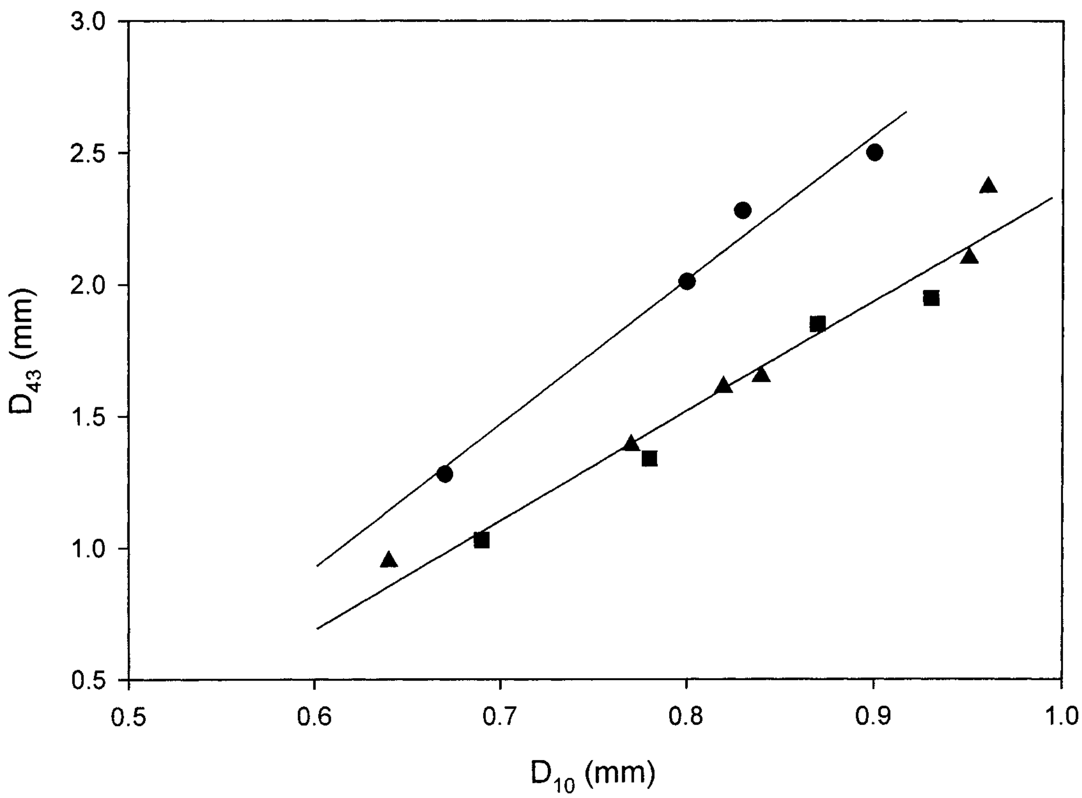

Figure 3.4. The effect of frother addition on the $D_{43} - D_{10}$ difference. (Note the significant difference between the D_{10} and the D_{43} indicating the presence of large bubbles. Symbols as in Figure 3.3.)

3.3.2 Implications

Recent studies have suggested that the pulp zone rate constant, k, is linearly dependent on the bubble surface area flux, S_b (Gorain et al., 1997; Hernandez et al., 2001). The S_b is defined by:

$$S_b = 6\, J_g / D_b \tag{3.3}$$

where, J_g is the superficial gas rate (i.e., the airflow rate divided by the cross-sectional area of the flotation cell), and

D_b is the bubble diameter (usually the Sauter mean, D_{32})

The relationship is usually expressed as $k = P\, S_b$ where P is the "floatability factor" which encompasses the contribution of particle size and hydrophobicity.

In principle, it is possible to quantify the functionality between airflow rate and mean bubble diameter for a given mechanism provided that the technique gives consistent measurements. Figure 3.5 illustrates the relationship between D_{32} and airflow rate for the case discussed in the previous section. (The J_g was measured with a technique developed by Torrealba-Vargas (2004).) The derived S_b is also given in the Figure. It can be seen that the relationship $J_g - S_b$ varies with frother addition. Gorain et al. (1999) proposed an empirical model to predict S_b. Their model neglects the impact of frother dosage as they considered that, in most practical (industrial) conditions, concentration variations do not impact bubble size significantly, i.e., they assumed that most flotation plants operate close to or above the CCC. This assumption can now be tested with recent instrument developments, not least the bubble size analyzer described in this thesis. One reason given for the development of an empirical model to predict S_b is the difficulty in measuring the J_g and D_b required to estimate S_b. The instrumentation being developed will greatly reduce the difficulty.

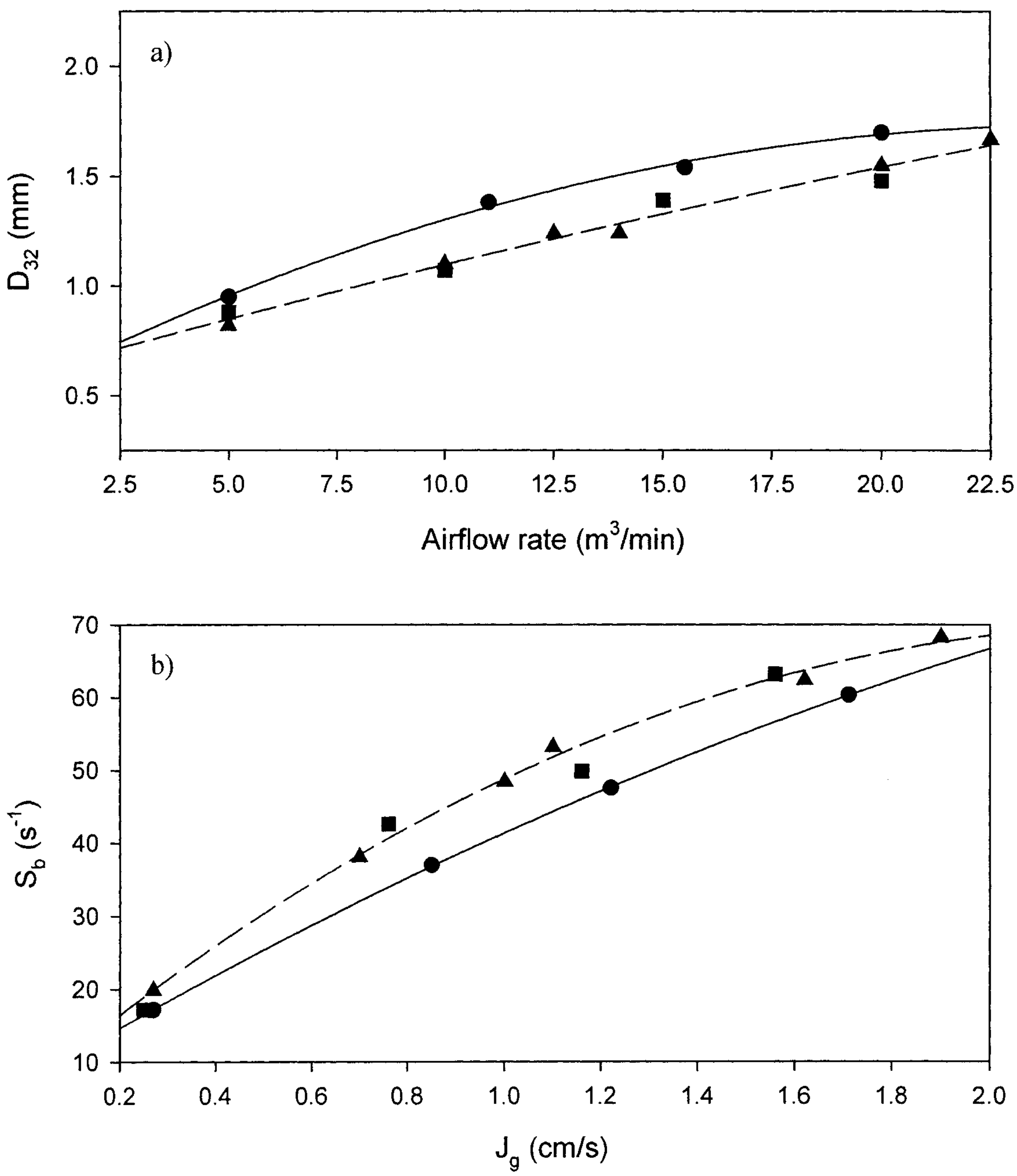

Figure 3.5. a) Variation of Sauter mean (D_{32}) with airflow rate; b) Variation of bubble surface area flux (S_b) with superficial gas velocity (J_g) (symbols as in Figure 3.3)

3.4 The need of validation

The proposed bubble sizing technique has been well received and is being used by several companies as well as the Mineral Processing Group at McGill University. Gorain (2002) writes:

> "Some sophisticated techniques (robust for plant applications), have been developed recently to carry out these [gas dispersion] measurements, which the industry is finding very useful (Hernandez-Aguilar et al., 2002)"

However, despite wide acceptance, the measurements require validation. The validation involves, on the one hand, the determination of the accuracy of sizing an individual bubble image; on the other, verifying that the sample is representative of the actual population and that the image analysis operations do not eliminate valuable information that may distort the size distribution.

CHAPTER 4

IMAGE VALIDATION

4.1 Background

Studies in which images are regarded as the standard (or reference) source of bubble size data abound in the literature. However, investigations aimed to validate the images are scarce. This has led to a variety of inconsistent and, occasionally, subjective approaches. A common practice is to use diffuse (incoherent) backlighting because it provides better contrast as opposed to being illuminated from the front-side. Under this configuration, the bubbles are visualized as opaque hollow-objects on a bright background. This condition is generally considered favourable since the sizing process can be automated with an image analysis system, for example using a threshold criterion. The fact that the transition from (clear) background to (dark) bubble occurs gradually (i.e., an intensity gradient exists near the bubble edge) has caused recurrent discrepancies. In addition, the local background value varies depending upon the image-sensing device used and the lighting quality; this background value is not often reported. As examples of the variety of threshold settings: Tassin and Nikitopoulos (1985) selected the threshold level where the grey-scale (intensity) gradient was maximum; Harvey et al. (1996) varied the threshold arbitrarily between 100 and 120 on a grey scale of 256 (i.e., between ca. 39% and 47% of the total scale) where the average local background value was not given; Duraiswami et al. (1998) adjusted between ca. 23% and 27% (of the total grey-scale) on the basis of a qualitative (visual) comparison between the images before and after thresholding; and Vigneault et al. (1992) used a constant value of 69%, but relative to a locally normalized grey-scale (i.e., relative to a reported average background value).

Also common is the use of image enhancing algorithms (sharpening filters, contrast enhancers, image equalizers, etc.) along with built-in edge detection and sizing routines which are included in commercial programs based on the premise that if "focalized" bubbles are (artificially) sharpened, then the resulting image silhouette corresponds to the real edge (e.g., Grau and Heiskanen, 2002). When sizing bubble-particle aggregates, Malysa et al. (1999) used a number of contrast enhancers and background equalization filters prior to setting a constant threshold value of 50%.

Another potential source of discrepancy is the occasional misunderstanding of the formation of the shadow. It has been considered (e.g., Rodrigues and Rubio, 2003; Vigneault et al., 1992) that the shadow is formed due to the contribution of direct (non-reflected/refracted) rays only (i.e., light rays in the vicinity of the bubbie edge are totally reflected whereas rays near the center are transmitted and perceived by the camera). This interpretation is erroneous because the size of the light source is large relative to the bubble. Therefore, off-axis rays (i.e., rays that are not perpendicular to the focus plane) are reflected and refracted at the gas-liquid interface causing further internal reflections/refractions, which affect the apparent size. In some cases, this could have dramatic consequences: Leifer et al. (2003) demonstrated that, under certain imaging conditions, the real edge of the bubbles was not within the plausible threshold values but slightly below the local background intensity. This can result because the irradiance level (or intensity gradient) near the bubble edge is governed by intimate and complex relationships among various optical parameters, including: the defocus distance (i.e., the distance between the bubble and the focus plane), the sign of defocus distance (the position of the object relative to the focus plane), the size and position of the light source, the size and position of the entrance pupil (of the objective), and the object (bubble) size itself. The quality of the lens, the sensitivity of image detector and the uniformity (or quality) of the diffused light are also important factors.

The study of Bongiovanni et al. (1997) offers a fundamental methodology (based on geometric optics and photometric laws) to compensate for the effects of direct, reflected and refracted rays and defocus distance (Δ) on imaging size. The method is divided in two steps. First, the bias due to reflected/refracted rays is discounted through an equation expressed in terms of an illumination-related variable, θ_L, which represents the angle under which the bubble "sees" the light source. Second, the bias due to the defocus distance is calculated using information within the image (the intensity gradient near the edge) and thresholding at half the irradiance level. A relevant outcome of Bongiovanni et al.'s work was that precise corrections can be made only if the sign of the defocus distance is known. Moreover, it was concluded that no reliable information regarding the sign of Δ can be obtained from the image.

The present work introduces the novel concept of angling the window (to intercept a stream of rising bubbles) along with a diffuse backlighting (i.e., incoherent) optical system. This combination provides high-contrast while bubble overlapping and bubble blurring are reduced. In addition to these practical improvements, the approach, fortuitously, resolves two fundamental problems: since the motion of the bubble is limited to two-dimensions, the defocus distance is small (because the focus plane is defined as the underside of the window), and more importantly, its position (i.e., its sign) is not ambiguous, it is always negative, i.e., "behind" the focal plane. Provided that the impact of the inclined window is either negligible or correctable, the method of Bongiovanni et al. could be readily implemented for the case of $\Delta < 0$.

This chapter proofs the concept of the inclined window/incoherent imaging system along with a correction procedure based on the method of Bongiovanni et al. An empirical approach was adopted to compensate for bubble deformation caused by the inclined window. Standardized single spherical and ellipsoidal bubbles were generated and sized with the displaced-volume method, which was regarded as the reference.

4.2 Fundamentals

Consider the imaging of a spherical bubble of radius R as it rises on a slightly inclined clean glass (hydrophilic) window, as illustrated in Figure 4.1. The location of the focus plane is the glass-liquid interface (i.e., the underside of the window) and the window inclination angle (θ_W) is measured from a plane parallel to the direction of gravity. Thus, the bubble is inherently non-focused (i.e., its center is located at a (defocus) distance Δ from the focus plane). It should be noted that, although of similar magnitude, R does not necessarily correspond to Δ due to the liquid film between the bubble and the window and bubble distortion due to the angled window. The objective (located at a distance s_P from the focus plane) is characterized by the radius r_P of its entrance pupil (s_P includes the changes in refraction indices through the different media). The scene is illuminated with a diffuse source of radius r_L located at a distance s_L relative to the focus plane.

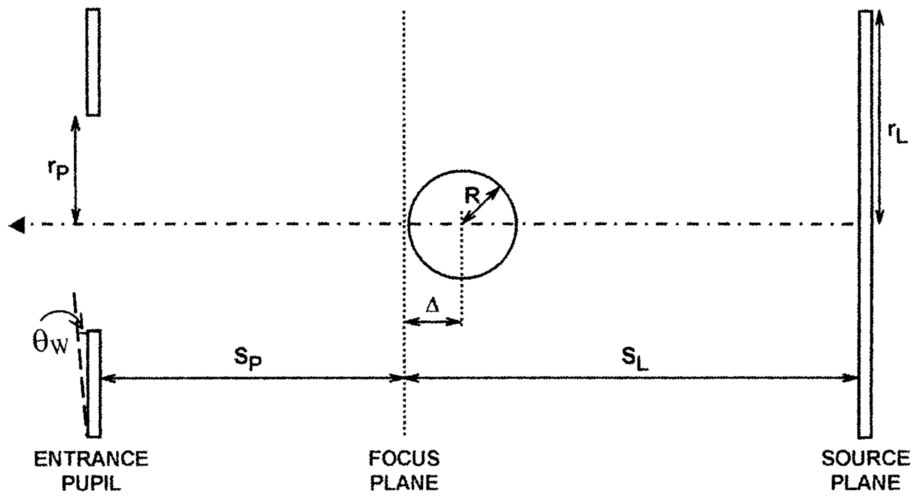

Figure 4.1. Imaging system: parameter definition

It is worth emphasizing the unique characteristics of this system in which the inclined window constrains Δ to be small ($\Delta \approx R$), nearly constant in spite of bubble size (i.e., the bubble motion has been reduced in one dimension), and with its position relative to the focus plane always negative (Δ is defined as negative as the bubble is between the focus plane and the light source).

4.2.1 The Blurred Shadow Model

When the image of a spherical object is formed due to the contribution of direct rays only (as in the case of an opaque object), the irradiance (E) presents universal profiles which can be expressed analytically (Equation 4.1) as a function of the distance, ρ, from the center of the sphere for given Δ:

$$
E(\rho^*) = \begin{cases}
1 & \text{if} \quad \rho^* \geq 1+\Delta^* \\[2ex]
\max\left\{0; 1-1/\Delta^{*2}\right\} & \text{if} \quad \rho^* \leq \left|1-\Delta^*\right| \\[2ex]
1-\dfrac{1}{\pi\Delta^{*2}}\left[\begin{array}{c} \cos^{-1}\left(\dfrac{\rho^{*2}+1-\Delta^{*2}}{2\rho^*}\right) \\ +\Delta^{*2}\cos^{-1}\left(\dfrac{\rho^{*2}-1+\Delta^{*2}}{2\rho^*\Delta^*}\right) \\ -\dfrac{1}{2}\sqrt{2\Delta^{*2}+2\rho^{*2}\Delta^{*2}+2\rho^{*2}-1-\Delta^{*4}-\rho^{*4}} \end{array}\right] & \text{if} \quad \left|1-\Delta^*\right| \leq \rho^* \leq 1+\Delta^*
\end{cases}
$$

(4.1)

where Δ* and ρ* are dimensionless groups defined by:

$$\Delta^* = \frac{|\Delta|\, r_p}{R\, s_p} \tag{4.2}$$

$$\rho^* = \frac{\rho}{R}\left(1-\frac{\Delta}{s_p}\right) \tag{4.3}$$

This expression (referred to as the Blurred Shadow Model) was derived by Bongiovanni et al. (1997) and has been transcribed here to facilitate discussion. Equation 4.1 was obtained by calculating the convolution product of the focused image pattern $(1 - I_{R_\Delta})$ by the cylinder function I_{R_p} where R_p is given by:

$$R_p = r_p \left|\frac{\Delta}{s_p}\right| \frac{1}{1 - \Delta/s_p} \tag{4.4}$$

and I_{R_Δ} is defined by:

$$I_{R_\Delta}(\rho) = 1 \text{ for } \rho \leq R_\Delta \quad \text{and} \quad I_{R_\Delta}(\rho) = 0 \text{ elsewhere} \tag{4.5}$$

where, $$R_\Delta = \frac{R}{1 - \Delta/s_p} \tag{4.6}$$

The Blurred Shadow Model (BSM) assumes a linear shift-invariant optical system with negligible diffraction and no aberrations.

As deduced from Equation 4.1, the BSM offers the possibility of "recovering" the actual size of the object and its position by knowing the characteristics of a blurred image (i.e., the irradiance profile). However, due to the absolute value in Equation 4.2, the irradiance profile itself is not sufficient to reveal the sign of Δ. Although Bongiovanni et al. explored various alternatives to infer the sign of Δ (e.g., contrast level, diameter of the central bright spot, central irradiance, etc.), it was concluded that these criteria were not sufficiently robust. In most practical applications, the sign of Δ is not readily defined because the motion of a bubble above 1 – 2 mm diameter is not rectilinear but oscillatory and the motion depends on the bubble size. One alternative is to derive a non-exact correction procedure (i.e., provide a correction within a given range of accuracy). However, in the system under consideration (Figure 4.1), Δ is invariably negative and nearly constant in spite of bubble size, therefore, the approach suggested by Bongiovanni et al. could be implemented deterministically, which is described as follows.

4.2.2 Correction procedure due to optics

The BSM is applicable for images in which the position and boundary correspond to those of an opaque sphere and should not be used directly for the case of bubbles in water, i.e., a transformation is required (Bongiovanni et al., 1997). The bubble irradiance pattern is the sum of the contributions of direct, reflected and refracted rays. Their impact on image formation is governed by geometric optics and photometric laws (i.e., Snell's laws and Fresnel's formulae). It has been demonstrated (e.g., Leifer et al., 2003) that ignoring the effects of reflected rays may cause large sizing biases (ca. 15%).

The characteristics of the light source (r_L and s_L) have a major influence on the contribution of reflected rays. The approach consists in transforming the bubble image into an equivalent opaque object using Equation 4.7 which is expressed in terms of the angle θ_L below which the bubble sees the source plane:

$$D_{S1/2}/D_{b1/2} = 1 - 7 \times 10^{-5}\,\theta_L + 4 \times 10^{-5}\,\theta_L^2 \qquad (4.7)$$

where $D_{b1/2}$ is the measured diameter when thresholding the bubble at half the irradiance level, $D_{S1/2}$ is the diameter of the equivalent opaque sphere and θ_L (in degrees) is defined by:

$$\theta_L = \tan^{-1}\left(\frac{r_L}{s_L + \Delta}\right) \tag{4.8}$$

Equation 4.7 is the best-fit correlation obtained from the numerical simulation of the Ray Tracing Model (Bongiovanni et al., 1997). Equation 4.7 also implies that reflected rays cause underestimation of the measured size, even for an in-focus image (i.e., $\Delta = 0$).

After this transformation, the BSM can be readily used to determine the size and position of a bubble. It is convenient to define two parameters: $B_{1/2}$, which is the sizing bias when thresholding the image at half the irradiance level, given by:

$$B_{1/2} = \frac{D_{b1/2} - D_b}{D_b} \tag{4.9}$$

and, $P_{1/2}$, the grey level gradient on the contour at the same half irradiance level.[1]

With these definitions and for specific case of $\Delta < 0$ (i.e., when $B_{1/2} < 0$ and, consequently, $D_{b1/2} < D_b$), the BSM can be conveniently represented graphically as

[1] Note, any irradiance level could be chosen; this is the one suggested by Bongiovanni et al. (1997) and it is a "common sense" choice

contours of $B_{1/2}$ (Figure 4.2) as a function of two quantifiable image and optical parameters, $P_{1/2}$ and r_P. (An example of the use of the BSM is given in Appendix I.)

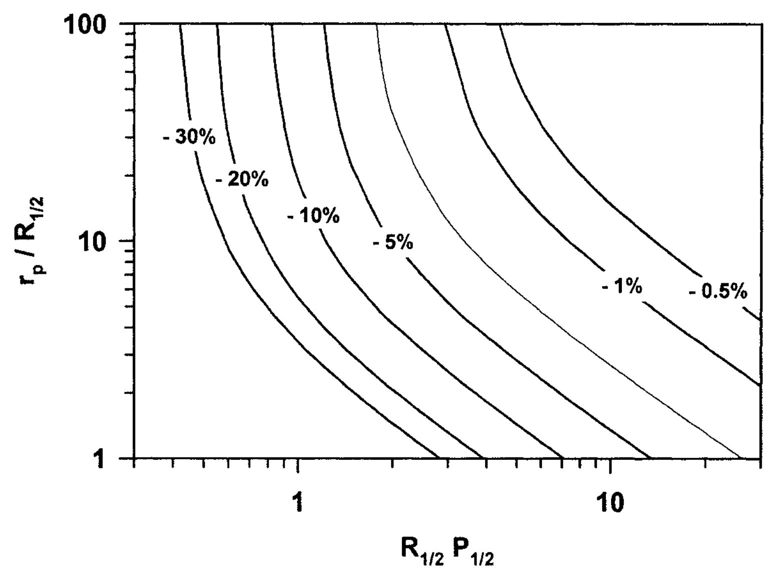

Figure 4.2. The BSM: contours of $B_{1/2}$ for the case of negative defocus (Note that $R_{1/2} = \frac{1}{2}D_{b1/2}$)

4.2.3 Effect of the inclined window

Studies in which an inclined window was used for sizing bubbles through backlit incoherent imaging are not common in the literature. However, there are some studies that can be used to anticipate the effect of θ_W. Qiu and Dhir (2002) observed that, at high inclination angles, bubbles changed shape from spherical to elongated spheroid or crescent as they slid on the surface of a polished surface. They also found that, the larger the inclination angle, the more distorted was the bubble. Addlesee and Kew (2002) observed significant flattening, particularly at $\theta_W > 45°$. They also discussed the difficulties associated in defining the resulting 3-D geometry. In their study, the bubble was modelled as a hemisphere because it is the simplest one-parameter shape with a flattened side.

It has been observed for the case of a single bubble, that $\theta_W > 5°$ is sufficient to keep the bubble in contact with the window (recall that the motion of a bubble above 1–2 mm is not rectilinear but oscillatory). However, $\theta_W > 15°$ is required for the case of bubble swarms (particularly when the population of size classes is broad) because the (liquid) turbulence caused by the swarm displaces bubbles (specially the smaller ones) away from the window. The discussion above indicates that at 15° bubble distortion may be significant; therefore, should a correction be judged necessary, we would expect to empirically determine a relationship between D_b (defined by Equation 3.2) and θ_W, i.e., $D_{max} = f(\theta_W)$ and $D_{min} = f(\theta_W)$.

4.3 Experimental

Applying a sufficiently low constant airflow rate to an orifice submerged in water produces bubbles of equal size at uniform departing periods (defined as the time interval between the release of consecutive bubbles). This bubble formation pattern is often referred to as the single bubbling regime (Zhang and Shoji, 2001). In the present work, a low constant pressure was maintained in an airtight reservoir using a water column to control the airflow. This approach was similar to the ones presented by Minnaert (1933) and by Vigneault et al. (1992). The bubbles were sized both with the displaced-volume method (regarded as the standard) and from digitized images collected as they rose along the window of a variable-angle viewing chamber. The experiments were designed to assess the correlation between real and imaged sizes, and to evaluate the effects of θ_L (i.e., reflective rays) and θ_W (i.e., bubble deformation).

4.3.1 Generation of standardized bubbles

A capillary tube was placed in the airtight chamber (A), as illustrated in Figure 4.3. Chamber (A) was attached to the generation cell (B) which was made of clear PVC tubing (150 mm long and 25.4 mm I.D.). The air supply (flexible) tube (C) was connected to chamber (A) and pressurized by opening valve (D) located at the bottom of the water column (E). A dilute solution (50 mg of solute per kg of solution) of a commercially available surfactant (Dow Froth 250C) in distilled water was added into the generation cell (B). This sequence was used to prevent water entering the capillary and blocking the air supply tube. The top end of the generation cell (B) was machined to facilitate insertion into an o-ring joint located in the rotating ball (F). This (plastic) ball was attached to the bottom of the viewing chamber (G) by a dual sealing-rotating mechanism. The viewing chamber (G) was rotated 5° (measured from a plane parallel to the direction of gravity) and the rotating ball (F) adjusted to keep the generation cell (B) vertical. This angle ($\theta_W = 5°$) kept the rising (single) bubbles in contact with the window surface as they passed through the field of view of the camera (H). The viewing chamber (G) was filled with the surfactant (frother) solution up to a constant point (ca. 11 cm between the optical axis and the liquid level) to maintain a constant pressure head. The height (ΔH) was then adjusted to achieve low bubble departing periods, typically between ½ and 1 s.

4.3.2 Sizing of standardized bubbles

The (glass) deflector (I) was turned into the "imaging position" (i.e., it was rotated to direct the bubbles towards the window). Once the generation pattern was stable, the bubble departing period was recorded and the image capture routine launched. It should be noted that the pressure in the airtight reservoir (J) was quasi-static, i.e., it decreased slightly with time as the air was depleted due to the change in ΔH (as noted by Vigneault et al., 1992). However, the influence of this pressure (head) variation on the generation frequency was considered insignificant. During a sizing experiment (ca. 15 min), ΔH changed less than 2 mm and the bubble departing period increased less than 1%. Room temperature was constant (20 ± 1 °C).

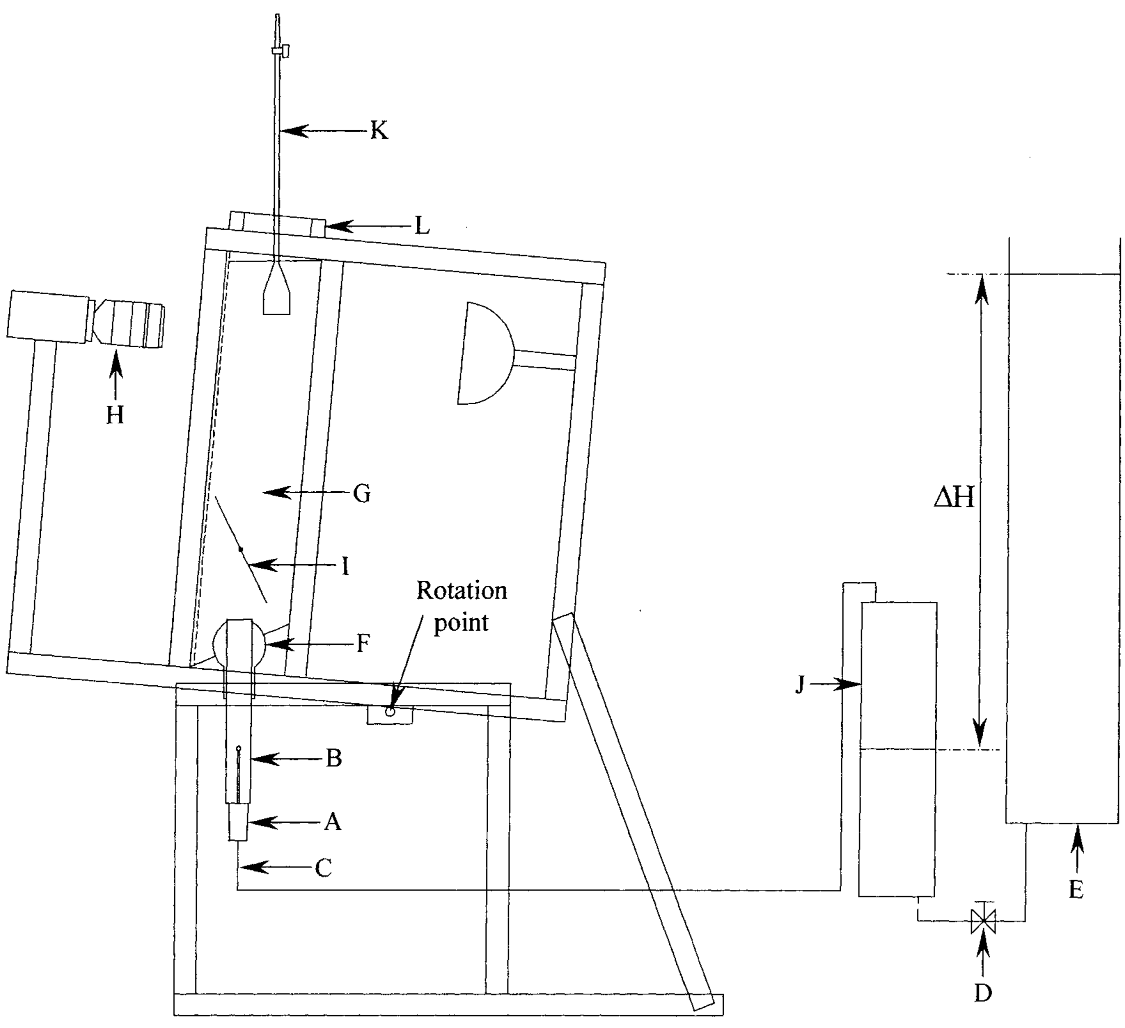

Figure 4.3. Experimental setup (description of the components in the text)

4.3.2.1 Imaging

A 50 mm Nikon Nikor lens equipped with an extension tube was attached to a Qimaging – Retiga 1300 progressive scan digital camera. An automated system, comprising a motorized optical bench and an image analyzer, was used to determine the size and position of the entrance pupil. (Appendix II includes the procedure to determine the entrance pupil characteristics.) The shutter speed was set to 15 ms and the aperture stop of the lens to f/5.6. This camera has an IEEE 1394 interface that allows the direct transfer of full resolution images (1000 x 1300 pixels and 256 grey levels) onto the hard disk of a portable computer without using a frame grabber. The maximum frame rate was ca. 2 frames/s, consequently not all frames contained a bubble. Typically, between 30 and 40 bubbles were collected in 300 s (i.e., 30 – 40 frames out of 600 contained a complete bubble).

A circular mask with r_L = 15 mm, was placed at s_L = 135 mm. Two light diffusers were attached to the mask. The light source (a 600 W quartz lamp) was connected to a rheostat to adjust the light intensity. The output of the rheostat (100V) was selected to give the image background a grey scale value of 256 (i.e., white). The images were thresholded at half the grey scale. A commercial image software package (Northern Eclipse 6.0) was used to determine D_{max} and D_{min}.

To determine $P_{1/2}$, a linear fit was applied to the grey scale gradient (across the major and minor axes of the image) for 10 randomly selected bubbles. The average of the 40 intensity gradients (i.e., 10 bubbles x 4 bubble edges) was considered as the characteristic $P_{1/2}$ of the bubble.

4.3.2.2 The displaced-volume method

Once the images were collected, the deflector (I) was turned to the "burette position", i.e., it was rotated to direct the bubbles towards the funnelled burette (K) (the burette was filled with the same surfactant solution and immersed into the viewing chamber through the opening (L) prior to starting to collect the images). A sufficient number of bubbles was allowed to enter the burette to measure reliably the displaced volume (i.e., at least 20% of the total burette volume), typically between 500 and 1000. The burette was removed from the bubble stream. Before recording the final volume mark, a period of ca. 5 min elapsed to permit the solution to drain from the burette walls. The total number of bubbles that entered the burette was recorded. It is understood that individual bubble volumes should not be calculated directly from the total volume displaced and the number of bubbles due to the different pressure conditions between the point where the image was capture and the burette. Also, the fact that some air was in the burette at the beginning of the test has to be considered. The correction procedure is described in the following section.

4.3.2.3 Corrections

The measurements obtained with the imaging and displaced-volume methods were taken under different conditions, therefore, corrections have to be made. Sizes obtained with the imaging method can be corrected with Equation 4.10 to standard pressure (P^0 = 1 atm) by assuming spherical bubbles and ideal gas behaviour:

$$D_b = D_b'\sqrt[3]{\frac{P}{P^0}} \tag{4.10}$$

where, D_b' is the uncorrected diameter

$P^0 = 101.325$ kPa

P = is the (hydrostatic) pressure where the optical axis intersects the window

The pressure P was calculated by measuring the distance between the optical axis and the liquid level using a tabulated value of the water density at 20°C (Perry and Green, 1997). The atmospheric pressure during all tests was assumed constant (101.325 kPa). Taking the bubble aspect ratio (D_{min}/D_{max}) to be invariant, a correction for the equivalent spherical bubble diameter can be derived by substituting Equations 4.11 and 4.12 in Equation 3.2:

$$D_{\max} = D'_{\max} \sqrt[3]{\frac{P}{P^0}} \tag{4.11}$$

$$D_{\min} = D'_{\min} \sqrt[3]{\frac{P}{P^0}} \tag{4.12}$$

where, D'_{max} and D'_{min} are the uncorrected maximum and minimum diameters, respectively.

In the case of the volume-displaced method, Equation 4.13 gives the equivalent spherical bubble diameter at P^0 and 20°C:

$$D_b = \sqrt[3]{\frac{6\Delta nRT}{N\,P^0\pi}} \tag{4.13}$$

where, Δn is the number of accumulated moles of air

N is the number of collected bubbles

R is the universal gas constant

T = 293.15 K

The ideal gas law along with the burette dimensions and the density of water at 20°C were used to calculate Δn. The marks on the burette were previously calibrated with an analytical balance using distilled water.

Nine bubble size classes were generated with capillaries of different sizes (Table 4.1). The inner diameters of the capillaries were measured with an optical microscope.

Table 4.1. Classification of the capillary tubes

Capillary Tag	Nominal size (μm)	Measured size (μm)
C1	25[1]	20
C2	25	20
C3	102[2]	38
C4	76	68
C5	102	99
C6	178	187
C7	406	393
C8	508	507
C9	1800	1680

[1] Same size as C2 but it was positioned horizontally to produce smaller bubbles.
[2] Originally, this capillary had the same size as C5 but it underwent a heating-stretching-cutting procedure to reduce its size.

For each bubble size class, a total of five imaging and displaced–volume sizing tests were conducted from which an average value and standard deviation were calculated.

4.3.3 Effect of θ_L

To evaluate the effect of non-direct rays, i.e., the effect of θ_L, masks of various r_L were used. Three capillary tubes were employed (C1, C6, C9). The r_L were 10, 15, 20, 40, 60 and 80 mm to give $\theta_L = 4.2°, 6.3°, 8.4°, 16.5°, 24.0°$ and $30.7°$.

4.3.4 Effect of θ_W

To evaluate the effect of θ_W, the cell (B) was replaced by a 25.4 mm I.D. plastic tube (machined to fit the o-ring joint) and placed to intercept the stream of single bubbles. The bubbles were generated at the bottom of a 50 mm I.D. clear-plastic column which was open to the atmosphere. Figure 4.4 illustrates the set-up. A rubber plug was placed in the plastic tube to permit filling the viewing chamber, which was sealed with a threaded cap positioned on the opening (L). The plug was removed and the bubbles entered. Five capillary tubes were employed (C2, C4, C6, C7, C8). Images were collected at $\theta_W = 5°$, 15°, 30°, 45° and 60°. The D_{max} and D_{min} obtained were corrected using equations 4.11 and 4.12. The pressure P (where the optical axis intersects the window) was $< P^0$ and varied with θ_W, as illustrated in Figure 4.4. Trigonometric and hydrostatic equilibrium formulae were used to calculate P.

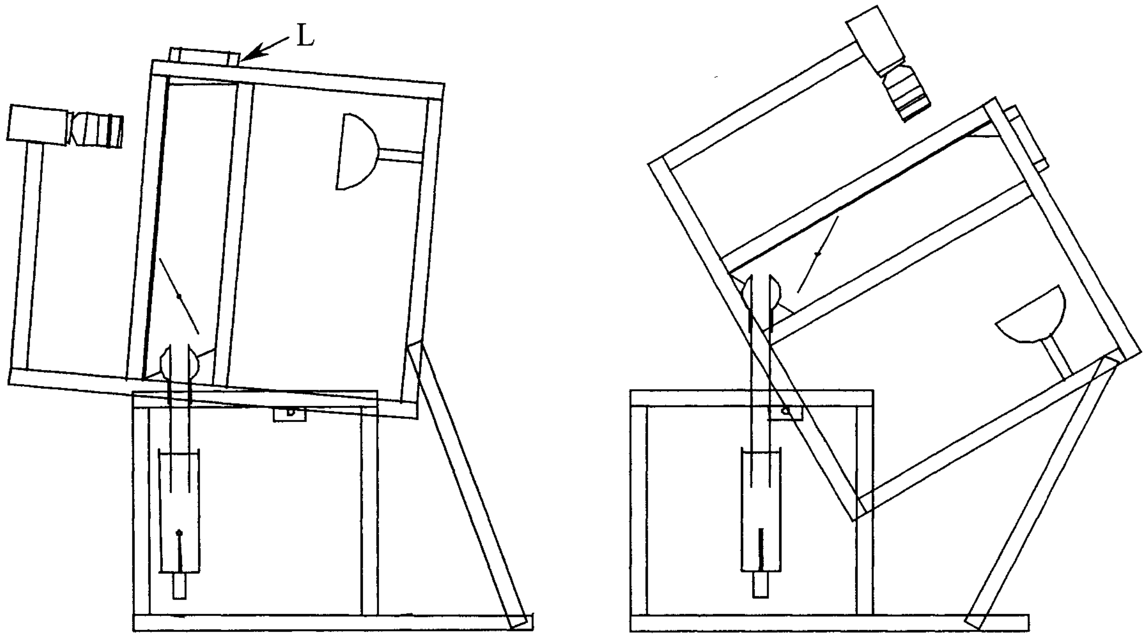

Figure 4.4. Experimental set-up to evaluate the effect of θ_W
Left: $\theta_W = 5°$; Right: $\theta_W = 60°$

4.4 Results and Discussion

4.4.1 Sizing underestimation

As depicted in Figure 4.5, at $\theta_W = 5°$ and thresholding at half the intensity level, the imaging method systematically underestimates and the bias is correlated to bubble size, i.e., the larger the bubble, the larger the bias. (Appendix III includes the results in tabular format.)

Figure 4.6 shows raw pixel data near the image boundary for three bubble size classes and an opaque disk located at the focus plane. Included is the normalized irradiance profile along the bubble axis (pixel position 7). The disk has a negligible thickness (ca. 0.02 mm), therefore, it is reasonable to assume that $\Delta = 0$. Despite this and regardless how precise the detection of the focus plane is, the profile is not a step function in intensity. This suggests a procedure to locate the focus plane, i.e., when the intensity gradient is maximum.

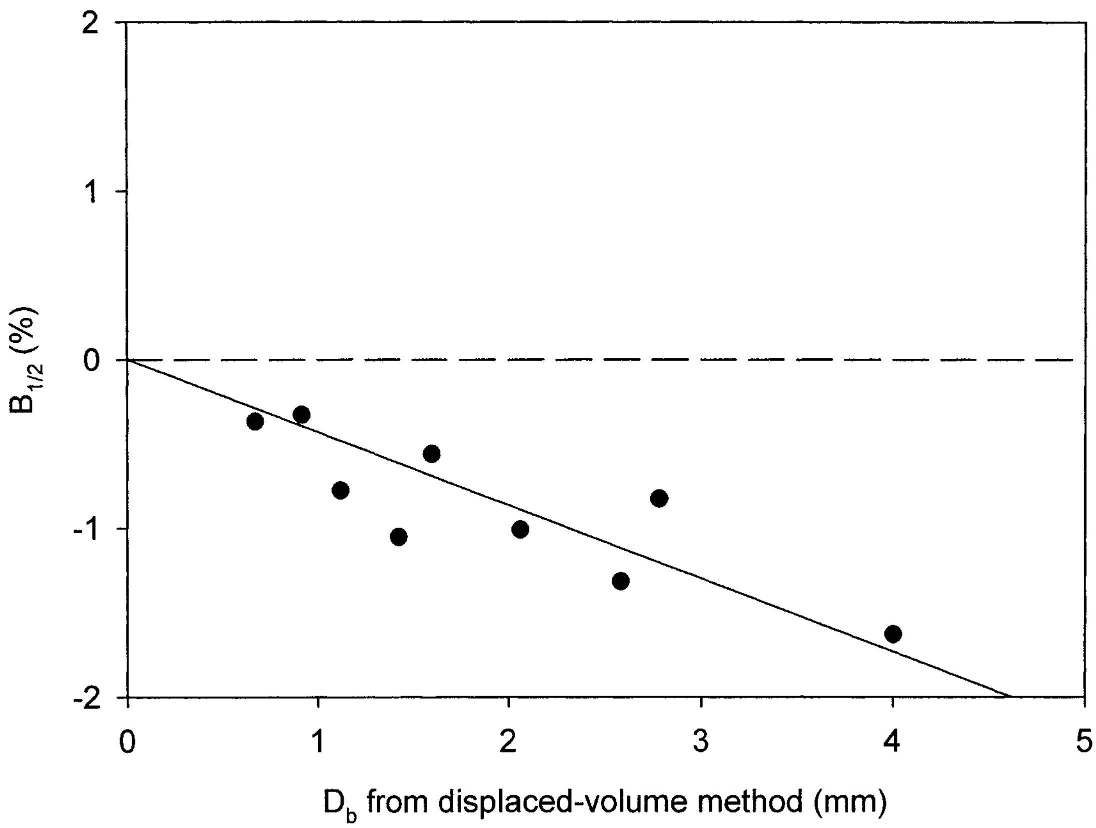

Figure 4.5. Imaging sizing bias ($\theta_W = 5°$; threshold = ½ intensity; $\theta_L = 6.3°$)

In the case of bubbles, as size increases the gradient decreases (i.e., the blurring increases) because Δ becomes gradually more negative. In this system, bubble blurring varies consistently with size since the motion has been limited to two-dimensions. Since the pixel size is ca. 0.01 mm and the measured $B_{1/2}$ values for C1 and C9 are ca. – 0.4 and – 1.6 %, respectively (Figure 4.5), it is deduced that the real bubble edge is within the plausible threshold range, i.e., it is located between the background intensity and half the threshold. This seems at odds with Leifer et al. (2003) who observed that the real threshold is slightly below the background intensity. They suggested that thresholding at multiple intensities and using a curve fit to extrapolate to the appropriate size will produce the greatest accuracy. However, the results here are not inconsistent with Leifer et al.'s observations; the data in Figure 4.5 are taken at a small θ_L (6.3°), i.e., reflected rays do not impact the image significantly. As discussed in more detail in the following section, reflected rays may cause a significant underestimation.

In addition to the role of reflected rays, Leifer et al.'s images appear to be more blurred, which increases the threshold uncertainty. For example, Figure 3 in their paper illustrates the sizing variation with threshold for a ca. 1.4 mm bubble. The measured size varies ca. 8% with a threshold change of 9%, whereas in the case of size class C6 (Figure 4.6 here), the size varies ca. 1% with a 50% threshold variation.

4.4.2 Effect of θ_L

Figure 4.7 illustrates that as θ_L increases the measured size decreases. Also, the size of the central spot increases with θ_L due to the increasing contribution of reflected rays. Conceptually, the image of a bubble unaffected by reflected rays (as in the case of an opaque object) would be obtained with an infinitely small θ_L. The size obtained under this condition (referred to as $D_{S1/2}$) may be obtained by extrapolation. A second-degree polynomial regression has been included in the figure. The fitting is good for bubbles C1 and C6, however, there is more scattering with C9. This is due to the shape variations associated with larger bubbles.

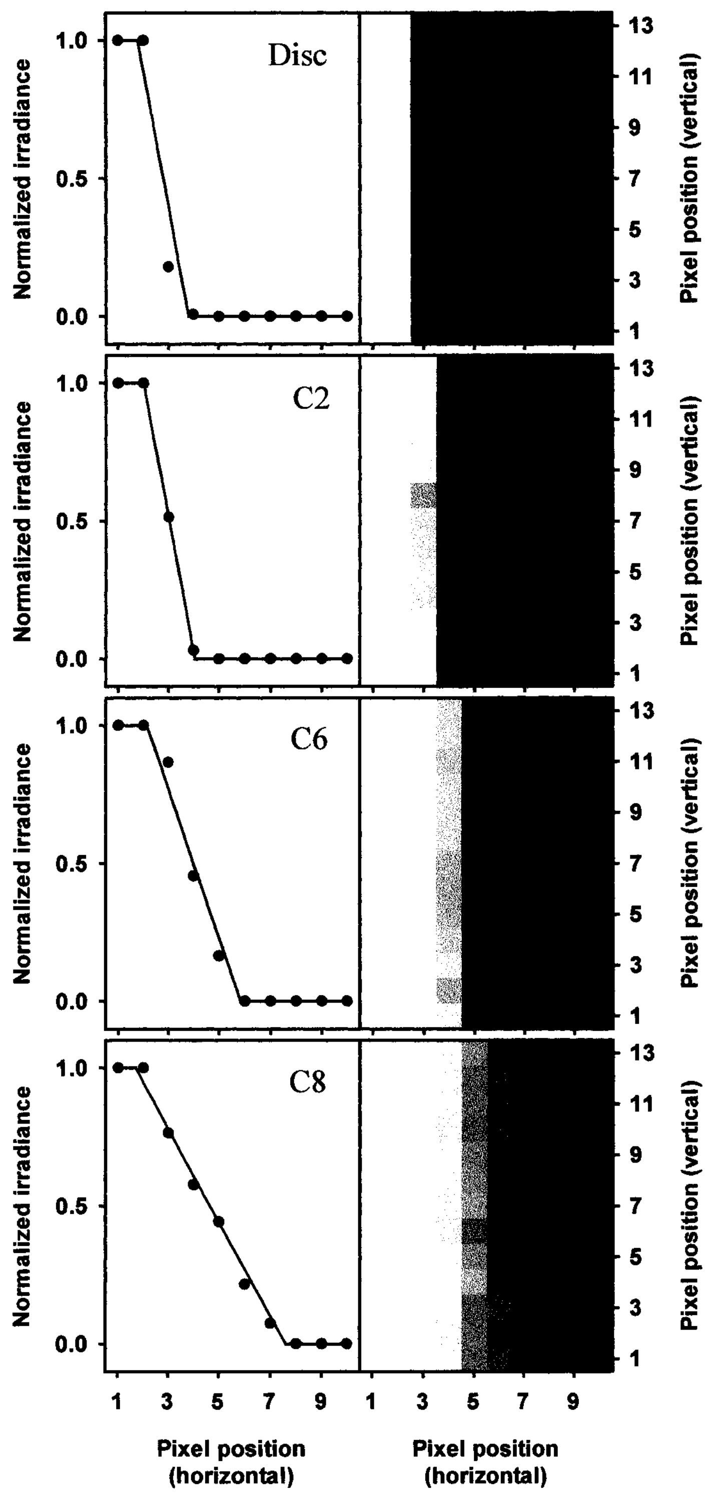

Figure 4.6. Intensity profile near the image boundary (actual pixel size ca. 0.01 mm)

In Figure 4.7, the symbols (triangles) on the vertical axis represent the sizes obtained with the displaced-volume (reference) method. In the case of C1, $D_{S1/2}$ (the polynomial's independent term) virtually corresponds to the reference value. It was anticipated that the impact of Δ and θ_W for this small bubble (ca. 675 μm) under these conditions would not be significant; and, therefore, the reference would be close to $D_{S1/2}$.

The computed $D_{S1/2}$ values were used to express the results in terms of the ratio $D_{S1/2}/D_{b1/2}$, as shown in Figure 4.8. Although Equation 4.7 was derived assuming spherical bubbles, the agreement between the predicted and the experimental data is good, even for C9. In this case, direct rays are the prime determinant of the image edge, confirming the hypothesis of Bongiovanni et al. (1997). They also discussed that the characteristics of the irradiance profile close to the image edge (i.e., $P_{1/2}$) would not be affected by θ_L when Δ is small, which proved to be the case here (Figure 4.9).

It is worth noting that the underestimation could be dramatic (Figure 4.8): for $\theta_L = 60°$ it is ca. 15% and for a light source of infinite size (i.e., $\theta_L = 90°$) it is ca. 30%.

4.3.3 Effect of θ_W

Examples of images at various θ_W are given in Figure 4.10. The deformation caused by the gravity force increases the apparent size due to bubble "flattening". Moreover, it can be seen that the blurring decreases as θ_W increases corresponding to the bubble flattening and decreasing Δ. An interesting observation is the fact that at 60° the bubbles are quasi–circles. This observation along with the sensitivity of the optical system to perceive grey levels (i.e., it is evident that at 60° the blurring almost vanishes) is such that it is possible to confirm qualitatively the hypothesis of Addlesee and Kew

(2002). They modelled (for high inclinations) the bubble as a hemisphere because it was considered the simplest one-parameter geometry with a flattened side. In the present case, attempts were made to predict the three-dimensional geometry for any angle between 5° and 60° and therefore derive the appropriate formulae to compute an equivalent spherical diameter (D_b); however, it was concluded that the information was not sufficient to quantify the relationship between θ_W and the resulting 3-D shape.

Consequently, an empirical approach was adopted which consisted in using a (consistent) definition of equivalent spherical diameter (Equation 3.2) and quantifying the variation of D_{max} and D_{min} in terms of θ_W (Figure 4.11). The information was then condensed into an empirical model (Equation 4.14) that permits computation of a theoretical "non-deformed" value (referred to as D_b^0 and obtained by extrapolation, i.e., D_{max} and D_{min} as $\theta_W \rightarrow 0$) for any D_b and θ_W. A third-order polynomial was used for the extrapolation since this gave a high coefficient of determination ($r^2 > 0.99$). It should be noted (Figure 4.11) that θ_W impacts D_{min} more significantly than D_{max}.

$$\frac{D_b^{\,0}}{D_b} = 1 - C_1\theta_W + C_2\theta_W^{\,2} - C_3\theta_W^{\,3} \tag{4.14}$$

where, $C_n = a_n + b_n\left[1 - \exp(-c_n * D_b)\right]^{d_n}$ (4.15)

θ_W is in degrees

D_b is in μm

and, a, b, c, d are empirical parameters given in Table 4.2

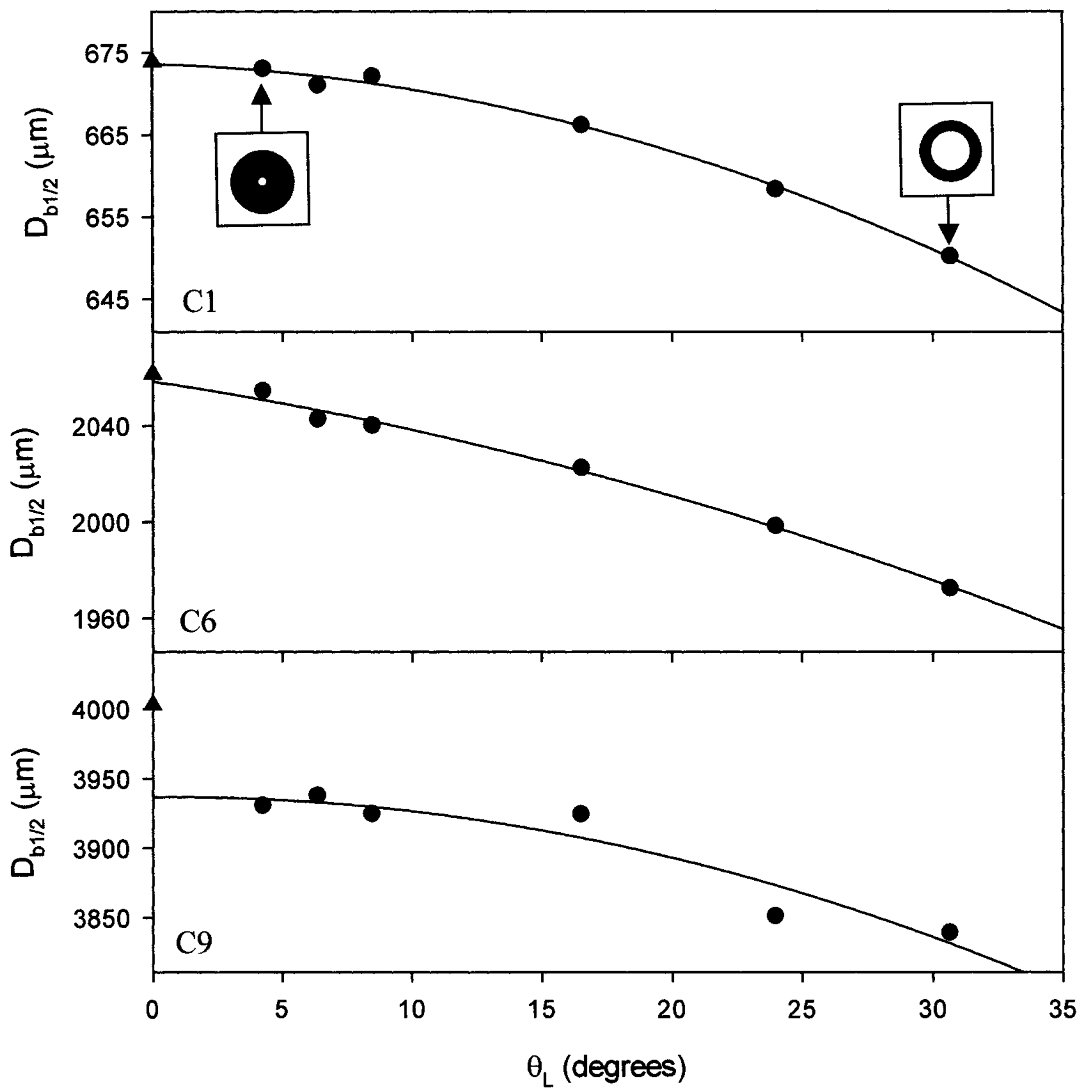

Figure 4.7. The effect of θ_L: the impact of reflected rays

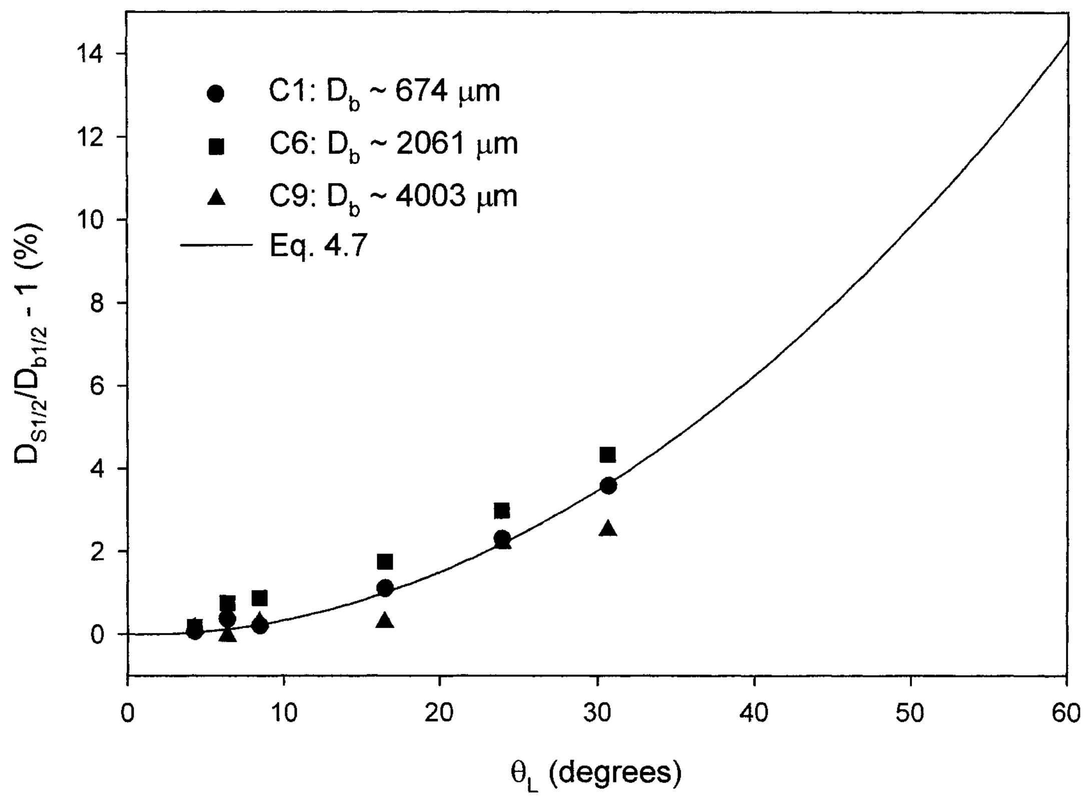

Figure 4.8. Experimental vs. predicted underestimation due to θ_L

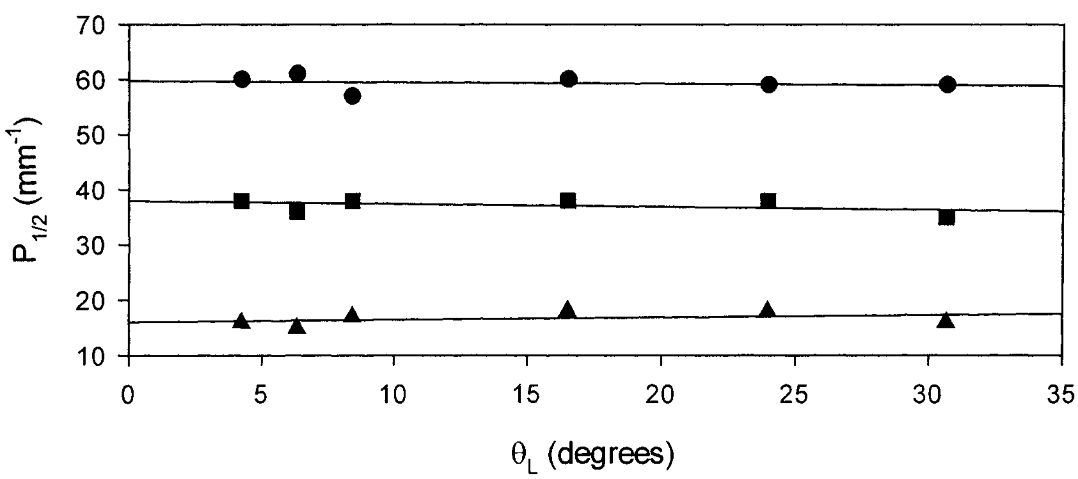

Figure 4.9. Invariability of the edge profile with θ_L (symbols as in Figure 4.8)

For the sake of consistency, the measured D_{max} and D_{min} were corrected both for pressure and defocus distance, despite the fact that Δ may not be associated to a spherical or ellipsoidal geometry. (Note that, since the deviation due to Δ has been compensated, the subscript "½" has been removed from $D_{b1/2}$.) Regardless, at shallow angles the bubble retains its elliptic shape (15° has proven sufficient to keep bubble swarms in contact with the window). Blurring quantification is given in Figure 4.12 and pressure corrections are discussed in section 4.3.4.

Although Equation 4.14 was developed and tested experimentally against bubbles between ca. 0.9 and 3 mm in diameter, the model parameterization (Equation 4.15) was selected carefully to provide a robust (safe) applicability beyond this range, i.e., $C_n \rightarrow a_n + b_n$ as $D_b \rightarrow \infty$ and $C_n \rightarrow a_n$ as $D_b \rightarrow 0$. Figure 4.13 illustrates the comparison between experimental and predicted values.

4.4.4 Defocus bias

The data in Figure 4.5 were collected under conditions where the underestimation and overestimation caused by θ_L (6.3°) and θ_W (5°), respectively, are relatively insignificant (in both cases, the bias is less than 1%). Considering the current pixel resolution (0.01 mm), it is reasonable, as a first approximation, to assume the two effects counterbalance. Therefore, the (negative) bias in Figure 4.5 is mainly due to the defocus distance Δ.

Figure 4.14 illustrates the measured $P_{1/2}$ values for the nine bubble size classes, and the predicted $B_{1/2}$ from the BSM. The predicted $B_{1/2}$ does not fully agree with the observed.

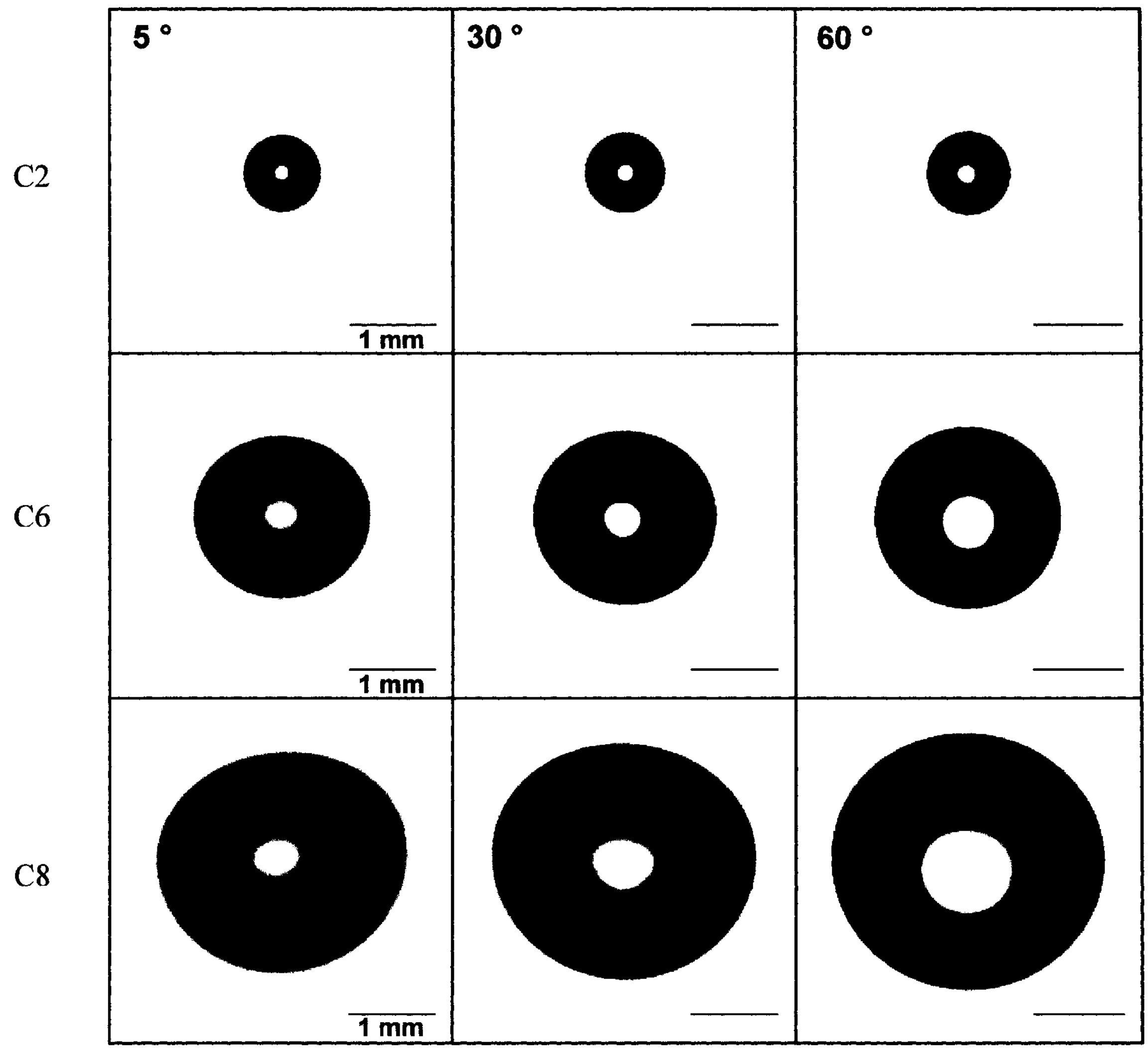

Figure 4.10. The effect of θ_W: examples of images

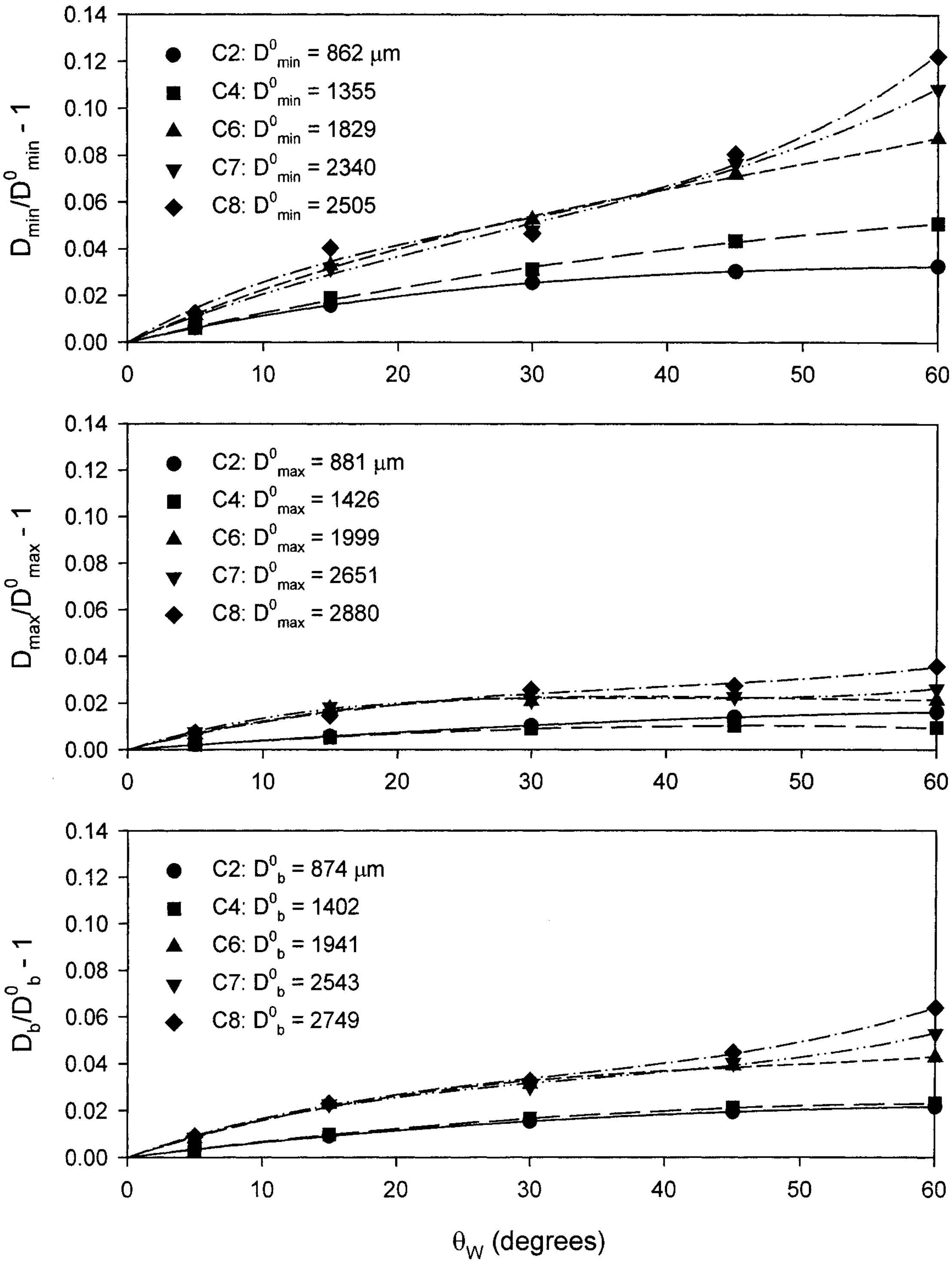

Figure 4.11. The quantification of bubble deformation: the impact of θ_W

Table 4.2. Parameter definition of Equation 4.15

n	*a*	*b*	*c*	*d*
1	6.998×10^{-4}	1.296×10^{-3}	6.384×10^{-3}	2.770×10^{4}
2	6.604×10^{-6}	3.845×10^{-5}	4.448×10^{-3}	2.023×10^{3}
3	7.304×10^{-9}	5.398×10^{-7}	2.108×10^{-3}	5.486×10^{1}

(*a* and *b* are in degrees^{-n}, c is in μm^{-n}, and *d* is dimensionless)

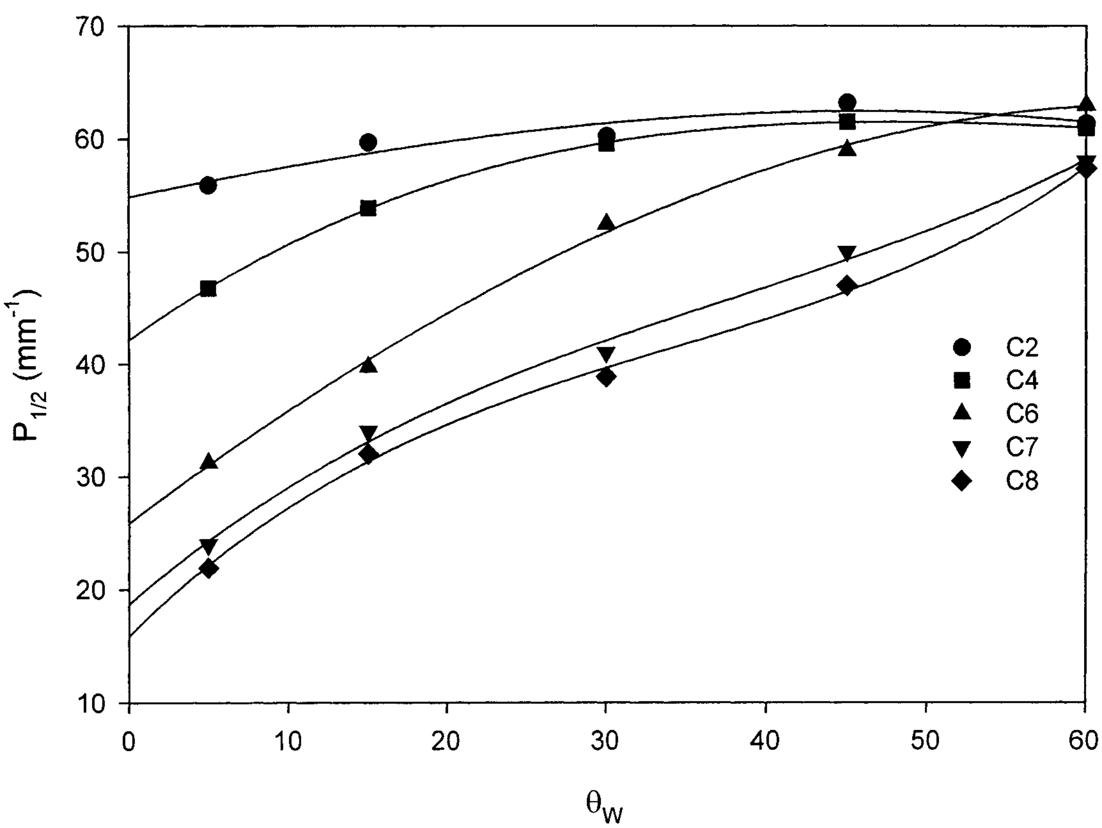

Figure 4.12. Decrease of blurring (i.e., increase in $P_{1/2}$) due to bubble flattening as θ_W increases

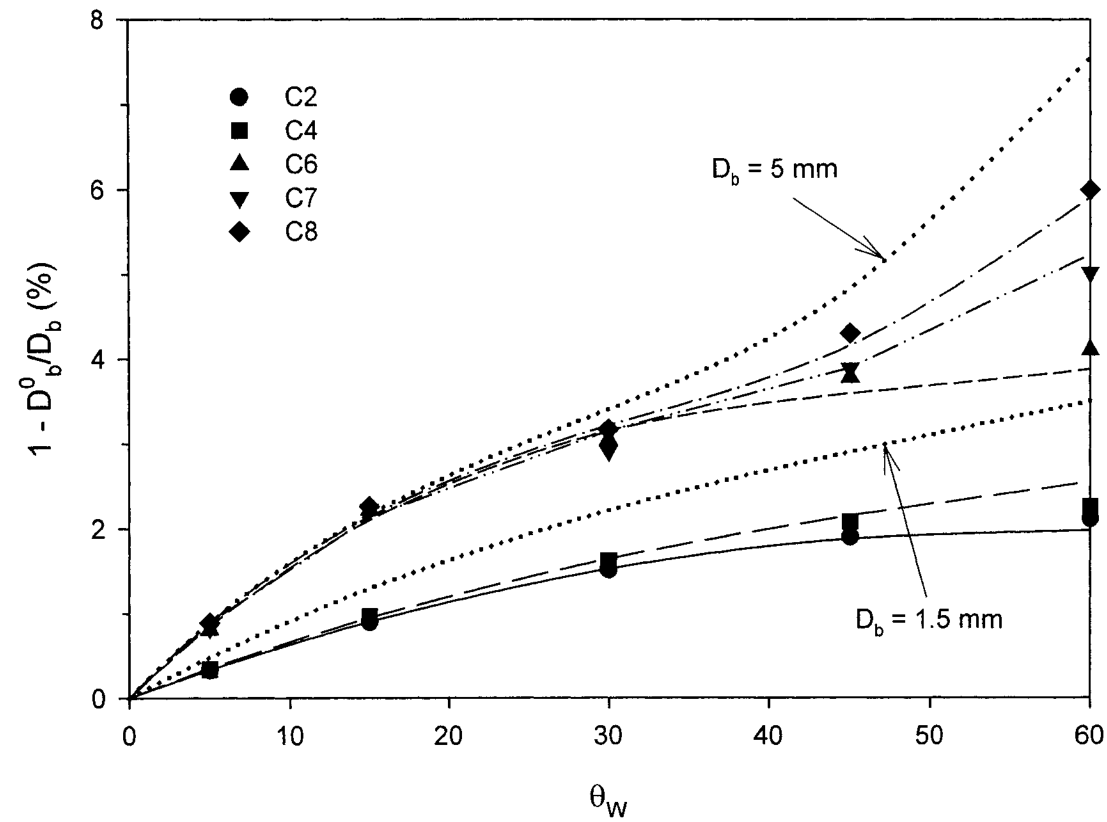

Figure 4.13. Experimental vs. predicted deformation using Equation 4.14 (the dotted lines represent predictions for D_b = 1.5 and D_b = 5.0 mm)

The BSM was primarily derived to predict Δ and $B_{1/2}$ from the image characteristics. However, in the system here (Figure 4.1) Δ might be considered as independent variable since it is reasonable to assume that $|2\Delta| \approx D_b$ as long as the thickness of the liquid film between the bubble and the window is neglegible (Addlesee and Kew (2002) deduced that this thickness is in the order of 50 – 100 μm). Nevertheless, as indicated in Figure 4.15, this correlation is approached when bubbles are < 1 mm and deviates as size increases.

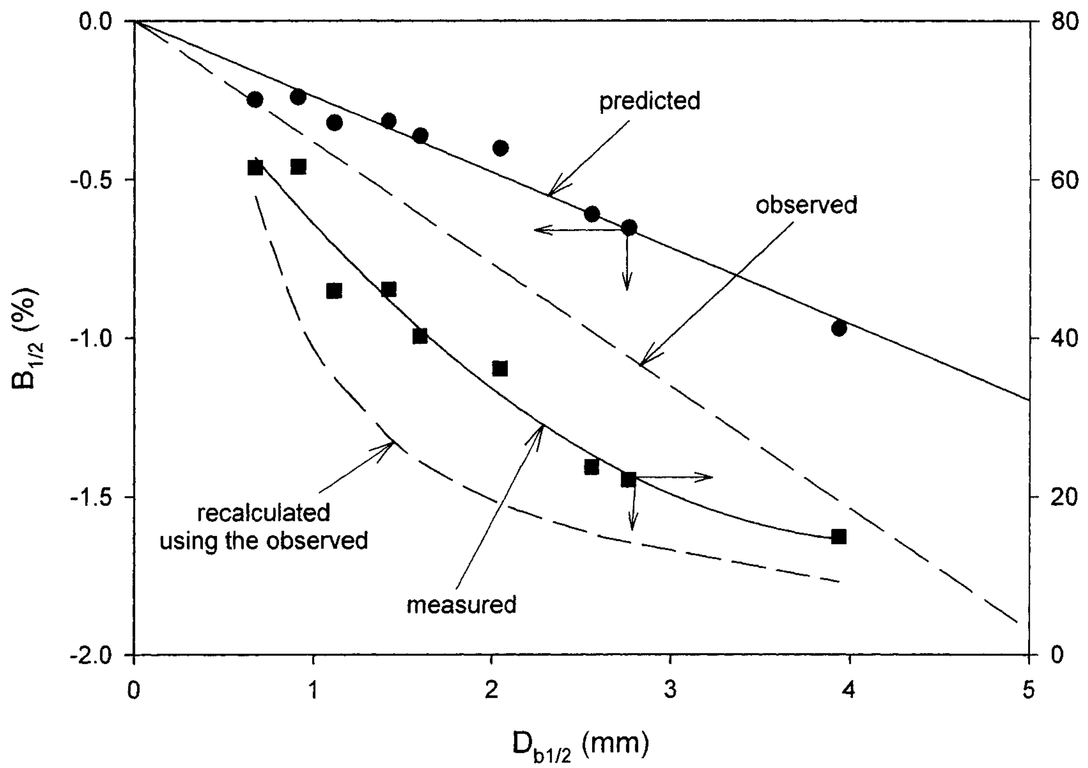

Figure 4.14. Predicted (symbols) vs. observed $B_{1/2}$.

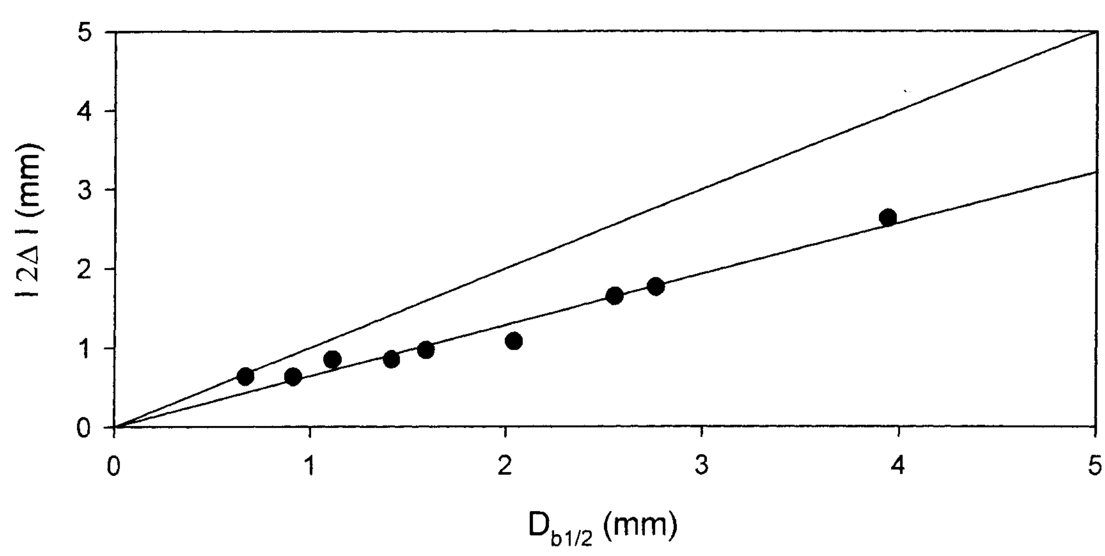

Figure 4.15. The deviation of the BSM

Various factors may explain this. The BSM assumes spherical bubbles, negligible diffraction, no aberrations, and a linear-shift invariant optical system. Bubbles > 1 mm start to lose their spherical shape and become ellipsoids. One alternative is to recalculate $B_{1/2}$ but using the "observed" Δ (i.e., assuming that $|\Delta| = \frac{1}{2}D_{b1/2}$) obtained from Figure 4.15. In Figure 4.16, the correction has been applied. It is shown that the original data are transformed to have less bias.

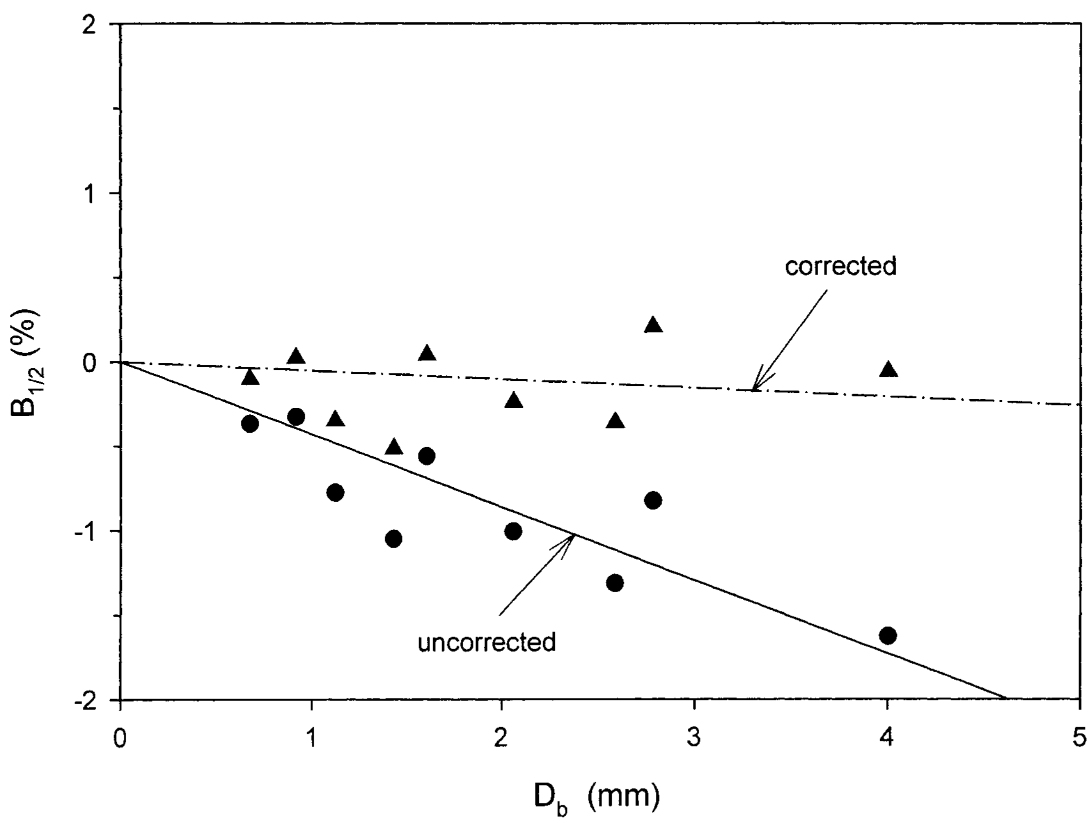

Figure 4.16. Corrected bias using the "observed" Δ from Figure 4.15 (D_b obtained from the displaced-volume method)

4.4.5 Correction protocol

The data treated in this chapter were collected at optical conditions which are not generally practical. To capture a significant number of bubbles of different sizes in a single frame, the θ_L and θ_W would have to increase to a point where the two effects do not cancel and the bias becomes significant. Therefore, a correction protocol should be devised. The following is now being implemented.

First, the image is thresholded at half the irradiance level to obtain $D_{b1/2}$ and $P_{1/2}$. Second, $D_{b1/2}$ is corrected to standard pressure using Equation 4.10. Third, the image is transformed to the equivalent opaque sphere ($D_{S1/2}$) using Equation 4.7. Fourth, Δ and $B_{1/2}$ are calculated using $P_{1/2}$ and the BSM. (Whenever possible, the optical system has to be calibrated with standardized single bubbles, to correct model deviations as indicated in Section 4.4.4 and Figure 4.15.) Fifth, the correction due to θ_W is made with Equation 4.15.

4.5 Conclusions

It was observed that when thresholding at half the intensity level, sizes were systematically underestimated and the bias was correlated to bubble size, increasing from 0.3% at ca. 0.7 mm to 2% at ca. 4 mm. Experiments were designed to evaluate the biases due to system optics (i.e., the contribution of reflected/refracted rays and the defocus distance to image formation) and due to the sloped window. The results showed that reflected/refracted rays slightly biased towards underestimated sizes whereas the inclined window caused a small overestimation, due to the bubble flattening caused by gravity. These two effects were of similar magnitude and, therefore, tended to cancel.

Consequently, the underestimation trend was attributed to the defocus distance which, in this unique system, is small and unambiguous (i.e., it is invariably negative since bubbles flow "behind" the focus plane, the underside of the window). A semi-empirical correction procedure is suggested which uses the fundamental method of Bongiovanni et al. (1997) to correct the bias due to system optics along with an empirical approach to compensate for bubble flattening.

CHAPTER 5

VERIFICATION OF THE SAMPLING AND IMAGE ANALYSIS PROCEDURES USING BI-MODAL DISTRIBUTIONS

5.1 Introduction

Reviewing concepts, computing size distributions involves the following: collecting a number of images (taken at uniform time intervals from a stream of bubbles flowing at steady state), applying the threshold criterion to distinguish objects within the image (isolated bubbles from clusters), eliminating the bubble clusters using the shape factor criterion, sizing the remanent objects (mostly isolated bubbles), and grouping them into size classes. Validation of this procedure requires the following: (1) verifying that the sample is representative of the actual population, (2) establishing the number of bubbles that needs to be sized, and (3) confirming that the image analysis algorithm (i.e., the shape factor criterion) does not eliminate valuable information that may lead to the distortion of the size distribution.

In this chapter, an experimental methodology is introduced using bi–modal bubble size distributions.

5.2 Rationale

Consider a column filled with a non-coalescing liquid and equipped with two independently aerated spargers with different pore sizes. If the (volumetric) airflow rate injected through each sparger are similar and the size distribution of the pores is homogeneous, then the resulting volume-based probability bubble size distribution in the column would be bi-modal. Therefore, the proposed technique should reveal the bi-modality and, moreover, the proportions of airflow rates injected through each sparger should correspond to the computed probabilities.

5.3 Experimental

Experimentation was carried out in a 10 cm diameter column operated batch. The porosity of the (cylindrical) spargers was 0.5 μm and 100 μm, generating bubbles from 0.2 mm to 1 mm and from 1 mm to 6 mm, respectively. (Sparger with porosities between 0.5 μm and 100 μm generated size classes that overlapped.) The spargers (made of porous stainless steel tubes, 3.8 cm length and 2.5 cm diameter) were placed vertically at the bottom of the column on a support designed to aerate each independently (Figure 5.1). The continuous phase was tap water containing 50 ppm of frother (Dowfroth 250C). Airflow rates were measured and controlled using two airflow controllers (MKS-5) routinely calibrated. Room temperature was 20 ±1°C.

Optical conditions were: $\theta_L = 16.5°$, $\theta_W = 15°$. Corrections due to system optics were made as described in Chapter 4. The length of the sampling tube was ca. 30 cm. It was immersed 12.5 cm from the top of the column, and was placed half way between the column center and the wall.

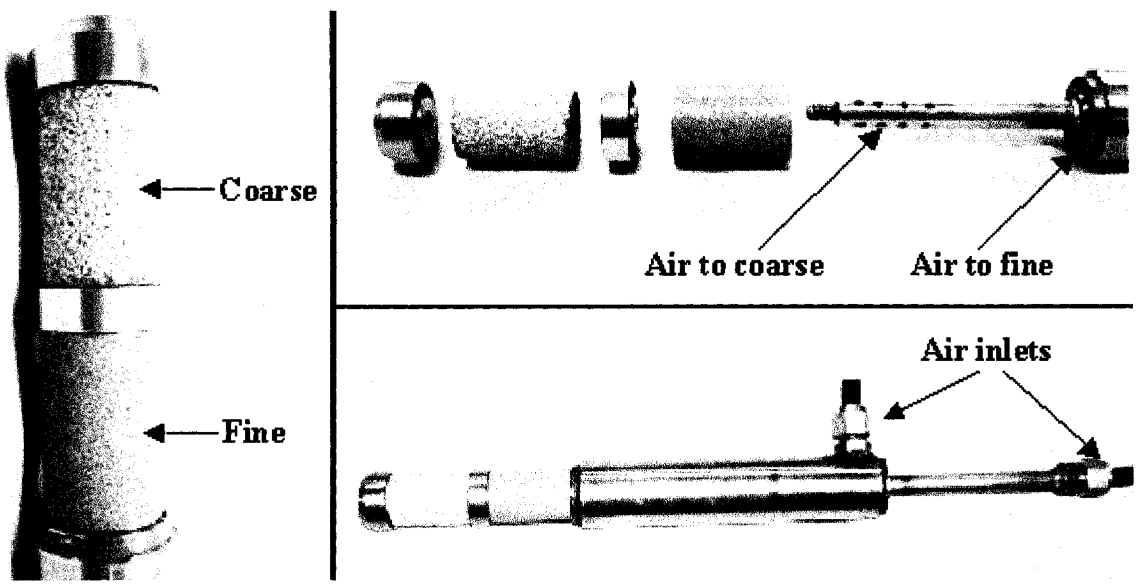

Figure 5.1. The dual-sparger

5.4 Results and discussion

5.4.1 Effect of shape factor

Figure 5.2 shows examples of images when equivalent airflow rates are supplied individually to each sparger. The J_g in the column (0.44 cm/s) is indicated. In the case of the coarse sparger, the shape factor (SF) is close to unity (ca. 0.9) even for ellipsoidal bubbles. Also, it can be seen that a cluster containing three bubbles has a SF = 0.4. In the case of the fine sparger, a 0.4 mm (spherical) bubble has a SF = 0.8, and the smallest isolated bubble in the image (ca. 0.2 mm) has a SF = 0.7. The SF for the ellipsoidal (5 mm) bubble is greater than the spherical (0.4 mm) because the perimeter of the latter has fewer pixels, i.e., the ratio area/perimeter (in Equation 3.1) is less exact.

Figure 5.3. shows the resulting 1:1 mixture (i.e., now the J_g in the column is 0.88 cm/s). The right hand-side edge of the image corresponds to the center of the window. (Recall the assumption that the bubble swarm spreads symmetrically along the center of the window.) It can be seen that small bubbles move away from the center because the large bubbles displace them. The SF of a cluster formed by a 4 mm bubble and a ca. 0.4 mm is 0.8 and for the 2.5–0.4 mm cluster the SF is 0.7. If the SF limit would be set to 0.7, then the indicated bubble clusters in Figure 5.3 would be included and the D_b calculation (Equation 3.2) would be affected. However, increasing the SF limit may cause the exclusion of a significant number of small bubbles. It should be noted that Figure 5.3 illustrates a condition which may not be common in flotation systems, however, the proposed experiment offers the possibility to explore an extreme condition. The analysis is oriented to find the optimum SF.

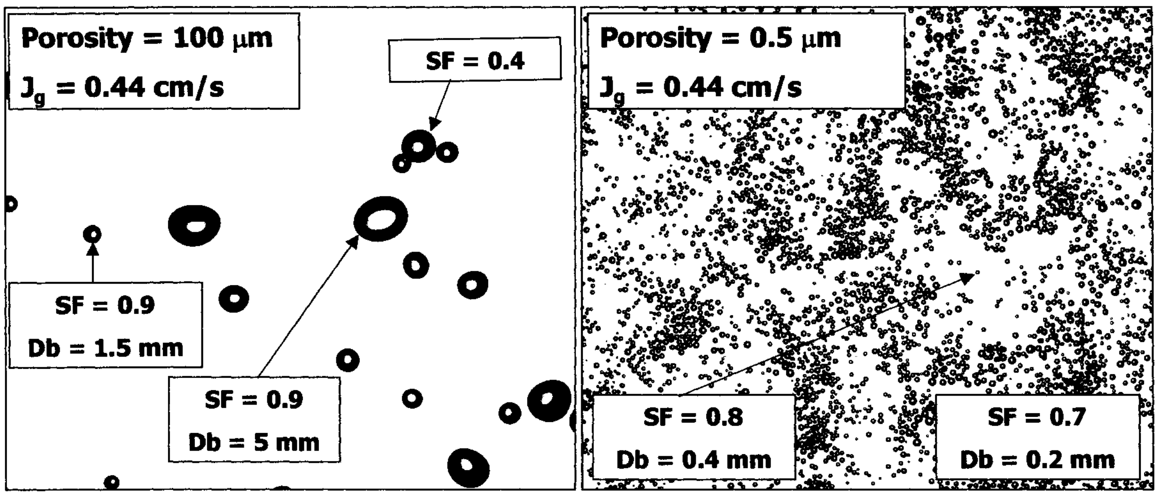

Figure 5.2. Examples of images when same airflow rates are supplied to each sparger individually; left: coarse (100 μm) porosity, right: fine (0.5 μm) porosity

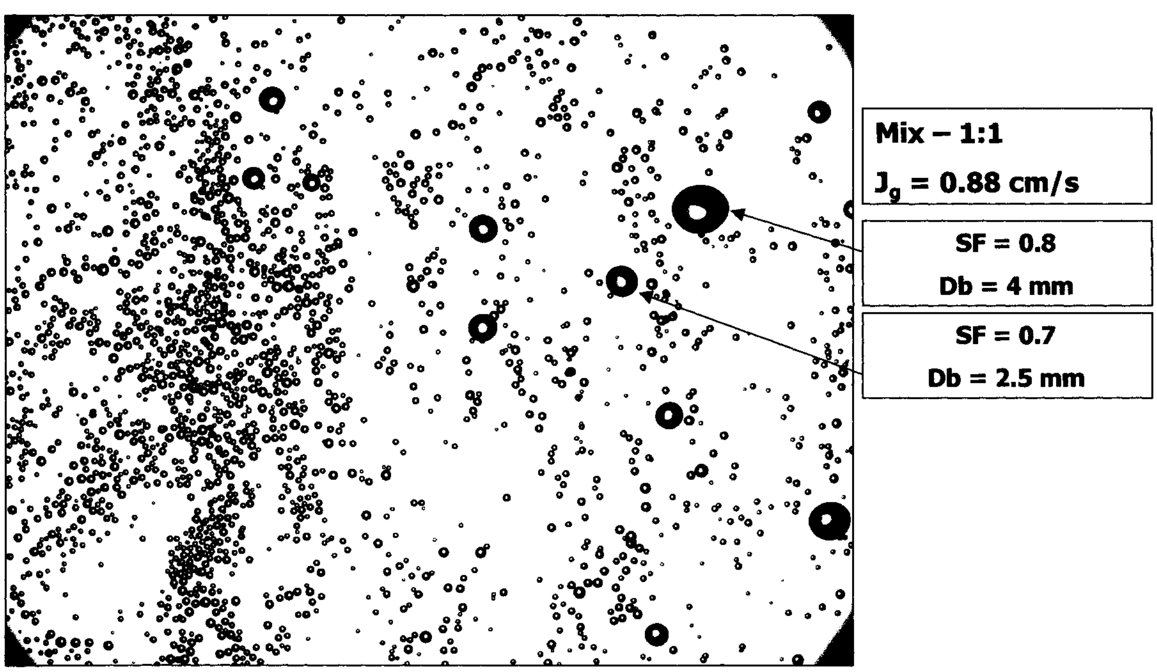

Figure 5.3. Example of image for a 1:1 mixture

Figure 5.4 illustrates the impact of the shape factor limit on average (D_{10}) bubble size for the conditions indicated in Figures 5.2 and 5.3. In the case of the coarse sparger, the average size does not change when SF < 0.5. This is because most objects are isolated bubbles. When SF > 0.5 the D_{10} decreases slightly (ca. 0.1 mm). In the case of the fine sparger, the D_{10} decreases dramatically (ca. 0.2 mm) for SF < 0.6, then stabilizes. Similarly, in the case of the mixture, the D_{10} is strongly dependent on SF when SF < 0.6 but becomes stable after this limit. Also, it can be seen that the % change of counted bubbles is strongly dependent on SF when SF < 0.6 and seems to be independent elsewhere. The SF of 0.6 appears to be a reasonable limit provided that a significant number of bubbles are sized. This is discussed in detail in the following section.

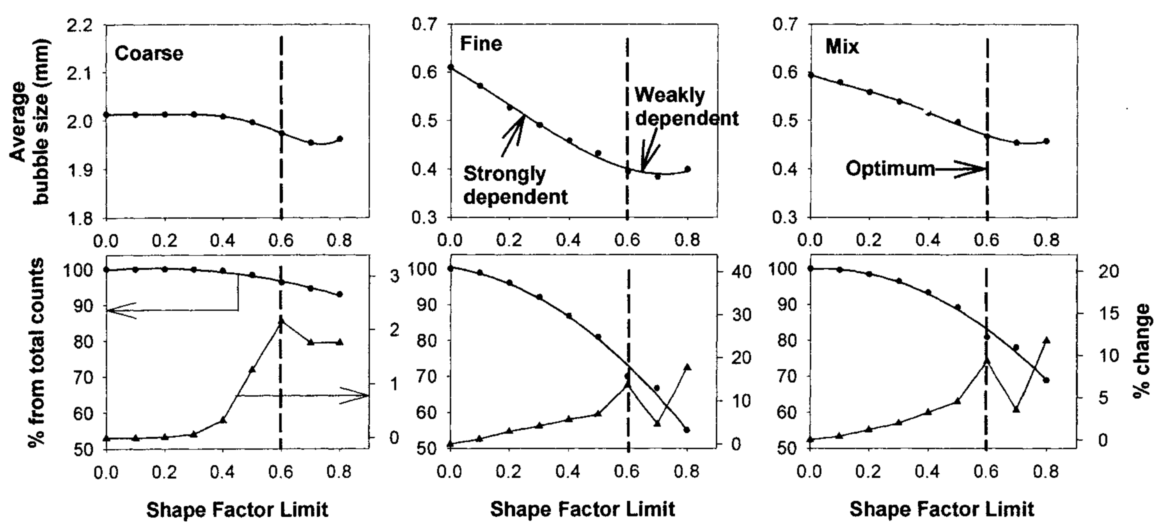

Figure 5.4. The effect of shape factor on average bubble size

5.4.2 Effect of number of bubbles

Figure 5.5 shows the effect of number of sized bubbles on the number- and volume-based size distributions when same proportions of air are supplied to each sparger (J_g in the column = 0.6 cm/s) and the shape factor limit is = 0.6. The results are clearly unrealistic for 3000 bubbles (the volume-based distribution shows at least two modes each). For 10 000 bubbles, the number-based distribution includes two peaks and the volume-based four peaks. After 50 000 bubbles, the number-based is uni-modal (mode ≈ 0.45 mm) but the volume-based still contains three peaks. The results appear to depict reality when 100 000 bubbles are sized, i.e., the volume-based distribution features the anticipated bi-modality. There is no difference in the distributions between 300 000 and 400 000 bubbles suggesting that ca. 300 000 bubbles is sufficient. An interesting observation is that bubbles of ca. 1 mm were not detected which indicates that this size class does not exist in the actual population.

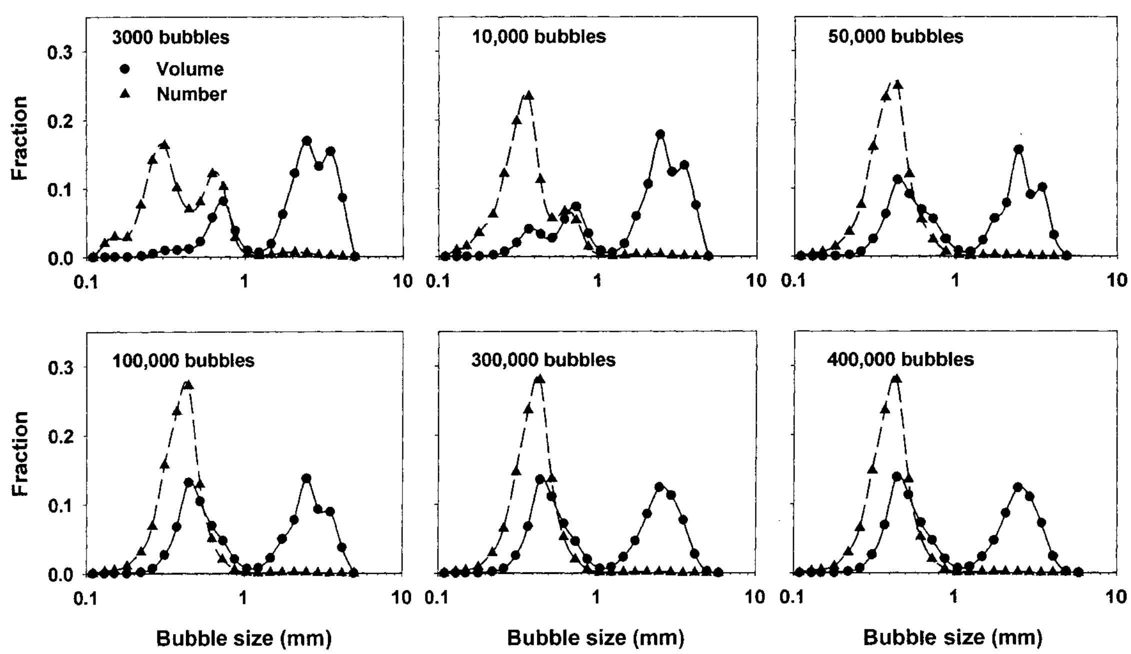

Figure 5.5. Effect of number of sized bubbles for a 1:1 mixture (J_g in the column = 0.6 cm/s)

5.4.3 Proportion quantification

By definition, for the fine sparger:

$$\int PDF^{fine} d(D_b) = 1 \tag{5.1}$$

where, *PDF* is the volume-based probability density function

Similarly, for the coarse sparger:

$$\int PDF^{coarse} d(D_b) = 1 \tag{5.2}$$

And, for the mixture:

$$a\int PDF^{fine} d(D_b) + b\int PDF^{coarse} d(D_b) = 1 \tag{5.3}$$

where the coefficients a and b represent the (volumetric) proportions of air injected to the fine and coarse spargers, respectively.

Figure 5.6 gives an example of estimation of the proportion through each sparger for the case illustrated in Figure 5.5. It can be seen that the *PDF* for the fine sparger is log-normal and for the coarse sparger is normally distributed (the scale on the horizontal-axis is geometric). In the mix, the position of the modes remains nearly unaltered (ca. 0.45 mm for the fine and ca. 3 mm for the coarse). The D_{10} is the same as in the case of the fine sparger indicating that this metric is not sensitive to variations in volume. The D_{32} for the mixture is ca. 1 mm. Note that there are no bubbles which are this mean size!

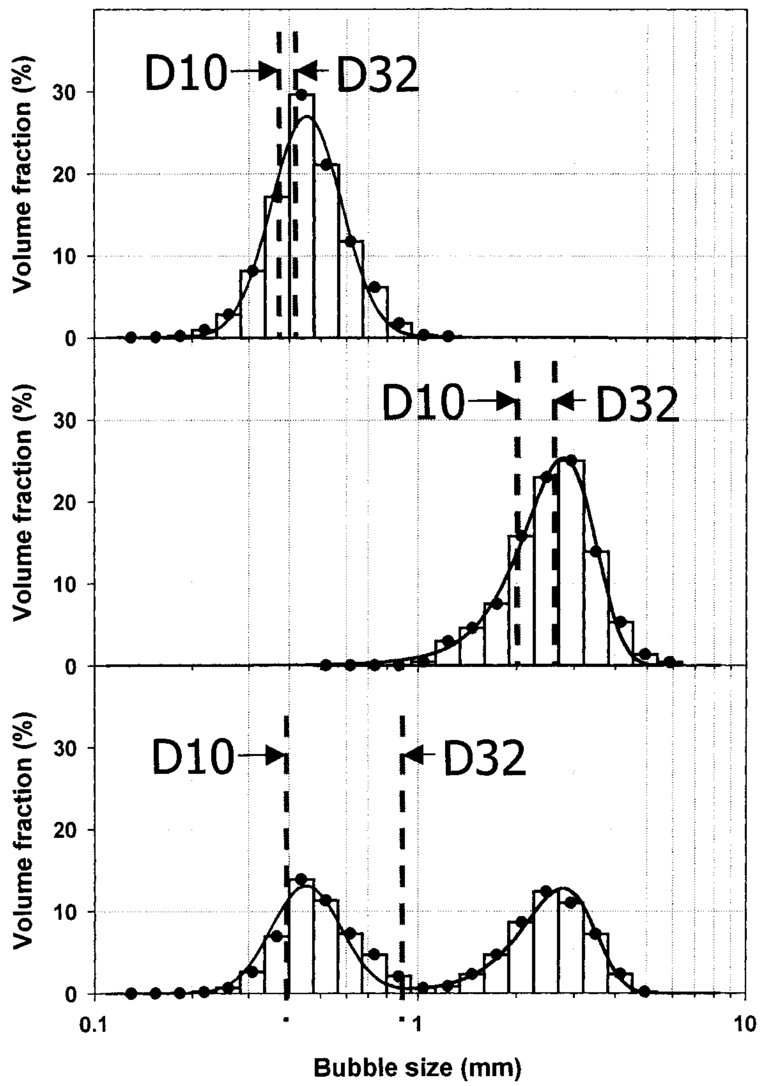

Figure 5.6. Quantification of the proportions
Top: fine sparger, Middle: Coarse sparger, Bottom: Mixture

Since the position of the modes does not vary significantly and the bi-modality is clearly defined, it is reasonable to assume that the left hand-side peak represents only the bubbles produced by the fine sparger and the right hand-side peak corresponds to the bubbles from the coarse sparger. Therefore, the first and second terms in Equation 5.3 can be approximated by Equations 5.4 and 5.5, respectively:

$$A = a \int PDF^{fine} d(D_b) \approx \sum_{i=1}^{i=12} f_i \tag{5.4}$$

$$B = b \int PDF^{coarse} d(D_b) \approx \sum_{i=13}^{i=22} f_i \tag{5.5}$$

where, f_i is the volume-fraction of size class i

(size class 1 is ca. 0.1 mm, size class 13 is ca. 1 mm and size class 22 is ca. 5 mm)

In the example given in Figure 5.6, A = 0.5 and B = 0.5, as expected. This methodology was applied to a range of different air proportions.

Figure 5.7 shows the measured vs. real proportions. The proportions are expressed in terms of the ratio of "areas" relative to the fine sparger, i.e., $A / (A + B)$. The results show that the real and calculated proportions corresponded with a deviation of less than 15%, considered remarkably good given the severity of the test.

5.4.4 Sampling bias

Figure 5.7 gives the impression the sampling/sizing methodology is validated, but it hides a trend. In Figure 5.8, the results are re-plotted in terms of the J_g in the column vs. the error relative to the fine sparger, which is defined by:

$$Error = (A - A^{real})/A^{real} \tag{5.6}$$

(note that, by definition, $A + B = 1$)

This shows the bias was correlated to J_g and as J_g increased the deviation was consistently against fine bubbles.

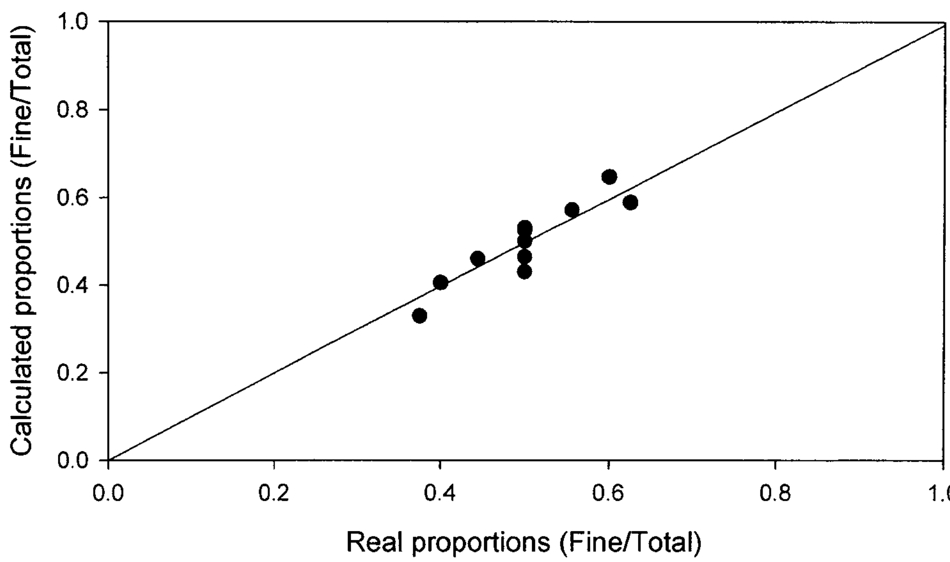

Figure 5.7. Calculated vs. real proportions relative to the fine sparger

To elucidate the sources of bias, the airflow rate entering the viewing chamber was measured using the displaced-volume method, i.e., by recording the time taken for the air to accumulate a certain volume in the viewing chamber (the volume in the viewing chamber was previously calibrated by weighing distilled water). This airflow rate was used to calculate superficial gas velocity in the sampling tube (J_g^{tube}), i.e., the airflow rate entering the viewing chamber divided by the cross-sectional area of the sampling tube. The J_g^{tube} was compared with the J_g in the column; the results are shown in Figure 5.9.

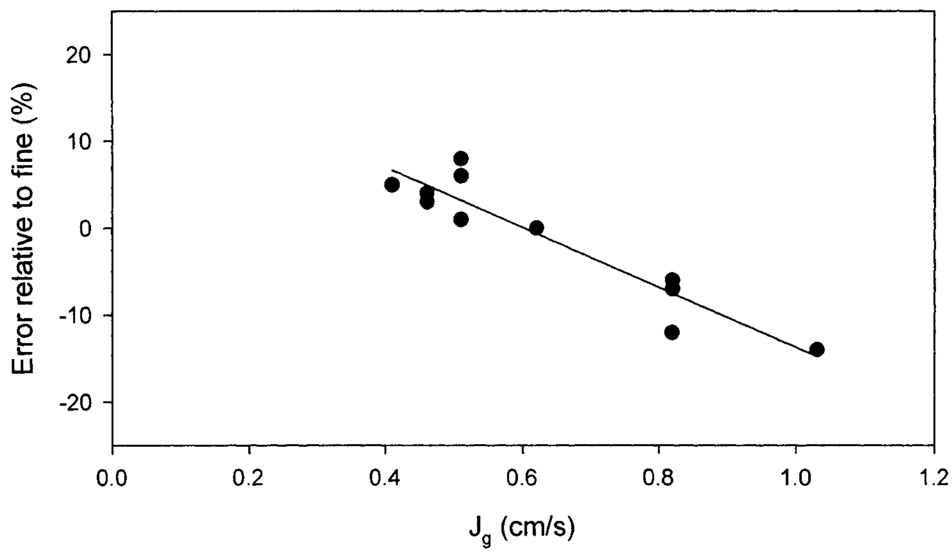

Figure 5.8. Bias against fine bubbles

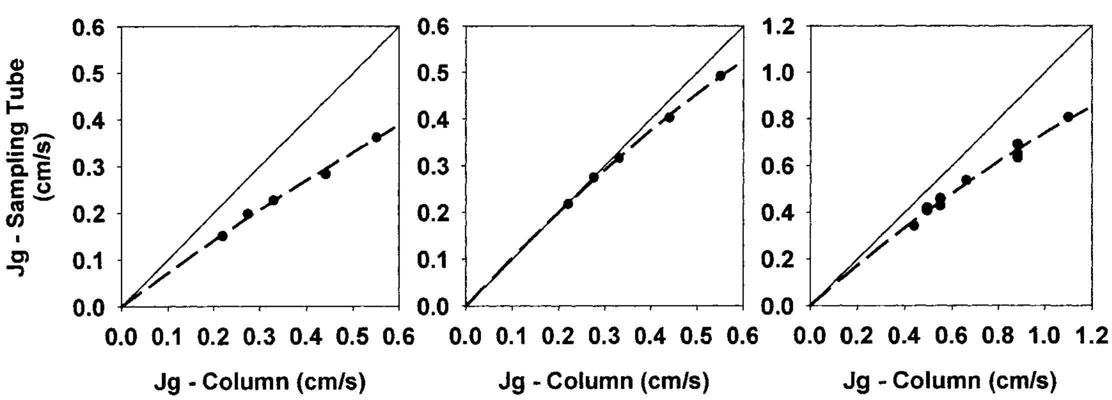

Figure 5.9. Evidence of sampling bias
Left: fine; center: coarse; right: mix

It can be seen that there is a sampling bias: $J_g^{tube} < J_g^{column}$. The deviation is most evident when only fine bubbles are present (ca. 30% at $J_g^{column} = 0.6$ cm/s); indeed, for coarse bubbles: $J_g^{tube} = J_g^{column}$ when $J_g < 0.3$ cm/s. The bias is less pronounced in the case of the mixture than in the case of fine bubbles (ca. 15% at $J_g^{column} = 0.6$ cm/s). Despite this, the main characteristics of the actual population (i.e., the bi-modality) and proportions were seen to be reasonably preserved (Figures 5.6 and 5.7). This suggests that the mechanisms of sampling bias follow complex bubble – sampling tube interactions. Although, the results are not sufficient to reveal the nature of such interactions, some of the possible sources of bias are suggested.

5.4.5 Possible sources of bias

5.4.5.1 Fine bubble – sampling tube interaction

As air accumulates in the viewing chamber, a downward liquid flow in the tube is produced. This downward flow could impede some bubbles from entering and, therefore, reduce J_g^{tube}. The effect would be more in the case of the fine bubbles that have low rise velocities. This effect could be even more significant due to the net reduction of sampling area, i.e., the liquid flows out through the interstices between the bubbles at the entrance of the tube causing a distribution of local liquid velocities, some of which could be considerable.

5.4.5.2 Coarse bubble – sampling tube interaction

The probability for a bubble to be collected (governed by the size of the tube cross-sectional area) decreases as bubble size increases. Also, the probability for a bubble to interact with the tube increases as bubble size increases: it has been observed that coarse bubbles are more prone to break when they contact the edge of the tube. This may cause a reduction of J_g^{tube} because only bubble fragments may enter.

5.4.5.3 Coarse bubble – fine bubble interaction

The volume of the wake behind rising bubbles increases as bubble size increases[2]. Fine bubbles might be entrained in the wake of coarse bubbles, reducing their sampling rejection and accelerating their motion, i.e., entrained fine bubbles will tend to move faster. On the other hand, coarse bubbles in the swarm will tend to ascend more slowly as they move in a more tortuous environment, i.e., the higher the bubble concentration, the higher the tortuosity. The combination of these two effects may explain the conservation of the proportions in Figure 5.6 and the reduction of J_g bias in the graph of Figure 5.9, compared to the graph on the left-hand side.

5.4.5.4 Volumetric- vs. Flux-based size distributions

Deglon (1998) discussed that there is an intrinsic tendency to overestimate the number of small bubbles with the imaging method because the size distribution obtained from the images is volumetric-based whereas the size distribution entering the sampling tube is flux-based. Figure 5.10 depicts an idealized case with large and small bubbles (moving at ½ the velocity) that can be used to illustrate the difference between size distribution defined from a volumetric and a flux perspective.

If one large and one small bubble enter the sampling zone every second then at steady state one large and one small bubble will leave the top of the zone every second. In the example shown in Figure 5.10, the frequency distribution obtained from a flux perspective is $F'(D_{b1}) = 1/2$ and $F'(D_{b2}) = 1/2$, where suffixes 1 and 2 correspond to the small and the large bubble, respectively. From a volumetric standpoint since the small

[2] Indeed, it is the Reynold's number ($Re = \rho\ D_b\ u_b\ /\ \mu$) that is correlated to the wake volume (Clift et al., 1978). For a system in which the continuous medium has constant density (ρ) and viscosity (μ) and in the presence of surfactants, the steady state velocity u_b increases with D_b.

bubble moves at ½ the speed of the large bubble the frequency distribution is $F(D_{b1})$ = 2/3 and $F(D_{b2})$ = 1/3.

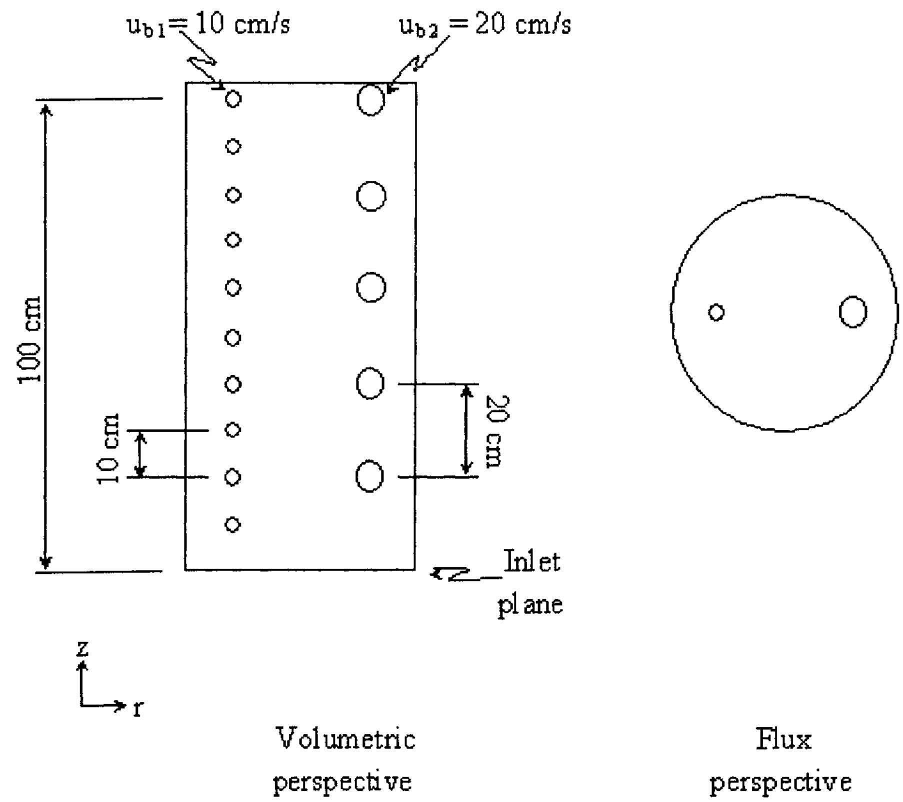

Figure 5.10. Illustration of volume and flux-based sampling

In this simple example, transforming the volumetric-based bubble size distribution (F) into a flux-based distribution (F') is rather straightforward:

$$F'(D_{b1}) = \frac{(10cm/s)(2/3)}{(10cm/s)(2/3) + (20cm/s)(1/3)} = \frac{1}{2} \tag{5.7}$$

$$F'(D_{b2}) = \frac{(20cm/s)(1/3)}{(10cm/s)(2/3) + (20cm/s)(1/3)} = \frac{1}{2} \tag{5.8}$$

Generalization of the transformation between bubble size distributions is given as follows:

Let N_{bi} and N_{bFi} be, respectively, the number of bubbles of size class i per unit volume and the number of bubbles of size class i passing through a plane of unit cross sectional area per unit time (*i.e.*, the flux). Therefore,

$$F(D_{bi}) = \frac{N_{bi}}{\sum_i N_{bi}} \tag{5.9}$$

$$F'(D_{bi}) = \frac{N_{bFi}}{\sum_i N_{bFi}} \tag{5.10}$$

In steady state, transforming N_{bi} to N_{bFi} is given by Equation 5.11:

$$N_{bFi} = u_{bi}(D_{bi})N_{bi} \tag{5.11}$$

From Equation 5.11 in conjunction with Equations 5.9 and 5.10, a volumetric-based distribution can be transformed to a flux-based distribution using Equation 5.12[3]:

$$F'(D_{bi}) = \frac{u_{bi}(D_{bi})F(D_{bi})}{\sum_i u_{bi}(D_{bi})F(D_{bi})} \tag{5.12}$$

[3] This equation was derived by Deglon (1998) and has been transcribed here to facilitate discussion

The bubble rise velocity (u_b) is needed to solve Equation 5.12. A first approximation would be to obtain u_b from relationships applicable to quiescent conditions with the assumption that interaction between bubbles does not significantly influence u_b, such as in the example given in Figure 5.10. However, as discussed in the previous section, bubble–bubble interactions may be complex especially in the case of broad size distributions and with high bubble concentrations. Moreover, in the case of the present technique, the bubble velocity associated with the images is affected by the presence of the inclined window, i.e., u_b on the window is anticipated to be a function of θ_W.

On the other hand, the intrinsic overestimation of small bubbles in the imaging method tends to mitigate the bias in sampling against fine bubbles evident in Figure 5.8.

5.5 Conclusions

An experimental methodology is introduced based on the controlled generation of bi–modal bubble mixtures to try to verify whether the computed size distributions are representative of the actual population. The results showed the anticipated bi-modality in which the real and calculated proportions corresponded with a deviation of less than 15%, remarkably good considering the severity of the test. However, the deviation was correlated to the superficial gas velocity (J_g) in the column and was consistently against smaller bubbles. It was observed that, regardless of the characteristic of the mixture, $J_g^{tube} < J_g^{column}$. This suggested that the mechanisms of sampling bias followed complex bubble – sampling tube interactions. The results were not sufficient to reveal the nature of such interactions. Possible sources of bias were suggested.

CHAPTER 6

COMPARISON BETWEEN SAMPLING-BASED TECHNIQUES: ISOKINETIC COLLECTION VS IMAGING

This chapter reports a laboratory and plant comparison between the UCT bubble size analyzer (sampling-followed-by-isokinetic-collection) and the technique under study (sampling-followed-by-imaging) which, hereafter, is referred to as the McGill University bubble sizing method. The laboratory work was conducted on single bubbles to establish the accuracy of the techniques by comparing with the displaced-volume method (regarded as the reference). The techniques were compared in a 50-m^3 industrial-scale mechanical flotation cell processing a Zinc ore at Red Dog mine (northern Alaska) during the summer of 2002.

6.1 Review

The UCT method comprises a sampling tube attached to a water reservoir in which a capillary tube is placed (Figure 2.1). The sampled bubbles ascend through the sampling tube to the reservoir. A fraction of the bubbles that reach the reservoir are suctioned into the capillary tube where they are converted into cylinders (slugs) and their lengths and velocities measured with two optical detectors. The total volume of gas captured by the capillary tube is measured and individual bubble sizes are determined as a fraction of this total volume (Equation 2.4).

Depending on the suction rate (controlled by a peristaltic pump) bubbles can approach being collected isokinetically in the capillary tube (in fact, proper sampling with the UCT technique is a combination of non-isokinetic (in the sampling tube) and isokinetic sampling (in the water reservoir)), i.e., the higher the suction rate, the closer to the isokinetic condition. Isokinetic collection is desirable because this reduces bubbles interaction as they enter and flow in the capillary. It has been observed that high suction rates minimize preferential selection of specific bubble sizes. However, excessive suction rates may cause bubble breakup: Grau and Heiskanen (2002) showed that bubbles > 3 mm broke when using a 0.1 cm I.D. capillary tube at a non specified suction rate.

In the McGill University technique, bubbles from the dispersion travel in the sampling tube under non-isokinetic conditions.

6.2 Experimental

A series of experiments was conducted in the laboratory to determine the accuracy of sizing single bubbles. Measurements were compared versus the displaced-volume method. In the case of the UCT device, preliminary experiments were carried out to establish the optimum suction rate. The techniques were then compared on an industrial-scale mechanical flotation cell.

6.2.1 Laboratory work

Bubbles in the single bubbling regime were generated. To this effect, three glass capillary tubes (capillaries used to generate bubbles; should not be confused with the capillary used by the UCT device) with orifices 51, 178 and 406 mm were placed individually at the bottom of a column of clear plastic (38 mm I.D., 215 mm height). The column was filled with a solution of frother (MIBC) in water (50 mg of solute per kg of solution) and the airflow was controlled with a pressure regulator.

6.2.1.1 The UCT Bubble Size Analyzer

As illustrated in Figure 6.1, the sampling tube and the water reservoir were detached from the UCT assembly enabling the capillary (0.5 mm I.D.) to be placed directly into the bubble stream. The cumulated gas volume in the burette (which is needed to compute bubble size) varies depending on the number of collected bubbles and the gas pressure in the burette. (It should be noted that the two techniques under study output raw bubble size data which are taken under different pressure and temperature conditions, therefore, corrections have to be made.) Bubble size is reported at 25°C (ca. 298 K) and 1 atm (ca. 1033 cm of water) using the approximation given by equation 6.1:

$$D_b = D_b' \sqrt[3]{\left(1 - \frac{1}{2}\frac{H_1 + H_2}{1033}\right)\left(\frac{298}{T + 273}\right)} \qquad (6.1)$$

where, D_b' is the raw bubble size (using the volume from the burette),

D_b is the bubble size corrected to standard conditions,

T is the room temperature (in °C), and

H_1 and H_2 are the distances (in cm) between the water level in the overflow tank and the initial and final water levels in the burette, respectively.

Equation 6.1 adjusts the volume the volume at 25°C and 1 atm taking an average between the initial and final gas pressures in the burette and using the ideal gas equation. H_1 and H_2 varied from 100 to 138 cm and room temperature between 25 and 26°C.

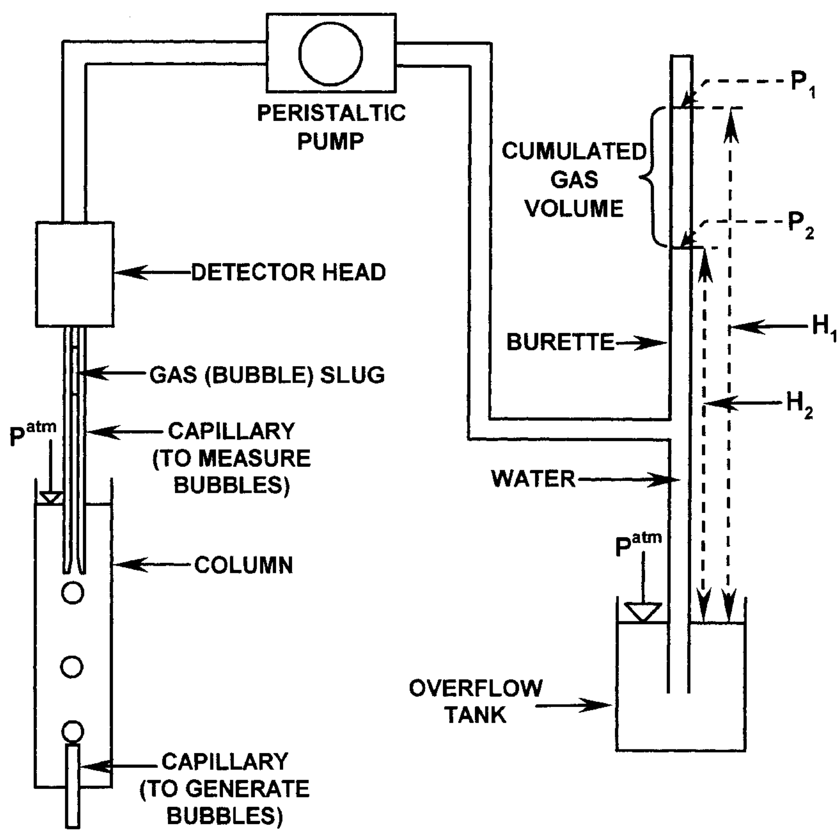

Figure 6.1. Experimental setup used for sizing single bubbles with the UCT technique

6.2.1.2 The McGill University Bubble Size Analyzer

Images were recorded onto an NTSC-DV (digital video) tape at a rate of 30 frames per second. The camera (Canon model GL-1) was set to f/5.6 (aperture stop) and 1/4000s shutter speed. The images were transferred onto the hard disk of a personal computer using an IEEE 1394 interface that allows the transfer of full-resolution (720x480 pixels) images. Images from the tape were captured at a rate of three frames per second and stored as 8-bit (256 intensity grey levels) monochrome TIFF files using a commercial program (Orange Link). It should be noted that NTSC-DV images use rectangular pixels with an aspect ratio of ca. 0.9. This causes, for example, circles to appear as ovals on a computer screen. A standard procedure to create square pixels was followed which consists of resizing the frames to 720 x 538 pixels (ca. standard frame aspect ratio of 3/4) using the image analysis program. Prior to bubble sizing, the magnification factor was determined by acquiring an image with a standard circle of known size (a single hole grid of 0.31 cm O.D. manufactured by Soquelec) placed in the focus plane and counting the number of pixels across the circle diameter. The use of the standard circle is convenient because it can also be used to confirm the squared-pixel procedure (i.e., after frame resizing, the horizontal and vertical axes should be of equal length).

Images were thresholded at half the grey scale. The equivalent spherical diameter was calculated as described in section 3.2. Figure 6.2 shows the setup used for the McGill University technique. Equation 6.2 was used for pressure and temperature corrections (i.e., applying the ideal gas law directly).

$$D_b = D_b' \sqrt[3]{\left(\frac{1033 - H_i}{1033}\right)\left(\frac{298}{T_i + 273}\right)} \tag{6.2}$$

where, D_b is the bubble size corrected to standard conditions,

D_b' is the raw bubble size (as taken from the images),

H_i is the distance (75 cm) between the water level in the column and the point at which the images are collected, and

T_i is the water temperature (25°C) in the viewing chamber

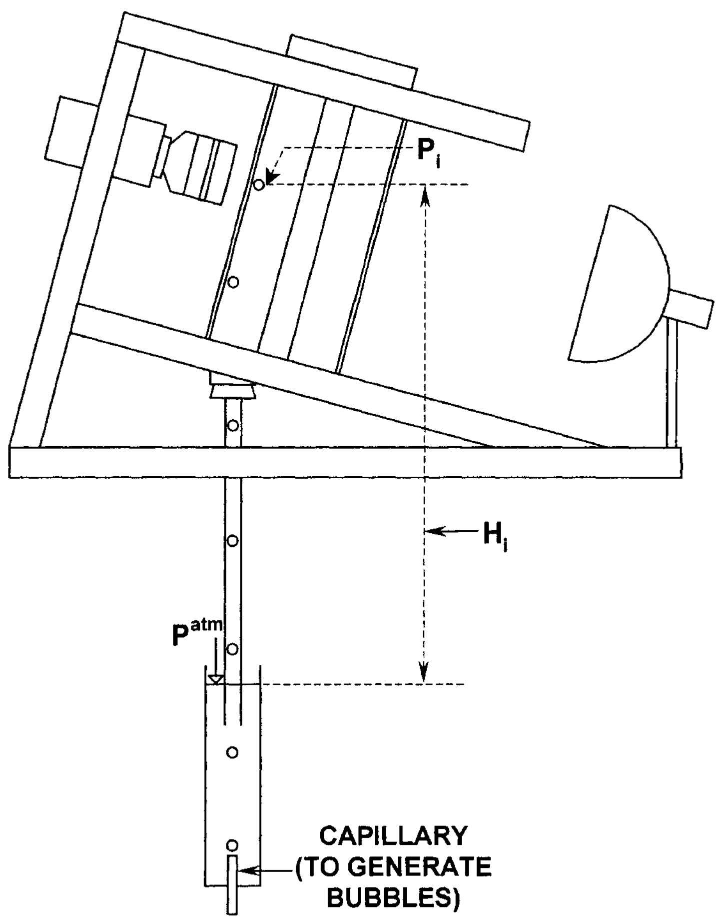

Figure 6.2. Experimental setup used for sizing single bubbles with the McGill University technique

6.2.1.3 The displaced-volume method

The burette (a graduated glass cylinder, ca. 12 cm height and 1.3 cm I.D., with 10 cm^3 nominal capacity and 0.2 cm^3 divisions) was filled with the frother-water solution and placed upside down to intercept the stream of bubbles, as depicted in Figure 6.3. The time (t) taken for the gas to accumulate a certain volume (V) was recorded. The bubble departing periods (p) were determined with a video camera and an equivalent spherical bubble diameter (D_b) was calculated from equation 6.3:

$$D_b = \sqrt[3]{\frac{6Vp}{t\pi}} \qquad (6.3)$$

Since the average between the initial and final gas pressures in the burette (P_1 and P_2 in Figure 6.3, respectively) is approximately equal to the atmospheric pressure, no correction is necessary.

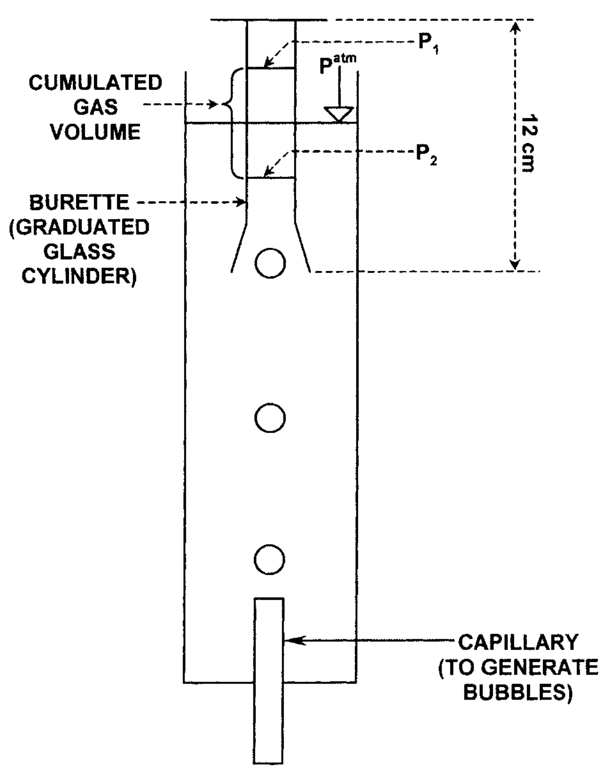

Figure 6.3. Experimental setup used for sizing single bubbles with the displaced-volume method

6.2.2 Plant work

The UCT and the McGill University techniques were compared in an industrial-scale mechanical flotation cell at Teck Cominco's Red Dog operation Alaska. The machine (a 50-m^3 nominal capacity Outokumpu tank cell model OK-50) was located in the cleaner stage of the Zn flotation circuit (particle size, approx. 80% minus 20 μm). The airflow rate to the machine was 150 SCFM (standard cubic feet per minute). The sampling tubes were placed about half way between the centre and cell wall and at ca. 50 cm below the froth/pulp interface.

6.2.2.1 The UCT Bubble Size Analyzer

The device was reassembled to its basic configuration (Figure 2.1). An air actuated valve, located at the bottom end of the sampling tube (ca. 2 m long), was opened allowing the bubbles to rise for ca. 20 to 30 s before they were drawn into the capillary (longer times would cause excessive accumulation of solid particles due to the limited volume of the water reservoir). Bubble suctioning took between 45 and 60 s to capture ca. 1200 to 2700 bubbles in each of the five executed tests. H_1 and H_2 varied from 100 to 113 cm and ambient temperature was constant (ca. 31°C). Corrections for temperature and pressure were made as described above (section 6.2.1.1).

6.2.2.2 The McGill University Bubble Size Analyzer

A rubber stopper was used to seal the sampling tube (1.3 cm I.D. and ca. 2 m long) permitting immersion in the cell. When removed the bubbles entered. The camera settings were the same as in the laboratory work (f/5.6 and 1/4000 s). Video images were recorded from the time the rubber stopper was detached.

The shape factor limit was 0.6 (Section 3.2). Water temperature in the viewing chamber was constant (ca. 18°C). The pressure at the point of image capture was measured directly with a vacuum pressure gauge placed on the top of the viewing chamber (the vacuum pressure was measured when the accumulating gas was sufficient for the water level in the viewing chamber to reach the point where the image was captured). Bubble size was corrected to standard conditions assuming the ideal gas law.

6.3 Results and discussion

6.3.1 Laboratory work

6.3.1.1 Effect of suction rate on the UCT method

To assess the effect of suction rate using the UCT device, the 178 mm orifice was selected and the pressure in the regulator was set to 34.5 kPa (5 psi). At these conditions, it was observed that bubbles were not of equal size (out of the single bubbling regime). The computed size distribution is given in Figure 6.4. A unimodal distribution with mode ca. 2.1 mm was obtained when operating at low suction rates. A gradual transition from unimodal to bimodal distribution was observed with increase in suction rate indicating that bubble breakup was occurring. Figure 5.5 illustrates the variation of the Sauter mean (D_{32}) and the number mean (D_{10}) bubble size with suction rate. The two mean values show very distinct behaviour: The D_{10} decreases ca. 40% whereas the D_{32} decreases less than 5% evidencing the importance of using the two mean values rather than just one.

The D_{32}/D_{10} ratio is also indicated in Figure 6.5. Equal to 1 for bubbles of uniform size, the ratio increases as the distribution broadens. As depicted in Figure 6.6, nearly identical size distributions were obtained with the McGill University technique and the UCT device operating at a suction rate of 0.32 cm^3/s. This suction rate was selected as the optimum, minimizing bubble breakup while more likely than the suction rate of 0.14 cm^3/s to achieve iso-kinetic conditions.

6.3.1.2 Single bubble measurements

For each orifice size (51, 178 and 406 mm), the regulator pressure was adjusted to achieve an airflow rate sufficiently low to be in the single bubbling regime (103.4, 6.9 and 3.4 kPa (15, 1 and 0.5 psi), respectively). The departing periods were 0.13, 0.06 and 0.05 s, respectively. Table 6.1 presents the comparison of the UCT and the McGill University techniques versus the displaced-volume (burette) method. The error in Table 6.1 represents the relative difference against the reference method (equation 6.4).

$$Error = \frac{D_{10} - D_R}{D_R} \tag{6.4}$$

where, D_R is the reference bubble size (from the volume-displaced method), and

D_{10} is the number mean bubble size

(in the single bubbling regime $D_{10} = D_{32}$)

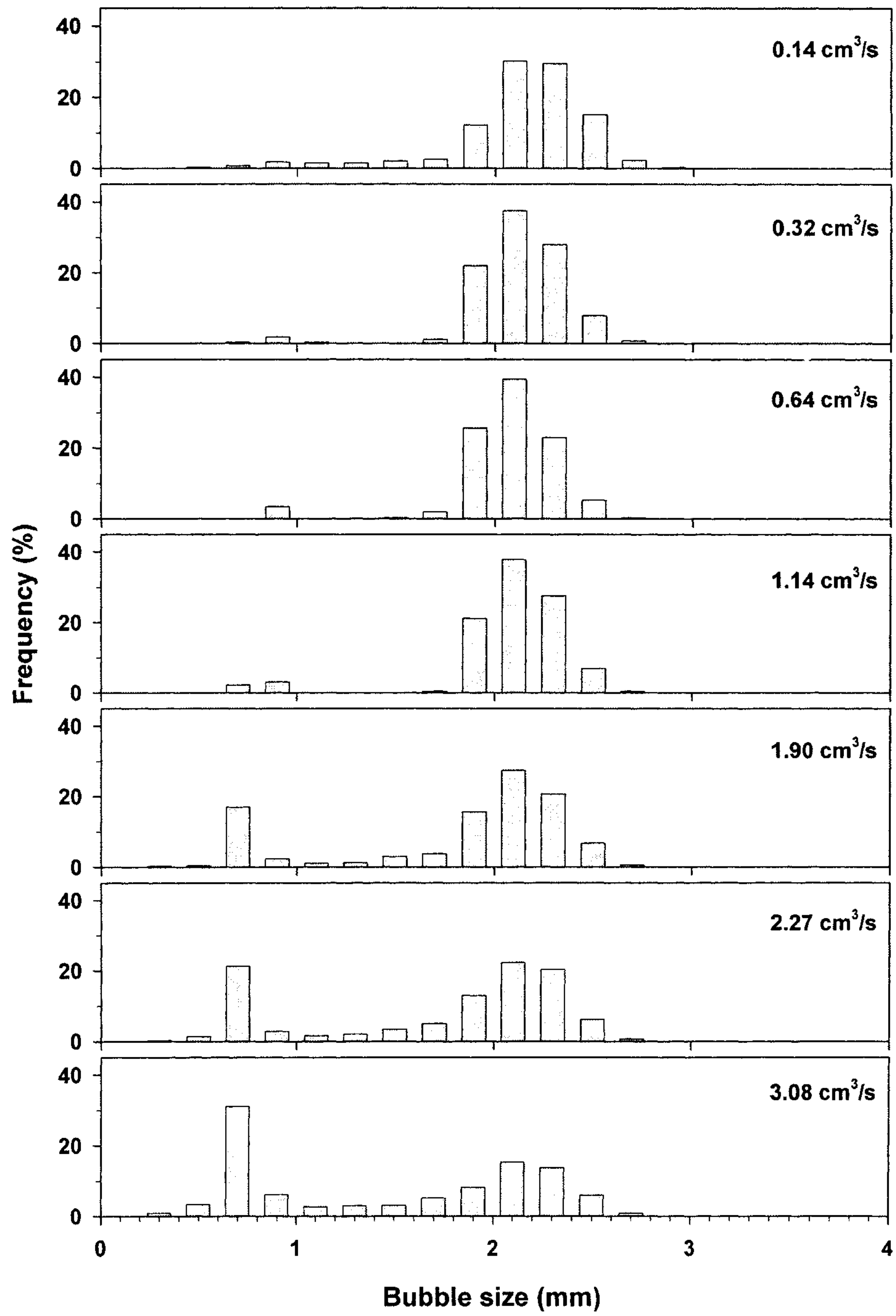

Figure 6.4. The effect of suction rate on bubble size using the UCT technique

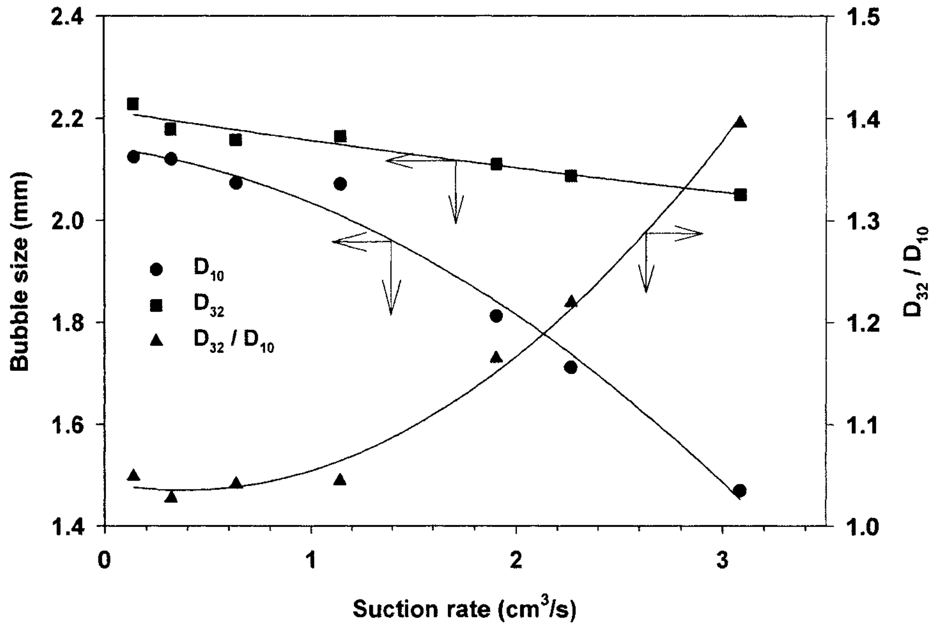

Figure 6.5. The effect of suction rate on mean diameter using the UCT technique

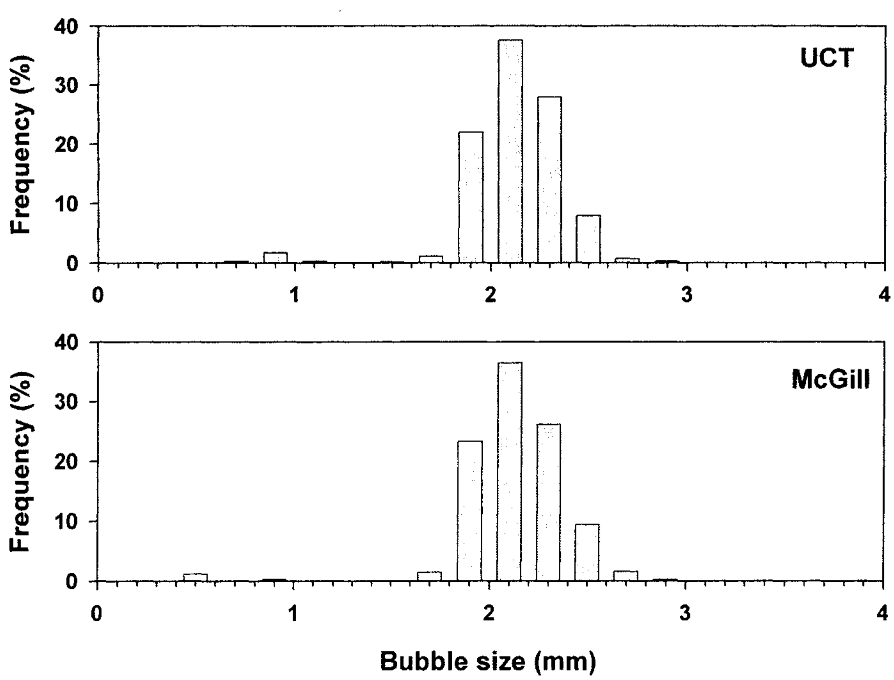

Figure 6.6. Comparison of bubble size distribution between the UCT (0.32 cm^3/s suction rate) and McGill University techniques

Table 6.1. Single bubble size measurements obtained with the UCT, the McGill University and the displaced-volume (burette) techniques

Orifice	Burette	D_{10} (mm)		D_{32} (mm)		Error (%)		D_{32}/D_{10}	
(μm)	(mm)	UCT	McGill	UCT	McGill	UCT	McGill	UCT	McGill
51	1.30	1.31	1.25	1.31	1.25	0.77	-3.85	1.00	1.00
178	1.96	1.98	1.97	1.98	1.97	1.02	0.51	1.00	1.00
406	2.65	2.52	2.63	2.62	2.64	-4.91	-0.75	1.04	1.00

The overall impression is that both methods give accurate results, error < 5%. In two cases the McGill University technique slightly underestimated which is expected from the effect of defocus distance (Chapter 4). Although the error appears minor, it should be noted that a 4% error for a 1 mm bubble implies an 8% deviation in the calculation of bubble surface area (bubble surface estimation is of importance for various flotation models). The discussion in Chapter 4 explains the underestimation trend. However, the bias in Table 6.1 is larger than in that previous study (ca. – 4% in one case) because of the poorer quality camera (i.e., the image sensor of the video camera used in this comparison contains fewer pixels increasing measurement uncertainty).

The measurements obtained with the UCT device with the 51 and 178 mm orifices indicate that there is a small tendency to overestimate bubble size (ca. 1%). Some validation studies of techniques similar to the UCT method show the same trend, attributing it, in part, to the fact that the actual shape of the bubble slug in the capillary is not exactly an ideal cylinder because of its convex ends. Also, it has been demonstrated that the thickness of the liquid film surrounding the bubble contributes to this overestimation when the computed bubble size is based on the dimensions of the capillary and the length of the gas slug. For example, Greaves and Kobbacy (1984) determined an average overestimation of ca. 9% compared with a known volume bubble injected in the inlet of a 0.61 mm I.D. capillary. They proposed a semi-empirical correction formula for 0.3 mm < D_b < 6 mm. After correcting with another semi-empirical equation, Zhang et al. (1989) observed a maximum deviation of 3% over the measurements obtained by a photographic method. Recently, Du et al. (2001) reported a <5% error after using Greaves and Kobbacy's formula. In these three cases, bubble size calculations were based solely on the dimensions of the capillary (i.e., the inner cross sectional area, A) and the length of the gas slug (derived from the bubble velocity in the capillary and the distance L between the photoelectric sensors). However, these parameters (A and L) are not easily quantified. Anticipating this problem, the UCT technique uses a different methodology which consists of computing individual bubble volumes as fractions of the total sampled volume (Equation 2.4). Therefore, the UCT approach reduces the overestimation trend.

The ca. – 5 % error obtained when using the 406 mm orifice (generating a ca. 2.7 mm bubble) with the UCT device was due to bubble breakup ($D_{32}/D_{10} \neq 1$). Confirmation of this is given in Figure 6.7, in which the calculated size distribution is no longer uni-sized. A capillary with larger I.D. along with a proper determination of the optimum suction rate would resolve this problem. Randall et al. (1989) used a 1 mm I.D. capillary to consistently size bubbles of ca. 2.8 mm.

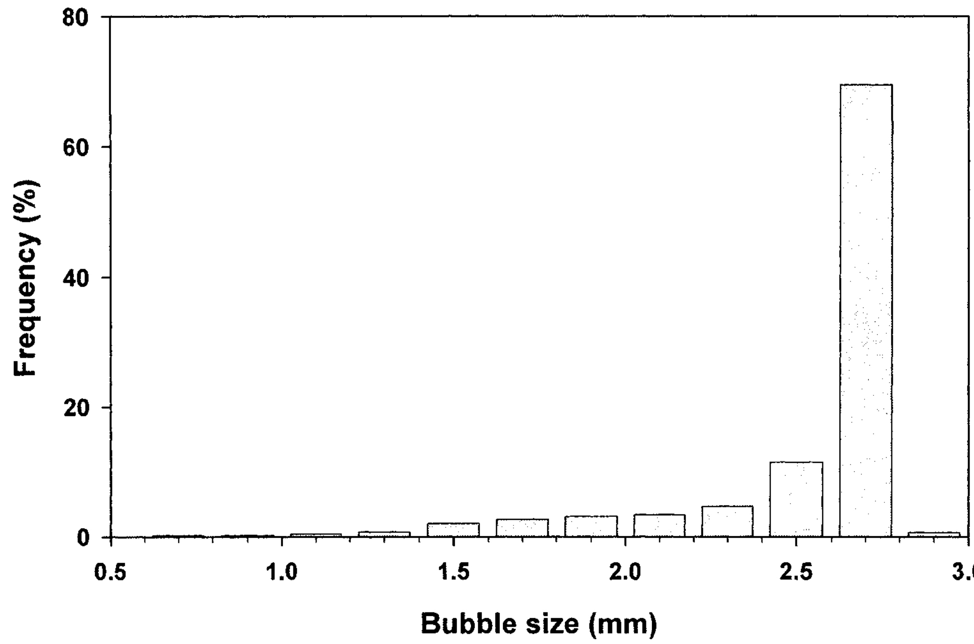

Figure 6.7. Evidence of bubble breakup of a ca. 2.7 mm bubble using the UCT technique

6.3.2 Plant work

Figure 6.8 depicts replicate tests obtained with the McGill University technique showing the variation of D_{10} versus the number of bubbles counted (the analysis started with the first image containing a bubble). The D_{10} was calculated every cycle of 100 bubbles. The approximate time (from the first analyzed image) is also indicated. It can be seen that the D_{10} decreases during the first 45 s (ca. 5000 counted bubbles), then stabilizes. This transient phase reflects the fact that bubbles of different sizes move at different velocities (i.e., larger bubbles arrive first in the viewing chamber). We can arguably suggest that the D_{10} will keep decreasing, however, the image processing was stopped at 20 000 bubbles since this facilitated the use of the single threshold value (after 20 000 bubbles (ca. 120 s) turbidity in the viewing chamber became significant as particles accumulate after their release when the bubbles burst, necessitating resetting the threshold). The standard procedure is to compute size distributions based on counting bubbles once the D_{10} stabilizes (between 5000 and 20 000 bubbles in this case).

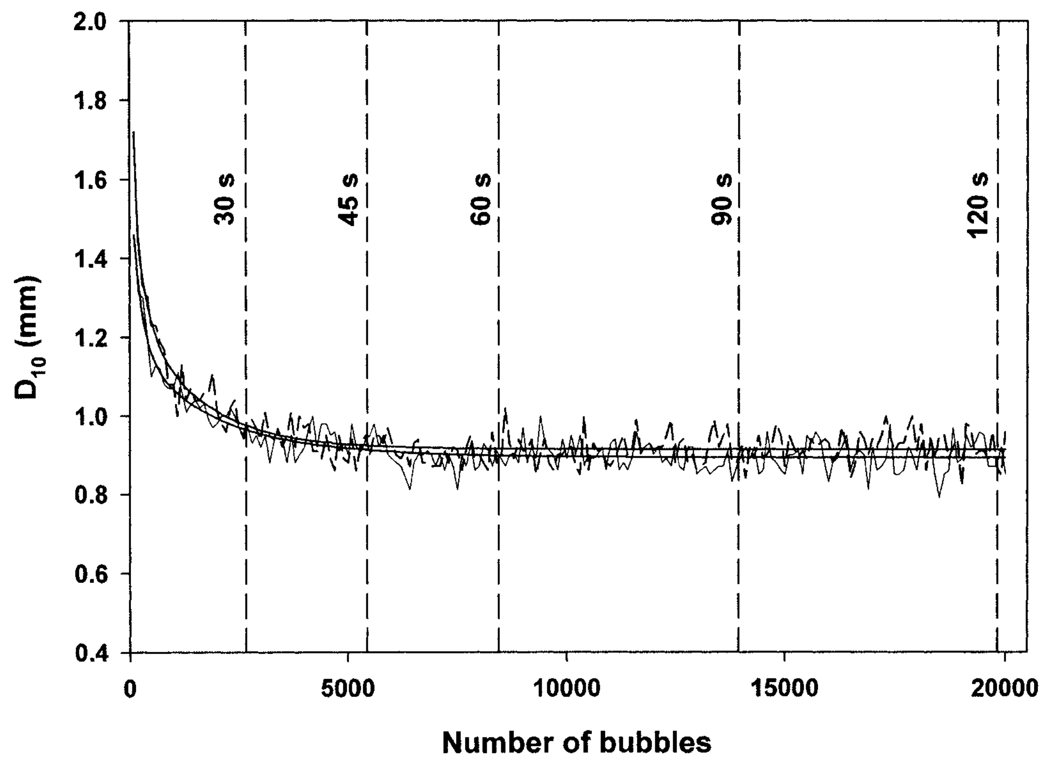

Figure 6.8. The variation of the number mean with the number of bubbles using the McGill University technique

Figure 6.9 presents the computed size distributions with the UCT and the McGill University techniques. The UCT histogram is the overall of the five experiments containing between 1200 and 2700 bubbles each. In the McGill University technique, the distribution is based on the two experiments of 15 000 analyzed bubbles each. The D_{10}, D_{32} and the ratio D_{32}/D_{10} are also indicated. The difference between the mean values is ca. 11% ($D_b^{UCT} > D_b^{McGill}$) but the ratio D_{32}/D_{10} is virtually the same, i.e., they both sense a similar breadth of distribution. From the single bubble analysis (section 6.3.1.2 above) we could expect a discrepancy of ca. 5% for bubbles of 1 mm to 2 mm, which is not enough to explain the 11% difference. Given that in the UCT technique bubbles are not collected completely iso-kinetically, the small number of bubbles collected may be biased towards the larger ones, as Figure 6.8 indicates occurs in the McGill University procedure. Overall, however, the agreement between the two techniques is good considering that sampling and sizing procedures are quite different. In the UCT device, bubbles are collected under non iso-kinetic conditions as they rise in the sampling tube. They continue ascending in the water reservoir in a more dilute (or less crowded) environment but still under non iso-kinetic conditions. A fraction of the bubbles is then iso-kinetically collected in the capillary. On the other hand, sampling with the McGill University technique proceeds under non iso-kinetic conditions throughout.

6.4 Conclusions

The optimum suction rate for the UCT bubble size analyzer ($0.32\ cm^3/s$ for $1\ mm < D_b < 2\ mm$ and a capillary tube of 0.5 mm I.D.) was determined by quantifying bubble breakup. By comparison with single bubbles of known size (determined by the displaced-volume technique), a small overestimation of ca. 1% was observed. A tendency to overestimate has been reported elsewhere, however, it is less with the UCT approach than other similar techniques that use only the geometry of the capillary and the length of gas cylinders to compute bubble size. Calculating individual bubble sizes as fractions of the total volume of gas collected as in the UCT method is, therefore, more accurate. A tendency to underestimate was observed when sizing the single bubbles with the McGill

University technique. This underestimation trend was anticipated due to the contribution of defocus distance.

The plant comparison showed that $D_b^{UCT} > D_b^{McGill}$ but the ratio D_{32}/D_{10} was the same. The discrepancy was greater than expected from the single bubble results. However, overall the techniques agreed well considering their distinct sampling and measuring principles.

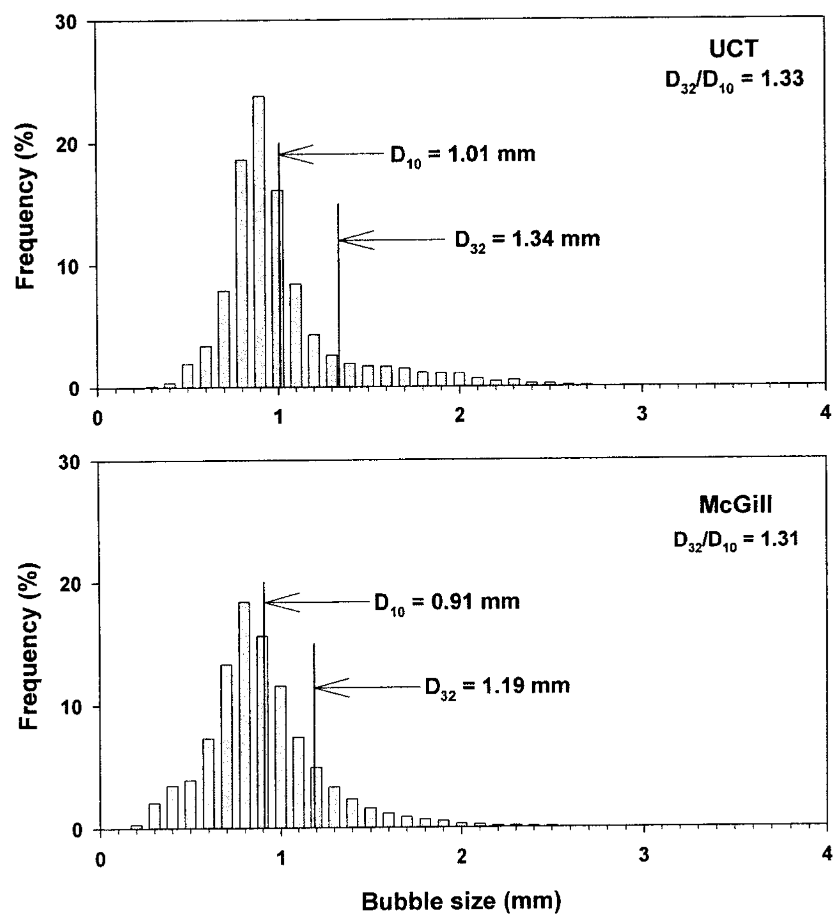

Figure 6.9. Plant comparison between the UCT and McGill University techniques

CHAPTER 7

TESTING THE k – S_b RELATIONSHIP AT THE MICROSCALE

In this chapter, the proposed relationship between flotation rate constant k and bubble surface area flux S_b for the pulp zone, namely $k = P\ S_b$, where P is the "floatability" factor, is tested at the microscale. Bubble size D_b was measured by an adaptation of the proposed technique.

7.1 Background

Recent studies have suggested that the pulp (or collection) zone rate constant, k, is linearly dependent on the bubble surface area flux, S_b (where $S_b = 6\ J_g / D_b$ and J_g is the superficial gas rate and D_b the bubble diameter (usually the Sauter mean)) (Gorain et al., 1997; Hernandez et al., 2001). The relationship is usually expressed as $k = P\ S_b$ where P is the "floatability factor" which encompasses the contribution of particle size and hydrophobicity. The dependence is predicted from a first principles analysis of the bubble-particle encounter process (Jameson et al., 1977). By isolating a "machine factor" (the delivery of S_b) from the effects contained in P the relationship has attractions in flotation circuit diagnosis and modeling.

In fundamental flotation chemistry studies, the use of a microcell of various designs is common, as pioneered by Fuerstenau et al. (1957). The technique invites use to explore the k - S_b relationship given the close control over the chemical and physical environment that it offers. This is explored in this chapter. A problem is measurement of bubble size and the adaptation to the McGill University bubble size measurement technique is described in some detail.

7.2 Experimental

7.2.1 Determination of bubble surface area flux, S_b

The microflotation cell was based on the design of Partridge and Smith (1969). It is 2 cm in diameter by 13 cm high for a nominal volume of 40 ml. To estimate S_b, gas rate J_g and bubble size D_b are required.

7.2.1.1 Superficial gas velocity, J_g

Superficial gas velocity was obtained by dividing the airflow rate (measured by a rotameter) by the cell cross-sectional area (3.1 cm^2). Airflow rate was regulated up to 92 ml/min, giving J_g up to 0.5 cm/s.

7.2.1.2 Bubble size, D_b

The McGill bubble size analyzer, originally designed for full size flotation machines, was adapted to measure the size of bubbles produced in the microflotation cell. Figure 7.1 illustrates the experimental setup. The sampling tube consists of two pieces of glass tubing joined with a flexible plastic section.

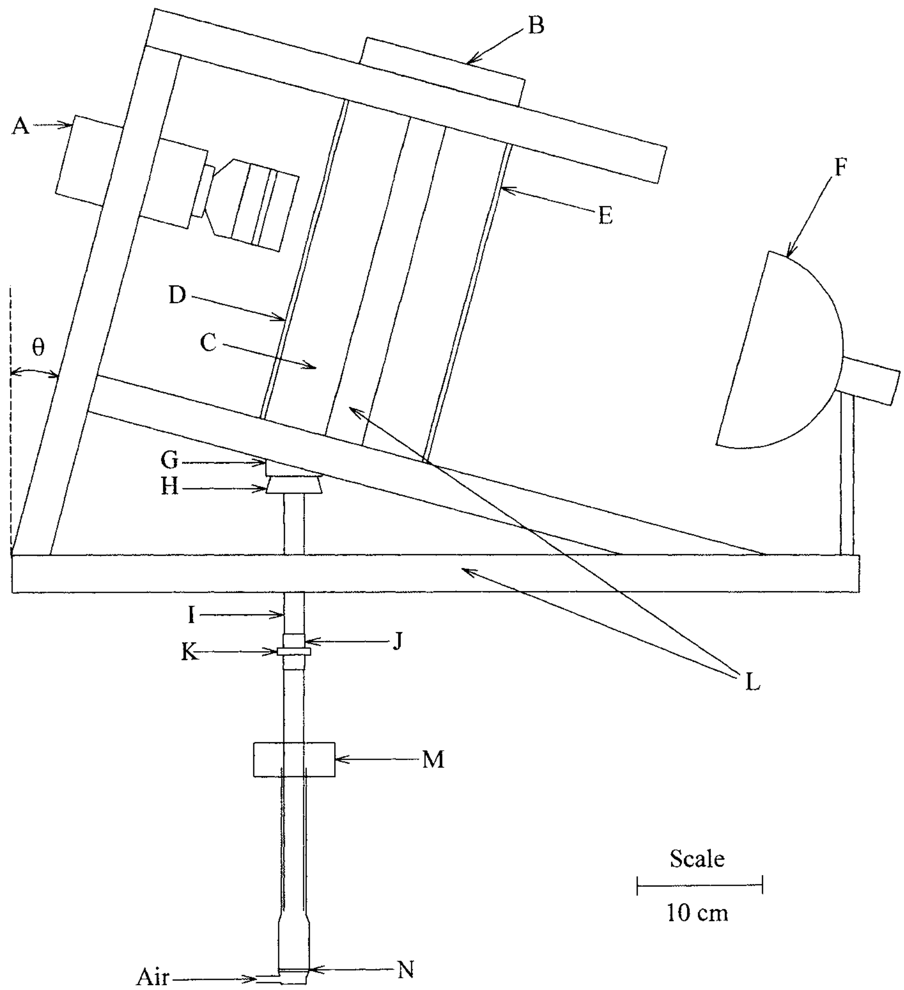

Figure 7.1. Scaled diagram of the experimental setup used for the direct measurement of bubble size distributions in the microflotation cell. A: digital camera, B: filling cap, C: viewing chamber, D: front window, E: back window, F: lamp, G: bubble viewer inlet, H: bored stopper, I: sampling glass tube, J: plastic tubing, K: tubing clamp, L: aluminum square bars (for support), M: microflotation cell, N: sparger. Detailed description of the components is given in Table 7.1

The procedure started by placing the tube (I) inside the cell. The internal diameter of the tube was selected to cover most of the cross-sectional area of the cell, i.e., in this case virtually all bubbles generated were collected. The clamp (K), located on the flexible portion of the sampling tube, was initially closed. The bubble viewer (C) was filled from the top via the cap (B) with a solution of frother in water (the same concentrations as used in the flotation tests). The clamp was opened slightly allowing the frother solution to fill the microflotation cell. Once the cell was full, the clamp was closed again. The cap (B) was tightened. This cap is threaded and has an o-ring to seal the viewing chamber. The clamp was then removed. It should be noted that this produces a pressure slightly below atmospheric in the viewing chamber. This low vacuum will stay constant if the bubble viewer is properly sealed, a convenient means to check for leaks. After hydrostatic equilibrium was reached, air was injected into the cell and adjusted to the desired flow rate value. Bubbles from the dispersion rose through the tube into the viewing chamber. After a steady flow of rising bubbles was established the light source was turned on and image capture launched. The bubble sizing procedure took place separate from the flotation test. In that sense bubble size in the microcell was "calibrated" and assumed to be the same when identical conditions were set in the flotation test.

Prior to sizing, the magnification factor was determined by acquiring an image with a 0.1 cm division transparent ruler placed in the focus plane. A certain number of pixels was counted and assigned a length from the ruler. The threshold value was 128 (half the gray scale) and the shape factor limit 0.6.

7.2.2 Determination of rate constant, k

7.2.2.1 Materials

Two solids were used, nickel oxide (99 % purity, 90% – 20 μm particle size, reagent grade from Sigma Aldrich, used as received) and galena, a high grade sample from Ward's Establishment. The galena sample was ground in a ball mill and the – 37 μm fraction isolated. The ground material was washed with 4 N hydrochloric acid to remove oxidation products and washed with deoxygenated deionized water.

Potassium ethyl xanthate and potassium amyl xanthate (Prospec Chemicals) were purified by recrystallization from acetone with petroleum ether. The frother Dowfroth 250C (Dow Chemicals) was used as received.

7.2.2.2 Flotation Rate Measurements

All the tests were conducted with a suspension prepared in distilled water at natural pH ~ 6.5 (± 0.2) and 10^{-5} M xanthate (ethyl for galena and amyl for nickel oxide) concentration. A 1-g sample (nickel oxide or galena) was mixed with 40 ml water, and the required quantity of xanthate added from a freshly prepared solution (0.1 g/l). After 5 minutes of conditioning the desired volume of frother was added and the slurry introduced into the cell. The airflow was set at the required rate and the float product collected at time intervals 30, 60, 80 and 120 s. A fresh sample was used for each time interval. The float product was filtered, dried and weighed and the recovery R determined as a function of time t. The flotation rate constant was calculated assuming the first order rate equation for a batch reactor, $R = 1 - \exp(-kt)$, and plotting $\ln(1 - R)$ vs. t.

7.2.3 Experimental program

The experiments proceeded in two stages. First, S_b in the microcell was obtained as a function of the two operating variables – airflow rate (which controls J_g and D_b) and frother dosage (which controls D_b). The dependence on frother dosage of bubble size was determined for five J_g values. The airflows selected were 48, 58, 69, 82 and 92 ml/min, i.e., J_g 0.25, 0.31, 0.37, 0.44 and 0.49 cm/s. The dependence was represented by an empirical equation obtained by regression analysis of the experimental data.

Second, twenty five rate constants (from the combination of five J_g and five frother concentrations) were determined for each material. The frother dosages were 0.025, 0.0375, 0.050, 0.0625 and 0.075 ml of 45% frother solution in the 40 ml. This was sufficient to control bubble size without producing bubbles that were too small producing too high a flotation rate for timing with a stopwatch. All twenty five experiments were repeated once and the average k was calculated for each S_b value. The cell was operated with a small froth layer (< 0.5 cm) as complete elimination gave less repeatable results.

7.3 Results and discussion

7.3.1 Bubble size

A specimen frame is given in Figure 7.2. For these conditions the bubbles are spherical and quite narrow in size distribution. The cumulative volume size distribution result for conditions in Figure 7.2 is given in Figure 7.3, along with the computed Sauter mean D_{32}. (The volume was selected in Figure 7.3 as this gives a distribution familiar to that when performing particle size analysis; for the same reason the size axis is logarithmic not linear.)

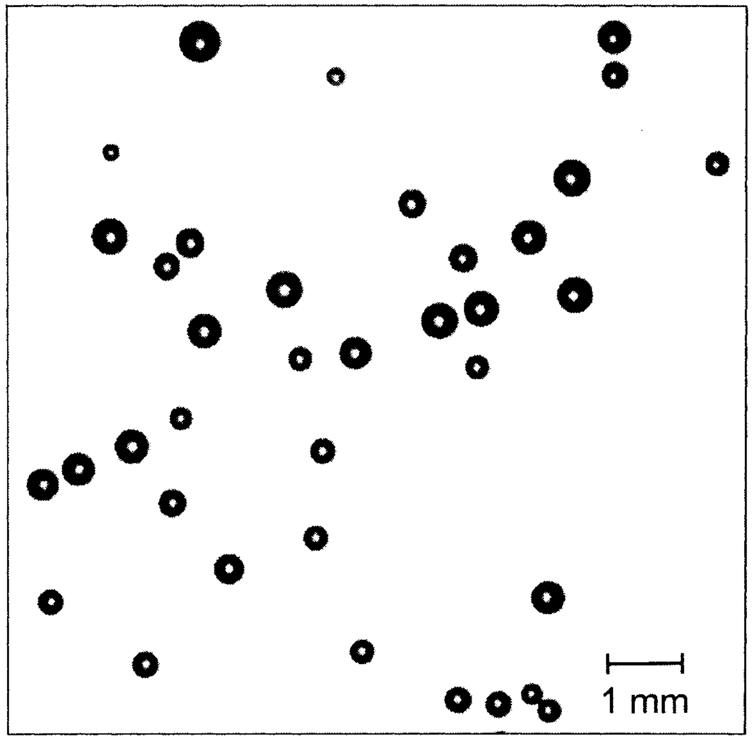

Figure 7.2. Image example. Frother concentration = 21 ppm, J_g = 0.25 cm/s

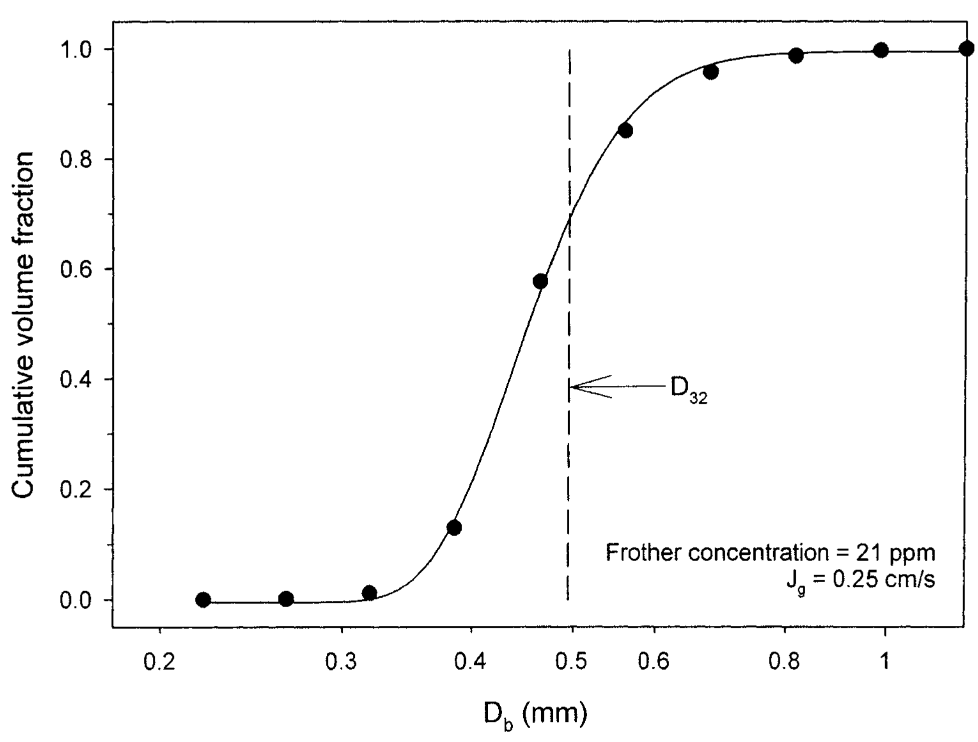

Figure 7.3. Example of a cumulative volume bubble size distribution

The mean bubble size as a function of the two variables is summarized in Figure 7.4. (This is one of the few times that such information on a microcell has been available, despite its long history.) The figure shows the fact that bubble size is strongly affected by the presence of frother due to its ability to hinder coalescence (Cheng et al., 1996). It is shown that bubble size decreases rapidly with increasing frother addition and at a particular frother concentration (ca. 30 ppm) coalescence appears to be completely prevented. Beyond this value, bubbles are produced at their minimum size for a given flow rate. (Cho and Laskowski (2002) refer to this value as the critical coalescence concentration, CCC.) Figure 7.4 also shows regression lines computed from a three-parameter model (Equation 7.1). This model well describes the experimental data. Regression analysis indicted that the coefficient of determination (r^2) was greater than 0.99 in all cases. Table 7.1 includes the values of the parameters.

$$D_b = D_o + ae^{-bx} \tag{7.1}$$

where x is frother concentration in ppm

Physically, D_o represents the original size of the bubbles generated at the sparger before any secondary processes (such as coalescence) occur ($D_b \rightarrow D_o$ as $x \rightarrow \infty$), a is the increment in size to D_o due to coalescence ($D_b \rightarrow D_o + a$ as $x \rightarrow 0$), and b is a parameter associated with frother type. Because bubble coalescence occurs near the point of production, a may be related to the structure of the sparger (in this case).

Bubble size in the microcell varied from 0.2 to 0.04 cm, and coupled with the J_g means a potentially deliverable S_b up to 74 s^{-1}. However, experiments were limited to frother concentrations less than 8.4 ppm ($D_{32} \approx 0.9$ mm) (to avoid too high a flotation rate) meaning S_b up to 35 s^{-1}, which remains comparable to full size machines (Deglon et al., 2000).

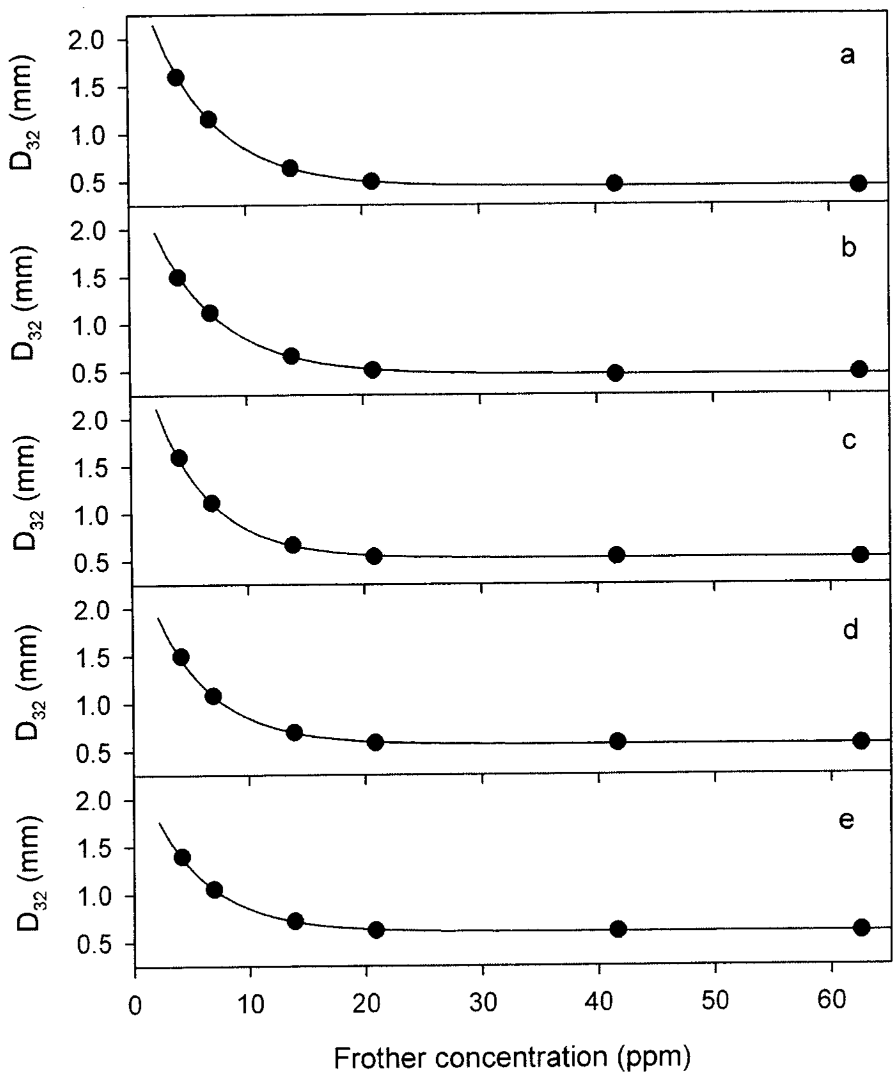

Figure 7.4. Effect of frother concentration on bubble size
a: Jg = 0.25, b: 0.31, c: 0.37, d: 0.44, and e: 0.49 cm/s

Table 7.1 Values of the parameters of Equation 7.1 (for Dowfroth 250)

J_g (cm/s)	D_o x 10^2 (cm)	a x 10^1 (cm)	b x 10^1 (1/ppm)
0.25	4.446	2.558	1.855
0.31	4.652	2.217	1.763
0.37	5.246	2.507	2.086
0.44	5.655	2.104	2.025
0.49	6.029	1.799	1.997

7.3.2 Flotation rate constant

Examples of the kinetic plots (i.e., ln (1 – R) vs. t) are shown in Figure 7.5. The required linearity through R = 1 to conform to the assumption of a first order rate process is obtained. Others have likewise shown this model holds for microflotation cells (e.g., Laskowski, 1998).

7.3.3 Testing k – S_b

The rate constant was determined for each condition (the average slope of two runs) and the corresponding S_b estimated from the "calibration". The presence of solids was assumed not to affect bubble size. A possible influence on D_b of residual xanthate was checked and found negligible. A synergistic effect of frother and xanthate on particle hydrophobicity, as contemplated by Leja (1982), was not considered. Taking this position means we assume xanthate influences particle hydrophobicity (i.e., P) only and frother influences bubble size (i.e., S_b) only. Certainly to reveal synergy, the effect of frother on D_b must be accounted for first (Laskowski, 1998).

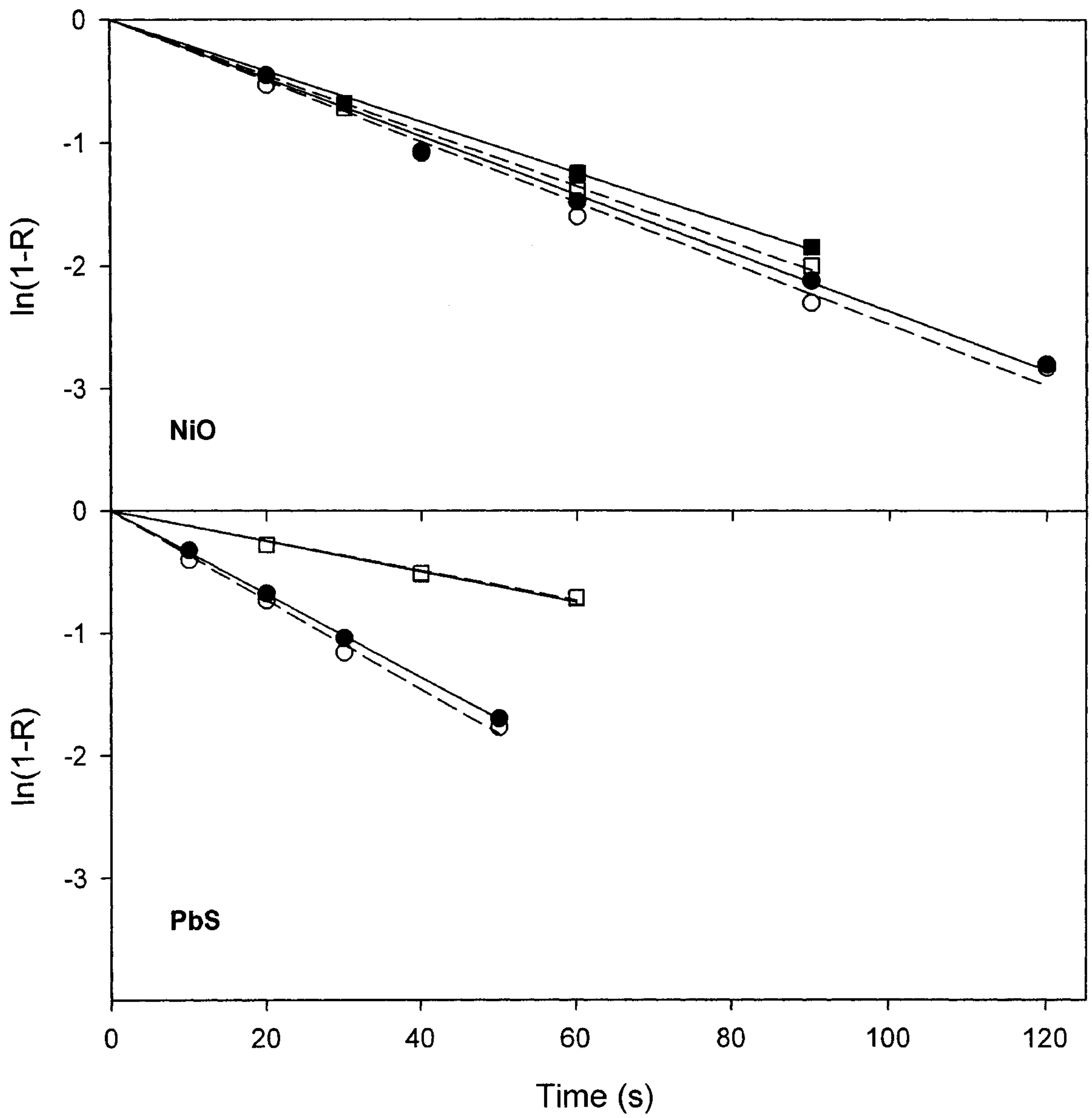

Figure 7.5. Examples of replicate kinetic plots (J_g = 0.25 cm/s)
Circles: 8.4 ppm (frother), squares: 4.2 ppm

The derived rate constant for both solids is plotted in Figure 7.6 against the surface area flux for each condition. A linear dependence between k and S_b though the origin appears to be reasonable, suggesting that the model k = P S_b is a plausible approximation.

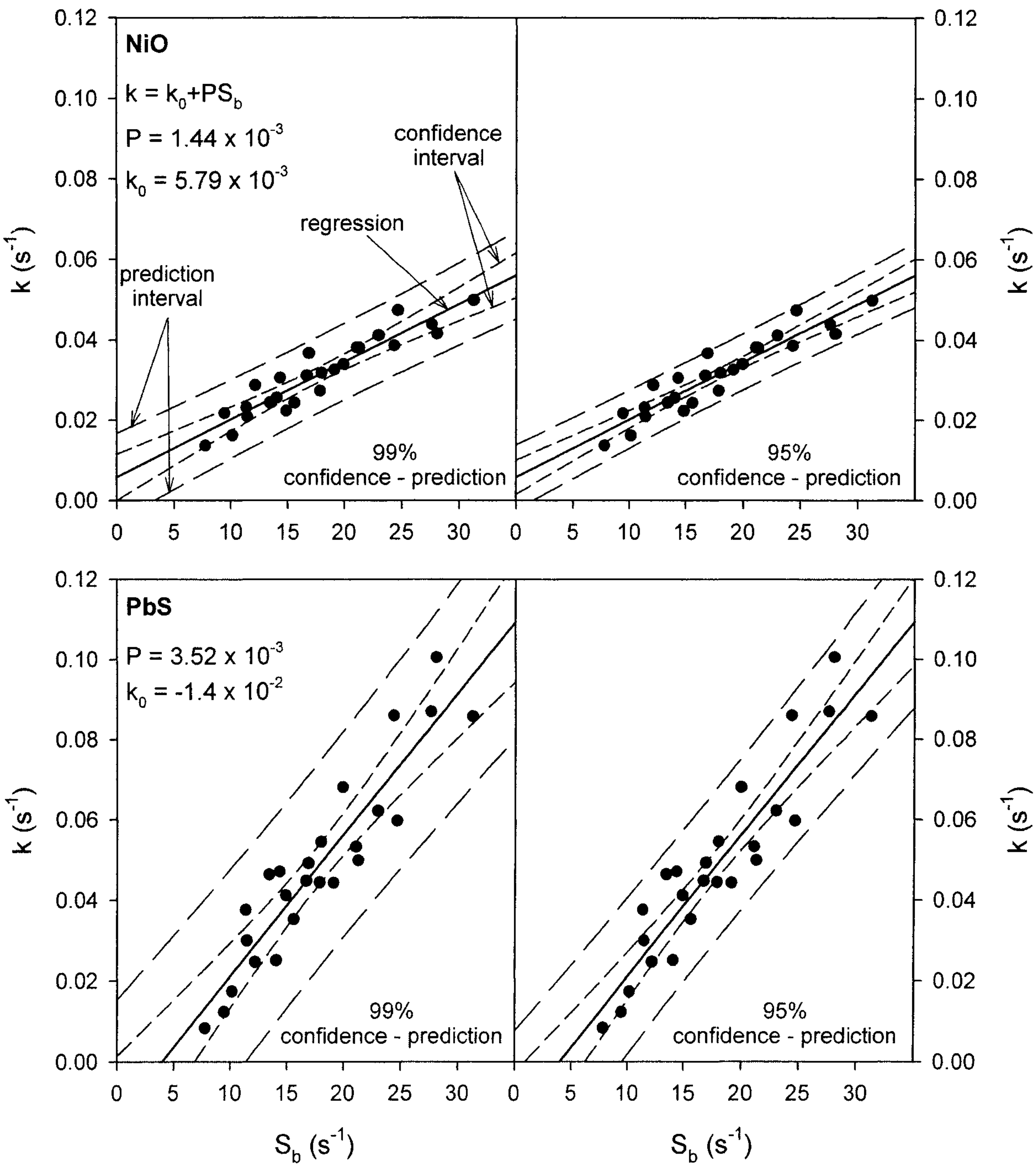

Figure 7.6. Confidence and prediction intervals for the model k = k_o + P S_b

Two approaches could be adopted to quantify the floatability factor P. The first involves the determination of the regression line $k = k_o + PS_b$ and testing the hypothesis that $k_o = 0$ at a certain significance level (a). The 99% (a = 0.01) and 95% (a = 0.05) confidence intervals are depicted in Figure 7.6. We could conclude from this figure that, for both solids, $k_o = 0$ at $a = 0.01$ with $P = 1.44 \times 10^{-3}$ for NiO and 3.52×10^{-3} for PbS. However, $k_o \neq 0$ at a higher significance level (a = 0.05) implying that either the model does not represent reality (random components relating k and S_b may not be being measured or fully understood, i.e., the model is just an approximation of something unknown and more complicated) or, the model is a representation of an ideal condition and the influence of not well controlled (but measurable) variables, such as froth level, makes the model depart from this ideality. For example, in the case of galena an intercept at ca. 4 s^{-1} is apparent, a circumstance associated with the presence of a froth (Gorain et al. 1998) (recall a shallow froth was retained for stable operation).

In the second approach, k_o is "forced" to be zero when performing the regression analysis. Figure 7.7 illustrates this procedure. The 99% and 95% confidence and prediction intervals (confidence and prediction intervals assess how much an estimated value and a future observation will fluctuate due to noise in the data, respectively) are also included. Since one interest in modeling the relationship $k - S_b$ is quantification of the floatability P of a mineral, we consider the prediction interval is the relevant statistic, more than confidence intervals in this case. In this sense, $k = P\,S_b$ is taken to be true within a certain prediction interval, keeping in mind that if future observations fall outside the interval the validity of the model has to be reconsidered.

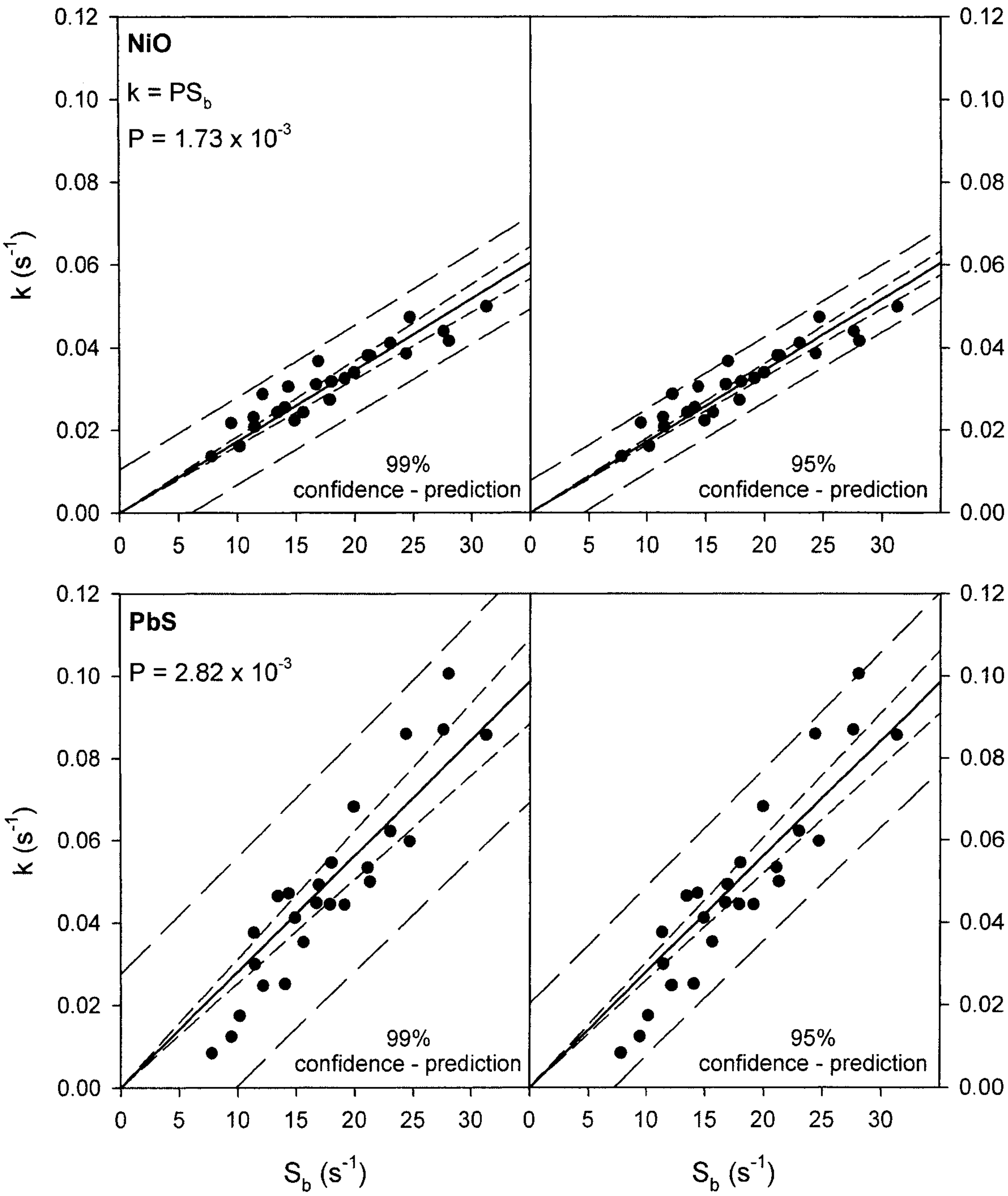

Figure 7.7. Confidence and prediction intervals for the model $k = P\,S_b$

It is noted that the galena data are more scattered (the prediction interval is wider) than that of NiO which probably stems from the higher flotation rate (the rate constant at equal S_b is nearly double that for NiO) giving less control over the flotation tests. The choice of NiO was in part because, from previous work (Naklicki et al., 2002), a slow float was anticipated. The floatability P for NiO was ca. 1.73×10^{-3} and for galena, ca. 2.82×10^{-3}, of the order starting to appear in the literature (Gorain et al., 2000). The microscale approach offers a means to study the impact of variables on P under well-controlled conditions, possibly giving a new lease on life to such a venerable test procedure.

The results at the microscale suggest the linear k–S_b relationship is reasonable. There is no previous analysis similar to that here, but several small-scale studies have explored the k–D_b dependence. The dependence found is of the form $k \propto 1 / D_b^m$, with m varying from 0 to 2 (Ahmed and Jameson, 1989; and Diaz-Penafiel and Dobby, 1994), and even 3 (Yoon, 1993). Recalling the definition, to agree with the linear dependence on S_b implies $m = 1$. To explore we have re-plotted the results assuming a form $k = P' S_b D_b^n$ (i.e., P is a function of D_b) with $n = -½$ (Figure 7.8) and $n = -1$ (Figure 7.9) (i.e., $m = 1.5$ and $m = 2$, respectively). It is arguable that the data are incapable of distinguishing among the options. The data might be less scattered, and models easier to discriminate, if a system of closely sized particles and bubbles could be manufactured. But, for practical purposes, the simplest model, $k = P S_b$, appears adequate, certainly for the range of bubble size achievable in typical flotation machines.

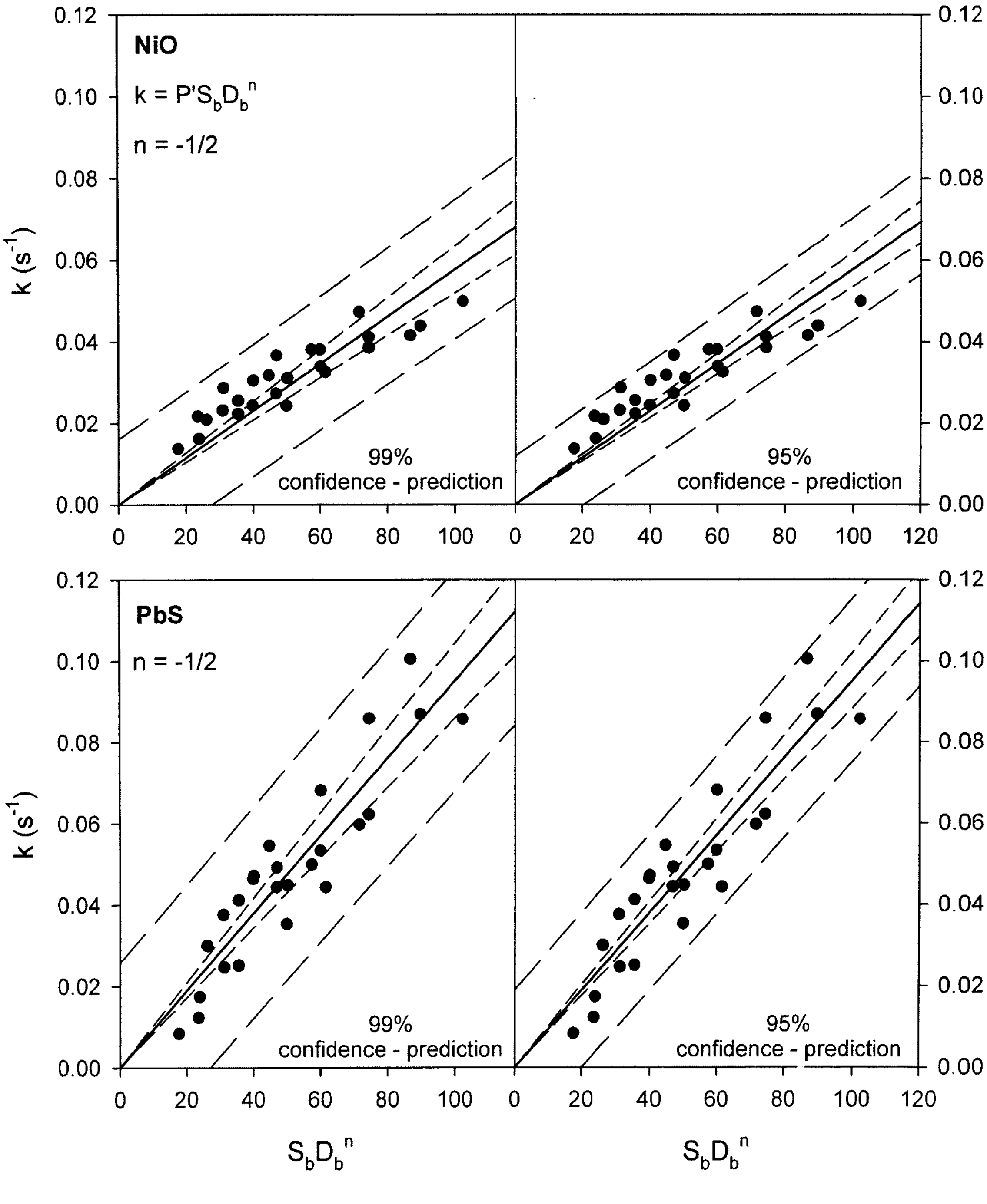

Figure 7.8. Confidence and prediction intervals for the model
$k = P' S_b D_b^n$ for $n = -½$

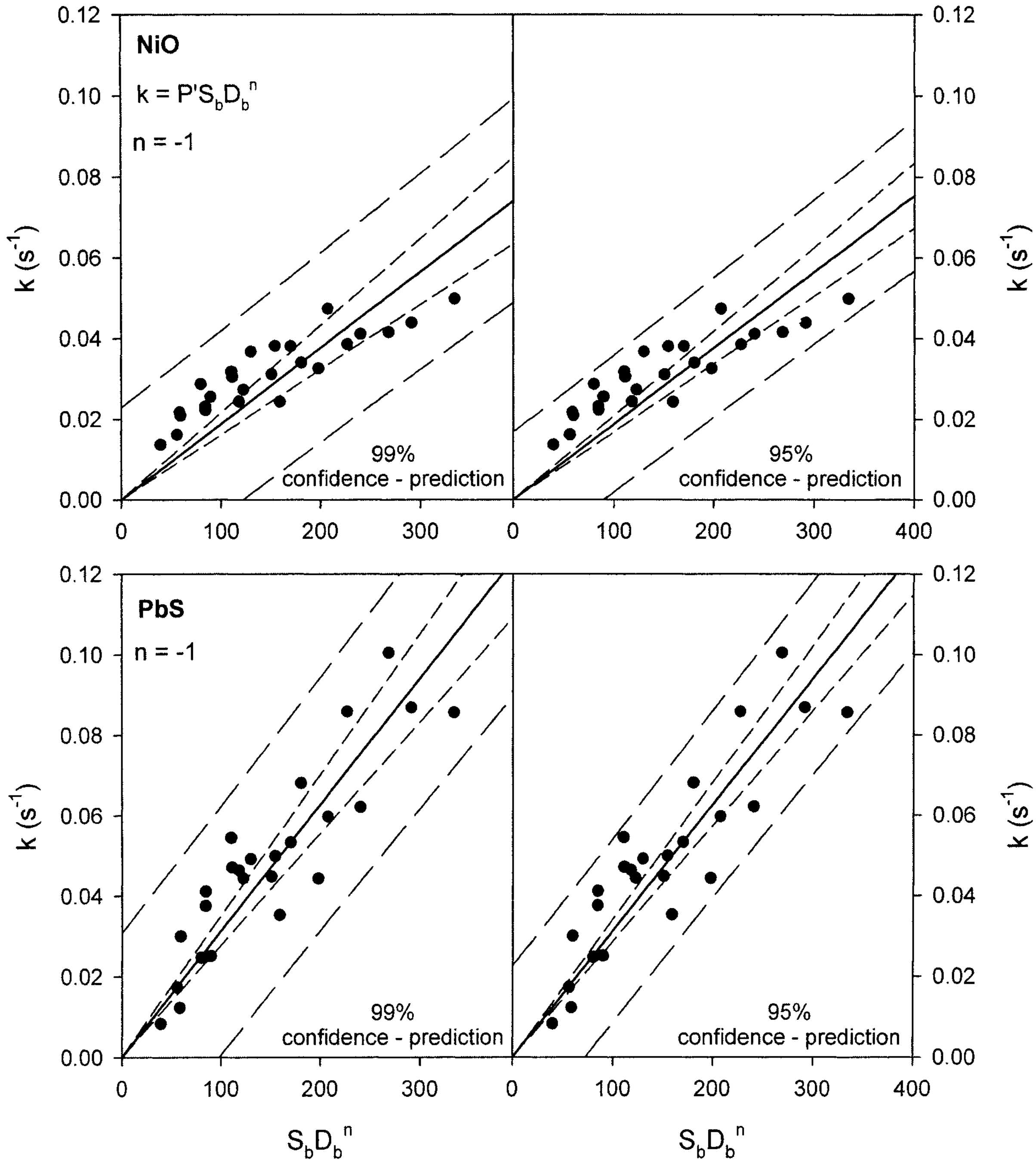

Figure 7.9. Confidence and prediction intervals for the model $k = P' S_b D_b^n$ for $n = -1$

7.4 Conclusions

- An adaptation of the McGill bubble size analyzer permitted measurement in a microscale flotation cell.
- A 3-parameter empirical equation is suggested to correlate frother concentration and bubble size; the parameters have physical significance.
- Bubble surface area flux ranged up to 50 s^{-1}, comparable to full size machines.
- The rate constant (k) determined as a function of surface area flux (S_b) for two materials (NiO and galena) reasonably agreed with the model $k = P\ S_b$, where P is floatability.
- The P values were in the published range.
- The data could not unambiguously discriminate among competing models of the form $k \propto 1/D_b^m$ where m varies up to 2.

CHAPTER 8

CONCLUSIONS AND SUGGESTIONS FOR FUTURE WORK

The proposed technique introduces the novel concept of angling the viewing chamber along with an optical arrangement based on incoherent imaging. This combination offers some solutions to common practical problems (bubble blurring, overlapping, clustering, contrast, etc.) through an uncomplicated image analysis algorithm, which uses solely a threshold and a shape factor criterion.

Besides the practical gains, the technique provides sensitive and consistent measurements. This ability encourages the study of various (nearly) unexplored facets such as the quantification of bubble coalescence and its impact on process performance at the industrial-scale, and the combined effects of airflow rate, machine type and geometry, and chemistry (notably frother type and dosage) on bubble size distribution. The technique is sufficiently flexible to be adapted to the micro-scale where gas-dispersion-related fundamental research could be conducted under the controlled conditions of the laboratory.

The image validation study evidenced that the technique, fortuitously, resolves two fundamental problems: since the motion of the bubble is limited to two-dimensions the defocus distance is small, and *a fortiori*, its position (i.e., its sign) is not ambiguous, it is invariably negative since the bubble always moves "behind" the focus plane. Therefore, a deterministic experimental and theoretical methodology was derived to test and understand the intrinsic biases of the system. A semi-empirical approach, which uses the fundamental method of Bongiovanni et al. (1997) (to correct the deviations due to system optics) along with an empirical equation to compensate for bubble deformation (due to the angled window) was proposed.

An experimental methodology was introduced to verify whether the calculated size distributions were representative of the actual population. The method consisted in producing controlled bi-modal bubble size mixtures in a column where the proportions (fine vs. coarse) were known *a priori*. The results showed the anticipated bi-modality in which the real and calculated proportions corresponded with a deviation of less than 15%, remarkably good considering the severity of the test. However, the deviation was correlated to J_g and biases against fine bubbles. This suggested that the mechanisms of sampling bias followed complex bubble–bubble and bubble–sampling tube interactions. Although the results were not sufficient to reveal the nature of such interactions, various mechanisms were postulated.

8.1 Limitations

The technique was developed with the mission of performing in (froth) flotation systems where frothers are generally used (to retard coalescence and stabilize the froth). Therefore, the data in this thesis were collected *in toto* in the presence of frothers. Consequently, the pertinent observations and proposed corrective empirical equations might not be extended to systems in which coalescence may occur. In addition, it is well documented that frothers inhibit bubble deformation.

The image correction protocol in section 4.4.5 was validated (against standardized bubbles) in a system where the background intensity was constant (i.e., with no solids accumulation). However, it is expected that, for the case of variable background, the essence of the proposed correction procedure will remain unaltered (as anticipated by Bongiovanni et al.), i.e., the prediction of $B_{1/2}$ through blurring quantification ($P_{1/2}$) using the BSM. Bongiovanni et al. writes:

> "Since we are only interested by the relative irradiance of the bubble image, the uniform irradiance *L* of the [light] source is chosen arbitrarily and the irradiance is normalized by the background brightness."

Therefore, the approach described in 3.2.1 (i.e., dividing the analysis in batches of frames to determine an average background intensity to calculate a characteristic $P_{1/2}$ for the batch) may be sufficient. Nevertheless, to be rigorous, a "standard" experiment with variable background caused by solids accumulation in the viewing chamber needs to be devised.

It has been observed that, in some cases, the bubbles appear "fully" covered by solid particles (e.g., the images from the base metal ore flotation in Figure 3.2). The observation arises from the fact that a significant number of bubbles do not feature the central bright spot. In this case, the bubble could behave as an "opaque" object. If this is confirmed, Equation 4.7 (i.e., the impact of reflected rays) should be eliminated from the correction protocol when fully loaded bubbles are present.

The method of Bongiovanni et al. (1997) is valid for bubbles > 100 μm where the effects of diffraction and interference can be neglected (because the size is large compared to the wavelength on the incident light).

8.2 Claims for original research

The merit of this work was the joining of recent with old (but not obsolete) concepts that were dispersed in the literature to conceive, develop and validate a novel and uncomplicated technique sufficiently robust to perform at the macro-scale, which is permitting the industry to address various gas dispersion related problems.

In addition, the technique proved to be sufficiently flexible to adapt to a laboratory-scale study where, for the first time, the bubble surface area flux (S_b) was determined in a micro-flotation cell. A mechanistic empirical model (Equation 7.1), in which the parameters have physical significance, was proposed to quantify the effect on bubble size of frother dosage in the micro-flotation cell. The model is expressed in terms of three parameters: D_o (the original size of the bubbles generated before any secondary processes, such as coalescence, occur), a (the increment in size due to coalescence), and b (which quantifies the coalescence prevention "strength" of the frother).

A unique experimental procedure based on the controlled generation of bi-modal bubble size distributions was introduced to verify whether the outputs were representative of the actual population.

A contribution was made to understanding the influence of the optical setup on the imaged bubble size, adding to the scarce literature on the subject. It was observed that, in addition to the practical improvements, the approach resolves fortuitously two fundamental problems (Δ is constant and small, and $\Delta < 0$). This observation (along with a proposed empirical approach to compensate for bubble deformation) was exploited to simplify the correction of intrinsic biases of the system.

8.3 Suggestions for future work

1. Generally, flotation is considered as a non-coalescing system due to the presence of frothers. However, in some cases (e.g., Figure 3.3) this may not be the case. If future studies attempt to quantify coalescence in flotation, it is worth reviewing the literature (particularly, in the Chemical Engineering domain where, in some cases, coalescence is a major issue, e.g., Tse et al., 2003) to establish consistent indicators (such as the $D_{43} - D_{10}$ difference) and standard methods of data analysis (e.g., see Figure 3 in Tse et al.'s paper).
2. The displaced-volume method used here to measure the standardized bubbles is a reliable technique provided that a significant number of bubbles are collected in the burette (to minimize the visual uncertainty associated with the location of the meniscus and thus the displaced volume). However, it is tedious particularly when bubbles are small (recall that, in some cases, ca. 1000 bubbles were required). The displaced-mass method (where an analytical balance could be used) should be explored, e.g., review the work of Leifer et al. (2003). They noted that employing a balance (with a 1 mg resolution in that case) allows the measurement of much smaller displaced volumes with elimination of using an optical calibration.
3. A "standard" experimental setup with variable background caused by solids accumulation and bubbles of known size should be devised to prove the approach described in 3.2.1 (i.e., dividing the analysis in batches of frames to determine an average background intensity to calculate a characteristic $P_{1/2}$ for the batch).

4. The BSM should be extended to include the effects of optical aberrations and diffraction (as indicated by Bongiovanni et al., 1997) to verify whether these effects explain the deviation illustrated in Figure 4.15. Also, it is suggested to conduct a study with objectives (lenses) of different qualities (Bongiovanni et al. reported discrepancies up to 20% on experimental intensity profiles with objectives and video cameras of low quality).
5. Equation 4.14 (the quantification of bubble deformation) was tested against bubbles between 0.9 and 3 mm. It is recommended to conduct experiments with larger bubbles as, in some cases (see Figure 3.2) bubbles could be considerably larger.
6. The bi-modal approach would have more impact if an extensive range of "narrow" peaks could be generated. The fine-coarse arrangement in this study (i.e., 0.5 μm vs. 100 μm, porosities, respectively) was the only combination where the two peaks were clearly defined (not overlapped). Studies oriented to conceive standard "multi-modal" mixtures should be conducted.

REFERENCES

Addlesee, A.J., Kew, P.A. "Development of the liquid film above a sliding bubble.", *Trans. I. Chem. E.*, **80**, Part A, 2002: 272–277.

Ahmed, N., Jameson, G.J. "The effect of bubble size on the rate of flotation of fine particles." *International Journal of Mineral Processing*, **14**, 1985: 195-215.

Aldrich, C., Feng, D. "Effect of frothers on bubble size distributions in flotation pulp phases and surface froths." *Minerals Engineering*, **13**, 2000: 1049-1057.

Barigou M., Greaves M. "A capillary suction prove for bubble size measurement." *Measurement Science & Technology*, **2**, 1991: 318-26.

Barigou, M., Greaves, M. "Bubble-size distributions in a mechanically agitated gas-liquid contactor." *Chemical Engineering Science*, **47**, 1992: 2009-2025.

Biswal, S.K., Reddy, P.S.R., Bhaumik, S.K. "Bubble size distribution in a flotation column." *Canadian Journal of Chemical Engineering*, **72**, 1994: 148-152.

Bongiovanni, C., Chevaillier, J.Ph., Fabre, J. "Sizing of bubbles by incoherent imaging: defocus bias." *Experiments in Fluids*, **23**, 1997: 209-216.

Broering, S., Fischer, J., Korte, T., Sollinger, S., Luebbert, A. "Flow structure of the dispersed gas-phase in real multiphase chemical reactors investigated by a new utlrasound-Doppler technique." *Can. J. Chem. Eng.*, **69**, 1991: 1247-1256.

Buchholz R., Zakrzewski, W., Schugerl, K. "Techniques for determining the properties of bubbles in bubble columns." *Int. Chem. Eng.*, **21**, 1981: 180-187.

Burgess, J.M., Calderbank, P.H. "The measurement of bubble parameters in two-phase dispersions. I. The development of an improved probe technique." *Chemical Engineering Science*, **30**, 1975: 743-750.

Cathignol, D., Chapelon, J.Y., Newhouse, V.L., Shankar, M. "Bubble sizing with a high spatial resolution." *Ultrason. Symp. Proc. '88*, **2**, 1988: 933-936.

Chen, F., Gomez, C.O., and Finch, J.A. "Technical note: bubble size measurement in flotation machines." *Minerals Engineering*, **14**, 2001: 427-432.

Cheng, Y.H., Mikhail, M.W., Salama, A.I.A., Al Taweel, A.M. "Bubble generation by a two-phase ejector." *COLUMN '96, Proc. Int. Symp. Column Flotation.* Editors: C.O. Gomez, C.O. and J.A. Finch, 1996: 3-11.

Cho, Y.S., Laskowski, J.S. "Effect of flotation frothers on bubble size and foam stability". *Int. J. Miner. Process.*, **64**, 2002: 69-80.

Clift, R., Grace, J.R., Weber, M.E. "Bubbles, Drops and Particles", Academic Press, New York, 1978, pp. 97-141

De Lasa, H., Lee, S.L.P., Bergougnou, M.A. "Bubble measurement in three-phase fluidized beds using a U-shaped optical fiber." *Canadian Journal of Chemical Engineering*, **62**, 1984: 165-169.

Deglon, D.A., Egya-Mensah, D., Franzidis, J.P. "Review of hydrodynamics and gas dispersion in flotation cells on South African Platinum concentrators." *Minerals Engineering*, **13**, 2000: 235-244.

Deglon, D.A. "A hydrodynamic investigation of fine particle flotation in a batch flotation cell." Ph.D. Thesis, University of Cape Town, 1998.

Diaz-Penafiel, P., Dobby, G.S. "Kinetic studies in flotation columns: bubble size effect." *Minerals Engineering*, **7**, 1994: 465-478.

Du, L., Ding, Y., Prokop, A., Tanner, R.D. "Measurement of bubble size distribution in protein foam fractionation column using capillary probe with photoelectric sensors." *Applied Biochemistry and Biotechnology*, **91-93**, 2001: 387-404.

Duraiswami, R., Prabhukumar, S., Chahine, G.L. "Bubble counting using an inverse acoustic scattering method," *J. Acoust. Soc. Am.*, **104**, 2699 (1998).

Durst, F., Zare, M. "Laser Doppler measurements in two-phase flows." *In Proceedings of the LDA Symposium, Copenhagen, Denmark*, 1975: 403-429.

Euzen, J.P. "Scale-up Methodology for Chemical Processes." Paris, Editions Technip, 1993.

Fuerstenau, D.W., Metzer, P.H., Seele, G.D. "How to use modified tube for better flotation testing", *Eng. & Mining J.*, **158**, 1957: 93-95.

Gorain B.K., Napier-Munn, T.J., Franzidis J.P., Manlapig, E.V. "Studies on impeller type, impeller speed and air flow rate in an industrial scale flotation cell. Part 5: Validation of k-S_b relationship and effect of froth depth." *Minerals Engineering*, **11**, 1998: 615-626.

Gorain B.K., Franzidis J.P., Manlapig E.V. "Studies on impeller type, impeller speed and air flow rate in an industrial scale flotation cell – part 4: effect of bubble surface area flux on flotation performance." *Minerals Engineering*, **10**, 1997: 367-379.

Gorain B.K., Franzidis J.P., Manlapig E.V. "The empirical prediction of bubble surface area flux in mechanical flotation cells from cell design and operating data." *Minerals Engineering*, **12**, 1999: 309-322.

Gorain, B.K., Franzidis, J.P. Ward, K., Johnson, N.W., Manlapig, E. "Modelling of Mount Isa Rougher-scavenger copper flotation circuit using size-liberation data." *Minerals & Metall. Process.*, **17**, 2000: 173-180.

Gorain, B.K. "The effect of bubble surface area flux on the kinetics of flotation and its relevance to scale-up." Ph.D. Thesis, University of Queensland, 1997.

Gorain, B.K., "An integrated approach to optimization of large flotation cell oparation." *In Proceedings Flotation and Flocculation*, Ed. by J. Ralston, J.D. Miller and J. Rubio, Hawaii, 2002: 193-201.

Gorain, B.K., Franzidis, J.P., Manlapig, E.V. "Studies on impeller type, impeller speed and air flow rate in an industrial scale flotation cell - part 1: effect of bubble size distribution." *Minerals Engineering*, **8**, 1995: 615-635.

Grau, R.A., Heiskanen, K. "Visual technique for measuring bubble size in flotation machines." *Minerals Engineering*, **15**, 2002: 507-513.

Greaves, M., Kobbacy, K.A.H. "Measurement of bubble size distribution in turbulent gas-liquid dispersions." *Chemical Engineering Research & Design*, **62**, 1984: 3-12.

Harvey, S.B., Best, J.P., Soh, W.K. "Vapour bubble measurement using image analysis." *Meas. Sci. Technol.*, **7**, 1996: 592.

Hernandez, H., Gomez, C. O. and J. A. Finch, "A Test of the Flotation Rate vs. Bubble Surface Area Flux Relationship", *Proc. 4th UBC-McGill Symposium on Fundamentals in Mineral Processing* (Eds. J. A. Finch, S. R. Rao and Liming Huang), Met. Soc. CIM, Toronto, Aug 26-29, 2001, pp 59-74.

Hernandez-Aguilar, J.R., Gomez, C.O., Finch, J.A. "A technique for the direct measurement of bubble size distributions in industrial flotation cells." *Proc. of the 34th Annual Meeting of the Canadian Mineral Processors*, ed. J.E. Nesset, 2002: 389-402.

Hewitt, G.F. "Measurement of Two Phase Flow Parameters." London, Academic Press, 1978.

Hilgert, W., Hofmann, H. "Characterization of gas phase flow in bubble columns at low gas velocities with the aid of an ultrasonic Doppler technique." *Ger. Chem.-Ing.-Tech.*, **58**, 1986: 228-229.

Hui, S. "Three-phase mixing and flotation in mechanical cells." Ph.D. Thesis, University of Newcastle, 2000

Humeres, E., Debacher, N.A., Wagner, T.M. "Effect of bubble size on the kinetics of flotation of pyrite." *Colloids & Surfaces A-Physicochemical & Engineering Aspects*, **149**, 1999: 595-601.

Hunold, M., Krauthauf, T., Mueller, J., Putz, H.J. "Effect of air volume and air bubble size distribution on flotation in injector-aerated deinking cells." *Journal of Pulp & Paper Science*. **23**, 1997: J555-J560.

Jameson, G.J., Nam, S., Moo Young, M. "Physical factors affecting recovery rate in flotation", *Minerals Science and Engineering*, **9**, 1977: 103-118.

Jameson, G.J. and Allum, P. "A survey of bubble sizes in industrial flotation cells." *Report to AMIRA'Ltd (Australian Mineral Industries Research Association Limited)*, 1984.

Klassen, V.I., Mokrousov, V.A. "An introduction to the theory of flotation." Butterworths & Co., London, 1963, pp. 353-385.

Lage, P L C. Esposito, R O. "Experimental determination of bubble size distributions in bubble columns: Prediction of mean bubble diameter and gas hold up." *Powder Technology*, **101**, 1999: 142-150.

Lammers, J.H. "The stability of bubbly flows." Published by the Univesity of Twente, Netherlands, 1994.

Laskowski, J. S. "Frothers and Frothing", in "Frothing in Flotation II", (Eds. J. S. Laskowski and E. T. Woodburn), Gordon and Breach Science Publishers, Amsterdam, 1998, pp 1 – 49.

Lee, S.L., Srinivasan, J. "An LDA technique for in situ simultaneous velocity and size measurement of large spherical particles in a two-phase suspension flow." *International Journal of Multiphase Flow*, **8**, 1982: 47-57.

Lee, S.L., Srinivasan, J. "Measurement of local size and velocity probability density distributions in two-phase suspension flows by laser-Doppler technique." *International Journal of Multiphase Flow*, **4**, 1978: 141-55.

Leifer, I., De Leeuw, G., Kunz, G., Cohen, L.H. "Calibrating optical bubble size by the displaced-mass method." *Chemical Engineering Science*, **58**, 2003: 5211 – 5216.

Leja, J. "Surface Chemistry of Froth Flotation", Plenum Press, New York, 1982.

Lin, J.N., Banerji, S.K., Yasuda, H. "Role of interfacial tension in the formation and the detachment of air bubbles. 1. A single hole on a horizontal plane immersed in water." *Langmuir*, **10**, 1994: 936-942.

Luebbert, A., Korte, T., Larson, B. "Simple measuring techniques for the determination of bubble- and bulk-phase velocities in bioreactors." *Appl. Biochem. Biotechnol.*, **14**, 1987: 207-219.

Malysa, K. Ng, S. Cymbalisty, L. Czarnecki, J. Masliyah, J. "Method of visualization and characterization of aggregate flow inside a separation vessel, Part 1. Size, shape and rise velocity of the aggregates." *International Journal of Mineral Processing*, **55**, 1999: 171-188.

Martin, W.W.; Adbelmessih, A.H.; Liska, J.J.; Durst, F. "Characteristics of laser-Doppler signals from bubbles." *International Journal of Multiphase Flow*, **7**, 1981: 439-460.

Meernik, P.R., Yuen, M.C. "Optical method for determining bubble size distributions - Part I. Theory." *Journal of Fluids Engineering-Transactions of the ASME*, **110**, 1988a: 325-331.

Meernik, P.R., Yuen, M.C. "Optical method for determining bubble size distributions - Part II. Application to bubble size measurement in a three-phase fluidized bed." *Journal of Fluids Engineering-Transactions of the ASME*, **110**, 1988b: 332-338.

Minnaert, M., "On musical air-bubbles and the sounds of running water." *Phil. Mag.*, **16**, 1933: 235-248.

Miyahara, T., Hayahino, T. "Size of bubbles generated from perforated plates in non-Newtonian liquids." *Journal of Chemical Engineering of Japan*, **28**, 1995: 596-600.

Naklicki, M. L., Rao, S. R., Gomez, M. and J. A. Finch, "Flotation and surface analysis of the Ni(II) oxide/amyl xanthate system, *Int. J. Miner. Process.*, **65**, 2002: 73-82

Nelson, M.G., F. P. Traczyk, and D. Lelinski, "Design of mechanical flotation machines," *In Proc. Mineral Processing Plant Design, Practice, and Control*, Ed. A. L. Mular, D. N. Halbe, and D. J. Barratt, Published by the Society for Mining, Metallurgy, and Exploration, Vol. 1, pp. 1179-1203 (2002).

Orsat, V. Vigneault, C. Raghavan, G S V. "Air diffusers characterization using a digitized image analysis system." *Applied Engineering in Agriculture*, **9**, 1993: 115-121.

Pamperin, O., Rath, H-J. "Influence of buoyancy on bubble formation at submerged orifices." *Chemical Engineering Science*, **50**, 1995: 3009-3024.

Parthasarathy, R., Ahmed, N. "Bubble size distribution in a gas sparged vessel agitated by a Rushton turbine." *I and EC Research*, **33**, 1994: 703-711.

Parthasarathy, R., Ahmed, N. "Size distribution of bubbles generated by fine-pore spargers." *Journal of Chemical Engineering of Japan*, **29**, 1996: 1030-1034.

Parthasarathy, R., Jameson, G.J., Ahmed, N. "Bubble breakup in stirred vessels. Predicting the Sauter mean diameter." *Chemical Engineering Research & Design*, **69** 1991: 295-301.

Partridge, A. C., Smith, G. W. "Small-sample flotation testing: a new cell", *Trans. Inst. Min. Metall.*, **80**, 1969: C199-C200.

Perry, R.H., Green, D.W. "Perry's Chemical Engineers' Handbook 7th Edition". McGraw Hill, New York, 1997.

Polli, M., Di Stanislao, M., Bagatin, R., Abu Bakr, E., Masi, M., 2002. Bubble size distribution in the sparger region of bubble columns. *Chemical Engineering Science*, **57**, 197-205.

Qiu, D., Dhir, V.K., "Experimental study of flow pattern and heat transfer associated with a bubble sliding on downward facing inclined surfaces", *Experimental Thermal and Fluid Science*, **26**, 2002: 605–616.

Randall, E.W., Goodall, C.M., Fairlamb, P.M., Dold, P.L., O'Connor, C.T., 1989. A method for measuring the sizes of bubbles in two- and three-phase systems. *Journal of Physics E: Scientific Instruments*, **22**, 827-833.

Raper, J. A.; Kearney, M. S.; Burgess, J. M.; Fell, C. J. D. "The structure of industrial sieve tray froths." *Chemical Engineering Science*, **37**, 1982: 501-506.

Reddy, P.S.R., Prakash, S., Bhattacharyya, K.K., Sastri, S.R.S., and Narsimhan, K.S. "Flotation Column for the Recovery of Coal Fines." *In Column Flotation-88, K.V.S. Sastry, Ed, SME Publications,* 1988: 221-223.

Reynolds, V. G., "Bubble Measurement Cell," Canadian Patent 2024972 (1992).

Rodrigues, R.T., Rubio, J. "New basis for measuring the size distribution of bubbles." *Minerals Engineering*, **16**, 2003: 757.

Saberi, S. Shakourzadeh, K. Bastoul, D. "Bubble size and velocity measurement in gas-liquid systems: application of fiber optic technique to pilot plant scale." *Canadian Journal of Chemical Engineering*, **73**, 1995: 253-257.

Saxena, A.C.; Rao, N.S.; Saxena, S.C. "Bubble size distribution in bubble columns." *Canadian Journal of Chemical Engineering*, **68**, 1990: 159-161.

Semiat, R.; Dukler, A.E. "Simultaneous measurement of size and velocity of bubbles or drops: a new optical technique." *AIChE Journal*, **27**, 1981: 148-159.

Steinemann, J. and Buchholz, R. "Application of an electrical conductivity microprobe for the characterization of bubble behavior in gas-liquid bubble flow." *Part. Charact.*, **1**, 1984: 102-107.

Steinmuller, A. "Hydrodynamics of a cocurrent-downwards bubble column with gas entrainment by a liquid jet." Ph.D. Thesis, University of the Witwatersrand, 1999.

Svendsen, H F. Luo, He'an. Hjarbo, K W. Jakobsen, H A. "Experimental determination and modeling of bubble size distributions in bubble columns." *Chinese Journal of Chemical Engineering*, **6**, 1998: 29-41.

Takahashi, Koji; McManamey, William J.; Nienow, Alvin W. "Bubble size distributions in impeller region in a gas-sparged vessel agitated by a Rushton turbine." *Journal of Chemical Engineering of Japan*, **25**, 1992: 427-432.

Tassin, A. L., and D. E. Nikitopoulos, "Non-intrusive measurements of bubble size and velocity," *Experiments in Fluids*, **19**, 1995: 121.

Thang, N.T. and Davis, M.R. "The structure of bubbly flow through venturis." *International Journal of Multiphase Flow*, **5**, 1979: 17-37.

Torrealba-Vargas, J. Ph.D. Dissertation (in progress), McGill University, 2004.

Tse, K. L., Martin, T., McFarlane, C. M., and Nienow, A.W, 2003. Small bubble formation via a coalescence dependent break-up mechanism. *Chemical Engineering Science*, **58**, 275 – 286.

Tsuge, Hideki; Terasaka, Koichi; Koshida, Wataru; Matsue, Hirokazu "Bubble formation at submerged nozzles for small gas flow rate under low gravity." *Chemical Engineering Science*, **52**, 1997: 3415-3420.

Tucker, J P. Deglon, D A. Franzidis, J -P. Harris, M C., and O'Connor, C T. "Evaluation of a direct method of bubble size distribution measurement in a laboratory batch flotation cell." *Minerals Engineering*, **7**, 1994: 667-680.

Ungut, A., Yule, A.J., Taylor, D.S., and Chigier, N.A. "Particle size measurement by laser anemometry." *J. Energy*, **2**, 1978: 330-336.

Varley, J. "Submerged gas-liquid jets: bubble size prediction." *Chemical Engineering Science*, **50**, 1995: 901-905.

Vigneault, C. Panneton, B. Raghavan, G S V. "Real time image digitizing system for measurement of air bubbles." *Canadian Agricultural Engineering*, **34**, 1992: 151-155.

Yianatos, J., Bergh, L., Condori, P., Aguilera, J. "Hydrodynamic and metallurgical characterization of industrial flotation banks for control purposes". *Minerals Engineering*, **14**, 2001: 1033-1046.

Yoon, R.H. "Microbubble flotation", *Minerals Engineering*, **6**, 1993: 619-630.

Yoon, R.H., and Luttrell, G.H. "The effect of bubble size on fine coal flotation." *Coal Preparation*, **2**, 1986: 179-192.

Yule, A.J., Chigier, N.A., Atkam, S., and Ungut, A. "Particle size and velocity measurement by laser anemometry." *J. Energy*, **1**, 1977: 220-228.

Zhang, L., Shoji, M., 2001. "Aperiodic bubble formation from a submerged orifice". *Chemical Engineering Science*, **56**, 5371-5381.

Zhang, Z., Dai, G., Chen, M., 1989. "Study on measurement of bubble size distribution in stirred vessels by photo-electric capillary probe technique." *Journal of Chemical Engineering of Chinese Universities*, **3**, 42-49.

Zhou, Z.A., Xu, Z., Masliyah, J., Kasongo, T., Christendat, D., Hyland, K., Kizor, T., and Cox, D. "Application of on-line visualization to flotation systems." *In Proc. of the 32nd Annual Operator's Conference of the Canadian Mineral Processors, compiled by M. Tagami, Canadian Mineral Processors*, 2000: 120-137.

Zun, I. and Saje, F. "Statistical characteristics of bubble flow." *In Proc. 3rd Austrian-Ital.-Yugosl. Chem. Eng. Conf., Publisher: Tech. Univ. Graz*, **2**, 1982: 112-119.

APPENDICES

APPENDIX I

EXAMPLE OF THE USE OF THE BSM

Consider the case of a bubble image where $D_{b1/2}$ = 2.8 mm (i.e., the equivalent spherical diameter after thresholding at ½ the irradiance level). The irradiance profile near the bubble edge is given in the following figure:

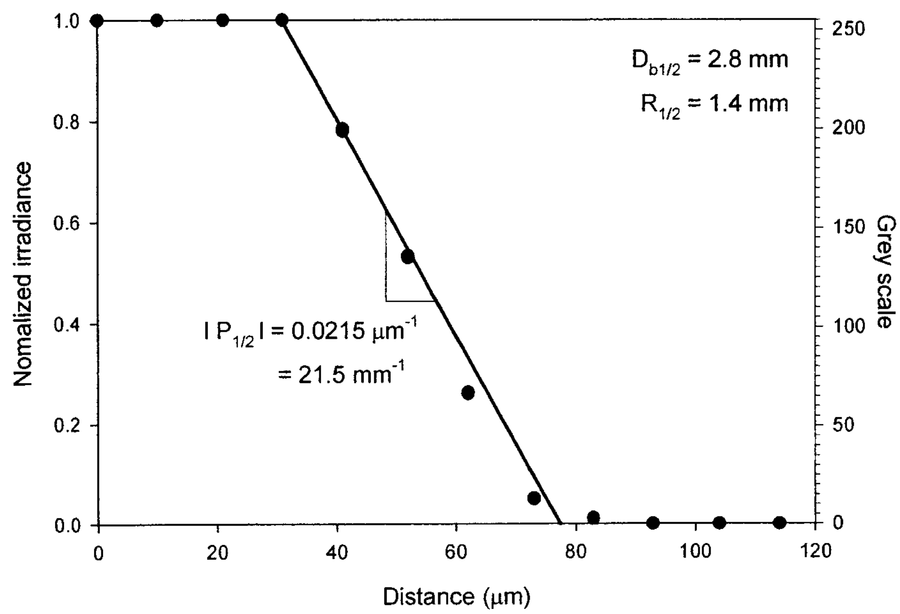

Figure A1. Example of the use of the BSM

The $P_{1/2}$ (i.e., the intensity gradient on the contour at the same half irradiance level) was obtained from a linear regression (i.e., the absolute value of the slope). The size of the entrance pupil was r_P = 4.44 mm, therefore, $r_P/R_{1/2}$ = 4.44 mm/1.4 mm ≈ 3. Also, $R_{1/2}\,P_{1/2}$ = 1.4 mm x 21.5 mm^{-1} ≈ 30. Using these two values and Figure 4.2, the predicted $B_{1/2}$ (Equation 4.9) is ca. – 0.8 % (since Δ is always < 0, then $B_{1/2}$ is invariably negative).

APPENDIX II

PROCEDURE TO DETERMINE THE CHARACTERISTICS OF THE ENTRANCE PUPIL

The measurements (size and position of the entrance pupil) were performed using a commercially available image analysis system (Optikos OpTest) on a Nikon Nikkor 50-mm f/1.4 lens (Serial Number 5299461) as outlined below.

1. Procedure

Before performing the measurements, the lens aperture was set to f/5.6 and the focus ring set to halfway between 0.6 and 0.7 m. Next the lens was mounted parallel to the axis of the optical bench with the front of the lens facing the OpTest Image Analyzer. Diffuse illumination was provided at the rear of the lens. Next, the image analyzer was focused on the edge of the entrance pupil, which itself is an image of the aperture stop (iris) inside the lens. Using motorized translation stages, the image analyzer was manipulated to measure the distance across the entrance pupil. Because the pupil was not round, but in fact a seven-sided polygon, four measurements were made across different azimuths to determine the average "diameter" of the pupil. Next, the image analyzer focus stage was moved along the optical axis of the lens (Z-direction) and translated until it was focused on the engraved surface on the front of the lens. The distance in Z was recorded before then focusing and translating to the very front edge of the lens. After recording the location in Z of this front edge, the lens was removed from the optical bench and the total lens length was measured. The distance from the rear flange to the back edge of the lens was also recorded.

2. Results

The results of the measurements on the size of the entrance pupil are: 8.937, 8.735, 8.669, and 9.188 mm, giving an average of 8.882 mm.

The diagram next shows the location of the entrance pupil relative to various lens features.

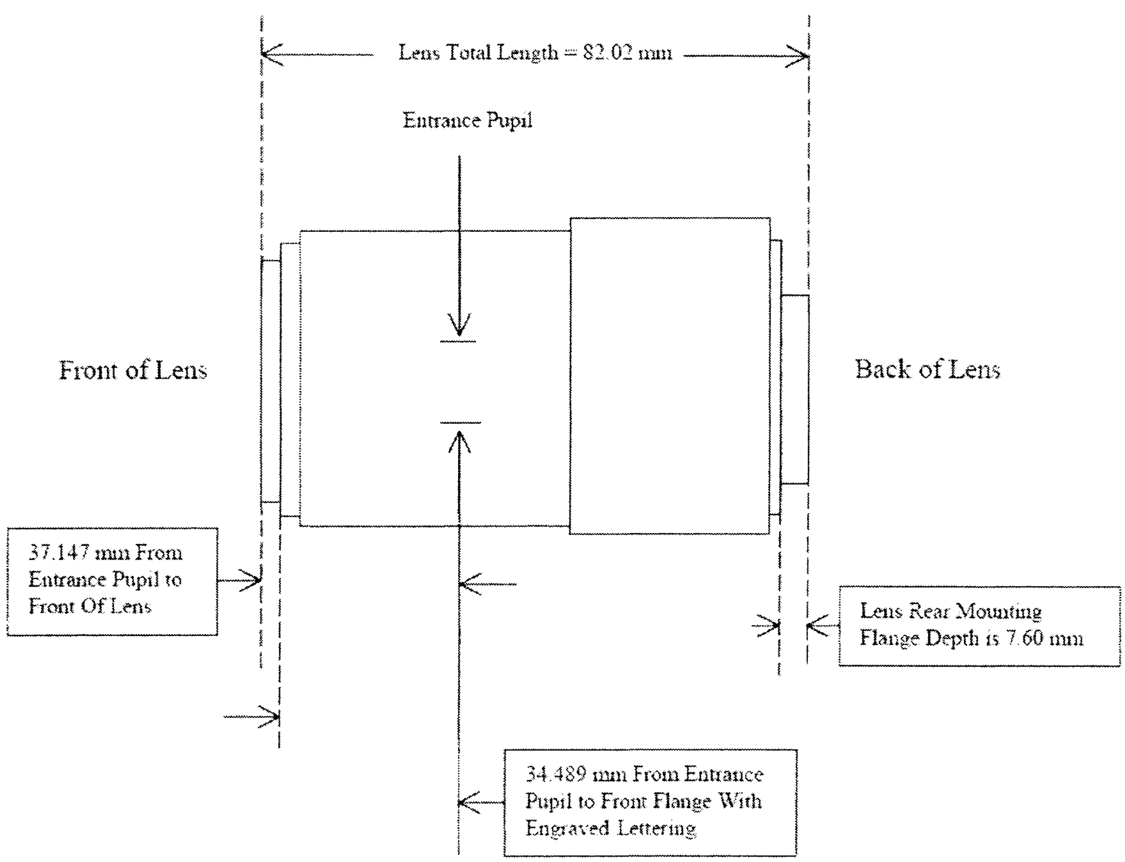

Figure A2. Size and location of the entrance pupil

From these measurements it can be seen that the entrance pupil is located 37.273 mm in front of the rear mounting flange on the lens (82.02 - 37.147 - 7.60 = 37.273 mm). Note that changing the focus ring setting moves all of the lens optical elements (and the iris) relative to the rear mounting flange of the lens. Therefore, the total length of the lens will increase or decrease, but the other relationships are preserved.

APPENDIX III

RESULTS FROM THE IMAGING VS DISPLACED VOLUME METHODS

Table A3. Imaging sizing bias ($\theta_W = 5°$; threshold = ½ intensity; $\theta_L = 6.3°$)

D_b – burette (μm)	STDEV (μm)	$D_{b1/2}$ - images (μm)	STDEV (μm)	$B_{1/2}$ (%)
674	1	671	1	-0.4
915	2	912	1	-0.3
1120	1	1111	5	-0.8
1428	5	1413	2	-1.1
1602	14	1593	17	-0.6
2061	6	2041	5	-1.0
2587	14	2553	13	-1.3
2785	8	2762	6	-0.8
4003	11	3938	10	-1.6